POLITECNICO DI MILANO
Facoltà di Ingegneria Industriale
Corso di Laurea Specialistica in Ingegneria Aeronautica

Numerical Modelling of Non-classical Aileron Buzz

Relatore: Prof. Giuseppe QUARANTA
Correlatore: Prof. Alberto GUARDONE

Tesi di Laurea di:
Francesca FUSI Matr. 744956

Anno Accademico 2011-2012

Contents

Nomenclature

$\mathbf{a}$	Local advection velocity
a_1, a_i, a_N	Coefficient of the aerodynamic model structure
$\mathbf{A}$, $\mathbf{A}_a$	State matrix of the model structure
A	Prescribed training signal amplitude
A_{at}	Rotation amplitude after transient response
b_1, b_i, b_N	Coefficient of the aerodynamic model structure
$\mathbf{B}$, $\mathbf{B}_a$	Input matrix of the model structure
c	Airfoil chord
c_1, c_i, c_N	Amplitude factor in the aerodynamic model structure
$\mathbf{C}$, $\mathbf{C}_a$	Output matrix of the model structure
$\boldsymbol{C}$	Generalized damping matrix
C_{M_H}	Hinge moment coefficient
$C_{M_{H,0}}$	Initial hinge moment coefficient
c_p, c_v	Specific heat at constant pressure and volume
C_p, c_v	Pressure coefficient
d_i	Damping coefficient
D	Feedthrough coefficient of the model structure
D_0, D_1, D_2	Feedthrough coefficients of the model structure
$\mathbf{D}_a$	Feedthrough matrix of the model structure
E^t, E^t	Total energy and energy per unit volume
$\mathbf{f}$	Inviscid flux functions
$\mathbf{F}$, $\mathbf{F}_{ij}$	Numerical fluxes
$\mathbf{F}^{\mathsf{I}}$, $\mathbf{F}^{\mathsf{II}}$, $\mathbf{F}^{\mathsf{ROE}}$, $\mathbf{F}^{\mathsf{LW}}$	First-order, second-order, Roe and Lax-Wendroff numerical fluxes
f_{at}	Rotation frequency after transient response
f_{max}	Maximum frequency of interest
$\mathbf{g}$	Boundary conditions
$\boldsymbol{h}$	Linear(ized) aerodynamic kernel function
I	Identity matrix
$\mathcal{I}$	Aeroelastic interface operator
I_H	Aileron moment of inertia about hinge line
J, J_{ga}	Cost function and genetic algorithm cost function

k	Time index
k_i	Stiffness coefficient
k_{max}	Maximum reduced frequency of interest
k_Ω	Reduced frequency of the blended step input
$\boldsymbol{K}$	Generalized stiffness matrix
L_∞	Reference length
m_i	Mass coefficient
M	Mach number
$\mathcal{M}$	Model structure or family
$\boldsymbol{M}$	Generalized mass matrix
m	Momentum
M_H	Aileron moment about hinge line
$\hat{\boldsymbol{n}}$	Local normal unit vector of the boundary
N	Order of the model structure
$\mathcal{N}$	Modal basis
N_{cells}	Ratio between the number of cells on the wing section and a reference value
N_f	Number of interfaces of the i-th cell
N_t	Number of samples of the input/output data
p, p_∞	Local and freestream pressure
q	Generalized displacements
$\boldsymbol{q}$	Generalized displacements
q_∞	Dynamic pressure
$\boldsymbol{Q}_a$	Generalized aerodynamic forces
$\mathcal{R}$	Linearized rotation operator
t	Time
t_k	Time instant
t_{max}	Half-period time of the blended input step
T	Period of the prescribed rotation
u	Generic training signal
u_a	Input of the aerodynamic low-order model
$\dot{\mathsf{u}}_a$, $\ddot{\mathsf{u}}_a$	First and second derivative of the input of the aerodynamic ROM model
u	Conservative variables for the Euler equations
$\boldsymbol{u}_a$, $\boldsymbol{u}_s$	Aerodynamic and structural nodes displacement
$\mathbf{u}_0$	Inital solution
$\mathbf{u}_a$	Input vectors of the aerodynamic low-order model
U, U_i, U_j	Solution of the governing flow equations
$\boldsymbol{v}$	Local velocities of moving boundaries
V_∞	Freestream speed
$\mathbf{x}$	Structural nodes position

x_H	x-coordinate of the hinge
x_a	State variables of the aerodynamic low-order model
$\boldsymbol{x}_H$	Position of the hinge
x_i	State variables of the internal second-order sub-systems
$\tilde{\mathsf{x}}_i$	Tentative state variables of the internal second-order sub-systems
x_{sw}	Shock wave position
y	Generic recorded output from experiment
$\hat{\boldsymbol{y}}$	Unit vector denoting the y-axis
y_H	y-coordinate of the hinge
y_a	Output of the aerodynamic low-order model
y_i	Generic identified output
z_H	z-coordinate of the hinge
β	Aileron deflection angle
ε	Identification error
ε_x	Identification error of the equation of state
ε_y	Identification error of the output equation
η	Non-dimensional time
η_{max}	Half-period non-dimensional time of the blended input step
γ	Specific heats ratio
Γ, Γ_{in}	Domain boundary and inlet boundary
Γ_{ij}, Γ_{i1}, Γ_{iN_f}	Interfaces of the i-th cell
ρ	Density
θ	Model parameters
$\bar{\omega}$	Prescribed training signal frequency
$\bar{\Omega}$	Prescribed frequency of blended step input
Ω	Spatial domain

List of Figures

List of Tables

Abstract

A computational study of non-classical aileron buzz is presented, which focuses on the modelling of the aerodynamics. To this end, a high-fidelity CFD model is employed and a reduced-order aerodynamic model is developed. The aeroelastic model is based on a two-dimensional wing section, in which a rigid aileron is integrated without gap. As far as the CFD-based calculations are concerned, the flow model of the Euler equations is chosen and it is coupled to the dynamics equation of the rigid rotation of the aileron, which are both implemented in the solver AeroFoam. The CFD-based direct simulations point out that the numerical solver is a reliable means for the analysis of aileron buzz, however care must be taken with respect to the grid details that might influence the solution. For instance, mesh refinement and size are crucial to obtain reliable results and the choice between a smoothed and non-smoothed grid has an influence on the system response, both quantitatively and qualitatively. As a matter of fact, grid details affect the simulation of shock dynamics, which is the driving mechanism for non-classical aileron buzz. On the other hand, a linear low-order model for the aerodynamics is developed, leveraging the idea of a parallel of second-order sub-systems. For the calculation of the model parameters a global optimization strategy is chosen after a brief comparison with other methods; such a method is based on a genetic algorithm. From the reduced-order model of the aerodynamic a low-order aeroelastic system is determined, which proves to be effective for a limited range of conditions. In fact, the linearity assumption is restrictive yet necessary, because it represents the first step in the development of a higher-fidelity model. Therefore, the work provides further insight in the numerical simulation of shock-dominated instability aeroelastic phenomena and blazes a trail for the development of a low-order model for the analysis of non-classical aileron buzz.

Keywords: aileron buzz, non-classical, CFD aeroelastic simulation, aerodynamic reduced-order model, AeroFoam

Sommario

Nel presente lavoro è presentato uno studio numerico del buzz di alettone di tipo non classico, con particolare attenzione alla modellazione dell'aerodinamica. A questo scopo viene impiegato un accurato codice CFD e allo stesso tempo viene sviluppato un modello ridotto dell'aerodinamica. Il modello aeroelastico è basato su una sezione bidimensionale di ala, all'interno della quale è integrato un alettone rigido senza fessura. Per quanto riguarda le simulazioni CFD, vengono scelte le equazioni di Eulero come modello fluido, le quali sono accoppiate all'equazione dinamica della rotazione rigida dell'alettone e implementate nel solutore prescelto AeroFoam. Tali simulazioni CFD mostrano che il solutore numerico è un mezzo affidabile per l'analisi del buzz di alettone, ciononostante occorre prestare attenzione ai dettagli della griglia di calcolo che possono influenzare la soluzione. Il raffinamento del dominio di calcolo e la sua dimensione, ad esempio, sono fondamentali per ottenere risultati affidabili e la scelta tra una griglia regolarizzata e non regolarizzata a cavallo della cerniera dell'alettone ha un'influenza sulla risposta del sistema, sia qualitativamente che quantitativamente. Di fatto i parametri della griglia di calcolo alterano la simulazione della dinamica dell'onda d'urto, che è il meccanismo chiave del buzz di alettone non classico. In opposizione, viene sviluppato un modello lineare di ordine ridotto dell'aerodinamica, sfruttando l'idea di un parallelo tra sotto-sistemi del second'ordine. Per il calcolo dei parametri del modello viene scelta una strategia di ottimizzazione globale a seguito di un confronto con altri metodi tradizionali; tale metodo è basato su un algoritmo genetico. A partire dal modello ridotto dell'aerodinamica, viene ottenuto il sistema aeroelastico di ordine ridotto, il quale risulta essere efficace per un intervallo limitato di condizioni. Infatti, l'ipotesi di linearità è restrittiva seppur necessaria, perchè rappresenta il primo passo nello sviluppo di modelli più accurati. Pertanto, il lavoro fornisce interessanti spunti nel campo della simulazione numerica di fenomeni di instabilità aeroelastica dominati da onde d'urto e pone le basi per lo sviluppo di modelli di ordine ridotto per l'analisi del buzz di alettone di tipo non classico.

Parole chiave: buzz di alettone, tipo non classico, simulationi aeroelastiche con CFD, modello ridotto aerodinamico, AeroFoam

Descrizione dell'attività

Si propone di seguito una breve descrizione del lavoro svolto.

Introduzione

Uno dei regimi di volo più critici per le analisi aeroelastiche è il campo transonico, nel quale si trovano spesso a volare aerei sia civili che militari. Limitazioni dell'inviluppo di volo derivano da instabilità dinamiche che nascono dalla mutua interazione tra forze elastiche, inerziali e aerodinamiche, come il flutter, il *buffeting* e i fenomeni di ciclo limite, che sono potenzialmente pericolosi per l'integrità e la sicurezza degli aeromobili. Tra questi fenomeni si trova il buzz di alettone, un'instabilità dinamica ad un grado di libertà che comporta oscillazioni autoeccitate della rotazione dell'alettone attorno al suo asse di cerniera. Il moto armonico della superficie di controllo è causato principalmente dalla dinamica delle intense onde d'urto e dagli effetti di interazione tra l'urto e lo strato limite. Prove sperimentali e in volo condotte negli anni 40 e 50 hanno permesso di ipotizzare che il fenomeno potesse essere associato ai differenti regimi di moto, dipendendo dal numero di Mach, dalla sezione dell'ala e dall'angolo di incidenza. A differenza di altre instabilità ad un grado di libertà, il buzz di alettone spesso culmina con oscillazioni divergenti di ampiezza estremamente elevata, raggiunte nel giro di pochi cicli e che possono portate a danni permanenti. Un esempio della pericolosità del buzz è un incidente avvenuto nel 2001 a bordo di un Learjet 25D, un *business jet* ad alte prestazioni, il quale ha incontrato un buzz di equilibratore che ha compromesso la sicurezza del volo. Oltre a problemi di sicurezza di volo, l'instabilità di buzz rappresenta un potenziale pericolo per i componenti della catena dei comandi di volo. Esso infatti è oggetto di investigazione durante la fase di certificazione dei velivoli e qualora causasse problemi di fatica ai componenti dell'attuazione dei comandi di volo, si vedrebbe necessaria una sua soppressione con sistemi di controllo attivo. Di conseguenza, sviluppare e migliorare gli strumenti di analisi per lo studio del buzz è di interesse durante la fase preliminare del progetto di un velivolo, in modo da stimare gli effetti di tale instabilità e definire strategie per evitarla. Inoltre, il fenomeno ha anche interesse teorico, dal momento che una

teoria comprensiva del problema non è mai stata raggiunta.

Oltre agli studi in galliera del vento, un'opzione percorribile è quella di analizzare il fenomeno tramite la modellazione numerica. A tal proposito, è possibile ricorrere agli strumenti della Fluidodinamica Computazione (CFD). Di fatto, le non linearità legate all'aerodinamica del buzz di alettone richiedono tecniche di analisi raffinate e di maggior qualità. In generale, infatti, gli strumenti lineari utilizzati in ambito industriale, basati su modelli di flusso a potenziale, non sono in grado di fornire stime accurate in regime transonico. Invece, i codici CFD sono sicuramente più accurati nell'affrontare problemi caratterizzati da forti nonlinearità e sono stati ampiamente sviluppati per calcoli aeroservoelastici. In tal senso i modelli di calcolo CFD vengono accoppiati con opportuni modelli strutturali del velivolo. Questa branca della meccanica delle strutture è spesso definita Aeroelasticità Computazionale e rappresenta un campo di ricerca altamente interdisciplinare. In questo contesto la modellazione numerica deve affrontare diverse difficoltà perchè, oltre al costo computazionale delle singole soluzioni aerodinamiche e strutturali, l'accoppiamento della soluzione aeroelastica richiede tecniche in grado di trattare contorni e griglie mobili e poter applicare l'interfaccia aeroelastica. Oltre a questo, le non linearità del problema comportano che la soluzione sia fortemente affetta da qualsiasi parametro del solutore numerico, come la dimensione del domino di calcolo e il suo raffinamento, oltre alla descrizione geometrica. Tuttavia, quando vengono eseguite queste simulazioni accoppiate, la soluzione CFD non stazionaria richiede generalmente un tempo di calcolo maggiore ad ogni passo temporale, mentre il solutore strutturale è più veloce. Perciò, se si riuscisse a sviluppare un accurato ed efficiente sostituto del solutore CFD, la predizione dell'instabilità aeroelastica sarebbe molto più efficiente dal punto di vista computazionale. I modelli in grado di sostituire un sistema dinamico sono definiti in inglese *Reduced-Order Models* (ROM), ovvero modelli di ordine ridotto, e rappresentano un'interessante alternativa alle simulazione CFD, non solo per quelle applicazioni numeriche dove vengono provate numerose condizioni (ad esempio, ottimizzazioni multi-obiettivo), ma anche per l'analisi delle caratteristiche essenziali di un sistema dinamico complesso. Ad oggi esistono una grande varietà di metodi in grado di sviluppare modelli efficienti che si sostituiscano agli algoritmi CFD. Una possibilità è quella di definire un modello matematico di ordine ridotto per le relazioni ingresso/uscita della soluzione CFD instazionaria, utilizzando la teoria dei sistemi. Concettualmente, si potrebbe pensare al solutore instazionario CFD come ad un sistema dinamico che traduce il moto della struttura in carichi aerodinamici. Un'efficiente tecnica per ottenere i modelli ridotti è l'identificazione dei sistemi, un processo che costruisce un modello matematico del sistema dinamico basato su un insieme di dati misurati dallo stesso. Questa metodologia è usata per identificare i parametri del modello che meglio approssimano l'insieme di dati registrati dal sistema dinamico. Il risultato è un modello

algebrico che rappresenta una trasformazione matematica tra gli ingressi e le uscite del sistema dinamico.

Il presente lavoro presenta e discute la modellazione numerica del buzz di alettone. L'attenzione è posta sulla rappresentazione del sotto-sistema aerodinamico, la quale è svolta in due differenti modi: da un lato è presentato un metodo per l'analisi del buzz di alettone basato su un codice CFD, dall'altro viene sviluppato un modello ridotto, del quale è studiata l'applicabilità.

Aileron buzz

Il fenomeno di buzz di alettone è un'instabilità dinamica che comporta oscillazioni armoniche della superficie di controllo. Varie tipologie di buzz sono state osservate durante le campagne di prove sperimentali e di prove in volo effettuate nei primi decenni dalla scoperta del fenomeno. In particolare, il buzz è solitamente classificato in tre tipologie. Il primo tipo di buzz o buzz di tipo A è principlamente causato dall'interazione dello strato limite con le onde d'urto che si muovono periodicamente rimanendo sempre davanti all'asse di cerniera della superficie di controllo e causando la separazione dello strato limite. Il secondo tipo di buzz o buzz non classico ha invece una dipendenza più immediata dal movimento delle onde d'urto che sono posizionate sulla superficie di controllo o che si muovono a cavallo dell'asse di cerniera. La viscosità in questo caso ha effetti secondari. Infine, il terzo tipo di buzz o buzz di tipo C riguarda l'oscillazione armonica che si instaura quando le onde d'urto si trovano al bordo d'uscita della superficie di controllo. Si evince quindi da questa breve descrizione che l'analisi della posizione e della dinamica delle onde d'urto sia cruciale nella modellazione del buzz.

Modello CFD

Il modello aeroelastico basato sul codice CFD è fondato sull'implementazione numerica delle equazioni di Eulero bidimensionali ed un modello rigido per la superficie mobile. Le ragioni che muovono questa scelta sono legate alla natura del fenomeno. Per quanto riguarda il modello fluido, il buzz non classico è infatti un fenomeno dominato dalla dinamica delle onde d'urto, piuttosto che dagli effetti viscosi dell'interazione urto-strato limite e pertanto il modello inviscido delle equazioni di Eulero è appropriato per la simulazione. Inoltre, essendo il buzz associato ad un solo grado di libertà che non interagisce significativamente con i gradi di libertà flessibili della struttura alare, la scelta di una superficie di controllo rigida è opportuna per la corretta rappresentazione del fenomeno. Inoltre, quest'ultima è libera di ruotare attorno al suo asse di cerniera senza effetti di cedevolezza o di dissipazione. L'accoppiamento debole tra l'aerodinamica

e la struttura è ottenuto mediante due differenti approcci, i quali portano a diverse descrizioni del dettaglio geometrico della cerniera dell'alettone. Il solutore AeroFoam è usato per la simulazione diretta del problema aeroelastico e diverse griglie di calcolo con raffinamenti opportuni sono utilizzati. In particolare, i risultati delle simulazioni numeriche dirette mostrano una sensibilità della risposta del sistema aeroelastico rispetto al raffinamento della griglia di calcolo e alla sua dimensione, ma anche rispetto al dettaglio geometrico dell'integrazione della superficie di controllo all'interno dell'ala. Il motivo di ciò è legato al ruolo predominante che riveste nel fenomeno aeroelastico la dinamica delle onde d'urto, la quale richiede una accurata rappresentazione affinchè sia correttamente catturata. Inoltre, l'impostazione numerica nel suo complesso risulta un affidabile strumento per la predizione della stabilità del buzz di alettone.

Modello ROM

I risultati numerici forniscono informazioni per lo sviluppo di un modello ridotto del sotto-sistema aerodinamico. Infatti, per il calcolo del modello ridotto la tecnica dell'identificazione dei sistemi è utilizzata, la quale prevede una fase sperimentale in cui vengono raccolti i dati relativi all'ingresso e all'uscita del sistema ed una fase di calcolo dei parametri del modello. La fase di raccolta dei dati nel caso di identificazione numerica è eseguita tramite una simulazione CFD a rotazione imposta. La rotazione, ingresso del sistema, è scelta opportunamente in modo da eccitare il sistema nella banda di frequenze di interesse, ma di non forzarlo eccessivamente. Per il problema in esame è scelto uno scalino raccordato. In seguito, il modello deve essere definita, il quale è costruito sull'assunzione di linearità del sistema. Inoltre, la struttura del modello è basata sull'idea di una "scatola grigia", ovvero un modello che contenga alcune informazioni sul sistema reale. In particolare, nel caso in esame sono state inserite diverse caratteristiche del sistema aerodinamico osservate in fase di simulazione diretta, quali la proprietà di asintotica stabilità del sistema e il carattere oscillatorio della risposta. L'identificazione dei parametri del modello è invece ottenuta per mezzo di una tecnica di ottimizzazione globale, ovvero un metodo genetico appositamente costruito e adeguato al problema. L'identificazione del sotto-sistema aerodinamico si dimostra efficace e capace di raggiunge risultati affidabili, mentre il modello ridotto è capace di predire l'instabilità e rappresentare i risultati del modello aerodinamico basato sul codice CFD, sebbene con un intervallo di applicabilità più limitato. Le problematiche del modello sono principalmente ascrivibili all'assunzione di linearità, la quale limita la rappresentazione effettiva dello scambio energetico tra la struttura e l'aerodinamica.

Sviluppi futuri

Il primo sviluppo futuro di questo lavoro è l'implementazione di un modello ridotto non lineare: le basi di questo modello sono già state poste nel presente lavoro e si ritiene che la semplice adozione di un sostituto polinomiale dell'ingresso sarebbe sufficiente a cogliere il comportamento non lineare, predicendo perciò con migliore accuratezza il ciclo di buzz. A partire da ciò, si potrebbe ricostruire con tecniche simili a quelle utilizzate in questo lavoro il legame tra i parametri del modello e il numero di Mach o l'incidenza di volo. La realizzazione nello spazio degli stati poi rende più facile l'implementazione di un'eventuale strategia di controllo del fenomeno. Riguardo al modello CFD, possibili lavori futuri possono focalizzarsi nell'analisi tridimensionale viscosa del buzz. Come già introdotto, considerando gli effetti tridimensionali e la viscosità si avrà una sicura influenza sul punto di comparsa del buzz, il quale sarà spostato a differenti numeri di Mach ma è probabile che le principali caratteristiche delineate in questo lavoro rimangano tali. L'inclusione di questi aspetti porta da un lato a simulazioni numeriche più accurate e dall'altro porta ad arricchire i modelli di ordine ridotto. Inoltre, si potrebbe anche studiare il buzz di tipo A e le sue differenze anche in termini di modello ridotto rispetto al buzz non classico. In conclusione, il lavoro fornisce interessanti spunti nel campo della simulazione numerica di fenomeni di instabilità aeroelastica dominati da onde d'urto e pone le basi per lo sviluppo di modelli di ordine ridotto per l'analisi del buzz di alettone di tipo non classico.

Introduction

One of the most challenging flows for aeroelastic analysis is the transonic speed range, in which civil and military aircraft often fly. Flight envelope limitations regarding the stability of wings in such regime are usually caused by dynamic instabilities arising from the mutual interaction among elastic, inertial and aerodynamic forces, such as flutter, buffeting and limit-cycle-oscillations phenomena, which are potentially dangerous for the integrity and safety of the aircraft. Among them is aileron buzz, a one-degree-of-freedom flutter involving self-excited oscillations of aileron rotation about its hinge. The sustained, harmonic behaviour of the control-surface is mainly caused by the strong shock wave dynamics and shock-boundary layer effects. Experimental and flight tests in the 40s and 50s suggested that the phenomenon could be associated to different regimes of flow, depending on the Mach number, wing section and angle of attack. Unlike other single-degree-of-freedom instabilities, aileron buzz often results in explosive oscillations of very large amplitudes within a few cycles, that lead to permanent damages. An example of the detrimental action of control-surface buzz is an incident occurred in 2001 on a Learjet 25D, a high-speed business jet aircraft, which encountered elevator buzz during a flight test [1]. The instability caused the total loss of the elevators and, although the experienced crew managed to estabilish pitch control by using horizontal stabilizer pitch trim, the jet aircraft was destroyed on impact with terrain while landing. Beyond flight safety, which is not greatly compromised in modern airliners thanks to the hydraulically operated (i.e. very stiff and irreversible) controls, buzz instability still represents a potential hazard for flight control system components: in fact, fatigue issues might arise from the high-frequency excitation of the aileron buzz. Hence it is interesting to develop and improve the analysis tools for the study of buzz at the design stage, thereby evaluating the effects of the instability and defining ways to avoid them. In addition, from a theoretical standpoint, the problem is not without interest: a theoretical treatment is out of reach and the attempted studies based on numerical and experimental simulations do not provide complete description of the problem.

Beside the experimental testing, a viable option for the analysis is that of the numerical modelling of the phenomenon. Hence, it is possible to resort on the Computational Fluid Dynamics (CFD) tools. As a matter of fact, the aerodynamic

nonlinearities involved in aileron buzz, require finer and higher-quality analysis techniques. In general, the standard industrial linear tools, based on potential flow models, are not capable of giving good prediction in transonic regime. Instead, high-fidelity CFD codes can be very accurate and have been extensively developed for aeroservoelastic computations. To this end high fidelity Computational Fluid Dynamics models must be adopted and coupled with proper structural models of the airplane itself. This branch of continuum mechanics is usually referred to as Computational Aeroelasticity, a highly interdisciplinary and very active reasearch field. In such a context the numerical modelling faces several difficulties, because beyond the computational cost of the aerodynamic and structural solution alone, the coupling in the aeroelastic solution requires techniques capable of dealing with moving boundaries, moving grids and aeroelastic interfaces. In addition to this, the nonlinearity of the problem causes the solution to be greatly affected by every numerical ingredient, such as mesh size and refinement, as well as by the geometry description.

Nevertheless, when running these coupled simulations, the unsteady CFD solution usually requires the greatest amount of CPU time at each time step, while the structural dynamics solver is faster. Thus, if an accurate and efficient substitute for the CFD solver could be developed, aeroelastic instability predictions would be much more computationally efficient. Such models are referred to as Reduced-Order Models and they provide an attractive alternative to CFD not only for those numerical applications where several conditions are tested (e.g. stability prediction and multi-objective optimization), but also in the analysis of the essential features of a complex dynamic system. To date, a variety of methods exists for developing an efficient surrogate model of a CFD algorithm. A possibility is to define a mathematical low-order model for the input/output relationship of the unsteady CFD solution using systems theory. Conceptually, a possible abstraction of the unsteady CFD solution implemented in an aeroelastic analysis is that of a dynamic system which maps the motion of the structure into the aerodynamic loads. An efficient system modeling technique is system identification, which is a process for obtaining a mathematical model of a dynamic system based on a set of measured data from the system. This methodology is used to fit the parameters of a model structure to a set of recorded data from the dynamic system. The result is an algebraic model that is a mathematical map between the input and the output of the system.

The current work presents and discusses the numerical modelling of a particular type of aileron buzz, namely non-classical aileron buzz. The focus is on the representation of the aerodynamic sub-system in two different ways: on one hand a CFD-based method for the analysis of the aileron buzz is presented and on the other a low-order model is developed, based on a reduced-order representation of the aerodynamics. In particular, in Chapter 1 the phenomenon of interest is pre-

sented together with a discussion of the main features and difficulties encountered when dealing with transonic flows. The CFD aerodynamic model is then defined in Chapter 2, where the governing equations and the numerical implementation are discussed. Chapter 3 presents the complete aeroelastic model, which is built on the CFD aerodynamic sub-system and the rigid structural model of the aileron. Also the numerical integration between the previous two is discussed in detail. In Chapter 4 a convergence analysis shows how grid refinement affects the aeroelastic response and the effect of the integration of the control-surface in the main wing on the system response is studied. Finally, Chapter 5 presents the discussion on the reduced-order model for the aerodynamic sub-system and the resulting comparison with some benchmark results.

Chapter 1

Aileron buzz

In the aeroelastic literature, the term *aileron buzz* is used to denote a single-degree-of-freedom flutter involving self-excited oscillations of aileron rotation occurring in transonic and low supersonic flight. The characteristics of such instabilty are strictly tied to the behaviour of the flow in that regime, which typically involves shock waves dynamics, boundary layer separation and mutual interference between the previous two. As a result, a clear understanding of the instability arising in this regime also requires to analyse the essential features of the aerodynamics involved. In particular, the present chapter is divided into two sections: Section 1.1 presents the aerodynamic phenomena arising in transonic flow over a non-symmetrical airfoil and in Section 1.2 the general causes, characteristics and treatments of aileron buzz are discussed.

1.1 Transonic flow

The transonic regime is defined as the range of free stream Mach number, for which the flow exhibits regions inside the domain with speeds lower, equal to or higher than the sonic value, i.e. the local speed of sound. As a matter of fact, the main aspect of transonic flow is the simultaneous occurrence of locally subsonic and supersonic regions, possibily separated by irreversible phenomena, such as shock waves. This feature makes it one of the most difficult flow to treat within the compressible flows, because the governing equations have different natures: subsonic flows are associated to elliptic equations, while in supersonic flows the governing equations have hyperbolic features.

Formally, the onset of the transonic regime is usually placed at a particular Mach number, namely the critical Mach number M_{cr}, which is defined as the Mach number for which a point P exists on the upper surface of the airfoil where the expansion of the flow yields sonic speed, i.e. $M_P = 1$ (Fig. 1.1 (a)). The location of point P usually depends on the airfoil geometry and the angle of attack and

the resulting critical Mach number generally decreases with increasing maximum thickness of the airfoil or angle of attack. On the other hand, a conventional upper boundary for the transonic regime doesn't exist; a typical transonic speed range for a slender body, such as an airfoil, is $0.8 < M_\infty < 1.2$.

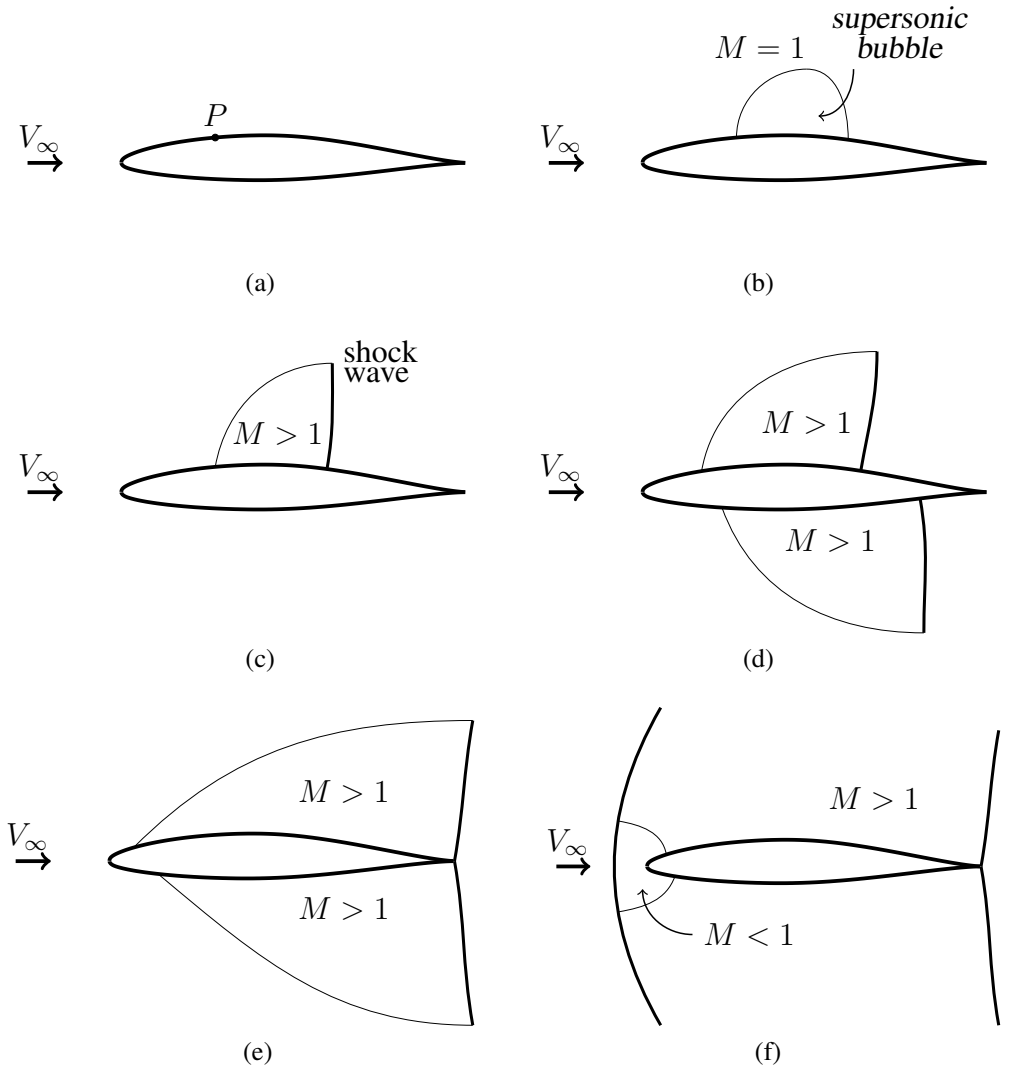

Figure 1.1: Features of ideal, inviscid flow in transonic and low supersonic regime.

In the transonic regime, different behaviours are detected according to the free stream Mach number. Here is the evolution of an inviscid and non-conductive flow over a non-symmetrical airfoil with increasing Mach number:

- At Mach numbers slightly higher than the critical Mach number, close to point P a region in which the flow is locally supersonic appears, which is

usually referred to as *supersonic bubble* (see Fig. 1.1 (b)). The region is surrounded by subsonic flow and it is enclosed by a line with constant pressure and sonic Mach number, called *sonic line*. In the rear part of the supersonic bubble a shock wave might occur. As a matter of fact, the expansion waves on the upper surface close to the leading edge are mirrored by the sonic line and after the reflection generate compression waves. In turn, depending on free stream Mach number, geometry and angle of attack, the compression waves might come together and merge into a shock wave, as sketched in Fig. 1.1 (c) .

- With further increase in Mach number the supersonic bubble spreads on a wider region of the upper surface, thereby yielding a more intense and rearward shock wave. In addition, another supersonic bubble occurs on the lower surface (Fig. 1.1 (d)), which rapidly develops and moves aft, until the associated shock wave reaches the trailing edge of the airfoil. Thus, depending on the airfoil geometry, there is a restricted range of subsonic free stream Mach numbers for which the flow is supersonic on the airfoil (except for a small area close to the leading edge) and both shock waves occur at the trailing edge (Fig. 1.1 (e)).

- Finally, for supersonic free stream Mach numbers the flow deeply changes: ahead of the airfoil a detached bow shock wave occurs, after which a small region of subsonic flow appears close to the airfoil leading edge, as presented in Fig. 1.1 (f). Everywhere else the flow is supersonic. With increasing Mach number the subsonic region progressively shrinks, but doesn't completely disappear, unless the leading edge is sharp.

From this description, it is evident that the transonic speed range is complicated by the presence of shock waves and simultaneous coexistence of subsonic and supersonic condition. However, further nonlinearities arise in this regime due to the role of viscosity. The interaction between shock waves and boundary layer has several consequences: the shock wave might change layout, yielding a coalescence wave called *lambda waves*, the shock might induce boundary layer separation (Fig. 1.2), causing shock-induced stall, or the interaction might yield unsteady phenomena such as *buffeting*. The mechanism of unsteady shock-boundary layer interaction is due to a mutual interference. Due to the strong adverse gradient caused by the shock wave, the flow is likely to transit to turbulent state or separate behind the shock wave. However, the separated flow changes the pressure field, thereby decreasing the strength of the shock. The consequent forward movement of the shock might encourage flow reattachement, which in turn, increasing the pressure jump across the shock, would close the loop. Clearly, the unsteady interaction between shock waves and boundary layer causes significant variation in time of the

aerodynamic loads. Such variation not only affects the airplane rigid movements, thereby influencing stability and control properties, but also it might couple with the structure flexibility, yielding instability phenomena, such as transonic flutter.

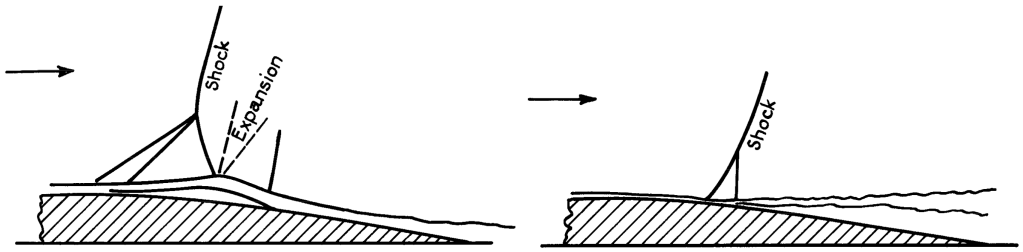

(a) Lambda wave (b) Shock-induced transition and separation

Figure 1.2: Sketch of typical phenomena of boundary layer and shock wave interaction (from Ref. [2]).

In conclusion, transonic regime is dominated by nonlinear pheomena, which involves shock wave dynamics, shock-induced separation and shock-boundary layer interaction.

1.2 Aileron buzz

According to Lambourne [3], aileron buzz was first encountered in high-speed subsonic flight in 1945. During flight testing of the P-80 jet fighter aircraft, aileron oscillations were detected, ranging from a spasmodic low-amplitude buzz to a motion so violent that resulted in the permanent damage to the control-surface [4]. Since flight tests proved hazardous, Erickson and Stephenson [5] undertook wind-tunnel tests of a P-80 half-span wing mounted in the Ames 16-Foot Wind Tunnel and concluded that aileron buzz was a one-degree-of-freedom flutter, thereby excluding the interaction between the aileron and the wing flexible degrees-of-freedom. In addition, the phenomenon appeared to be associated to the motion of shock waves to the extent that the fore and aft motion of these shock waves on the wing surface accompanied the control-surface oscillations. Typically an oscillating control surface gave rise to an oscillating shock, which in turn produced an oscillating pressure field resulting in an oscillating control surface that gave rise to an oscillating shock and so forth. In particular, as confirmed by a later wind-tunnel investigation by Lambourne [2] the downward movement of the aileron was accompanied by a rearward movement of the upper shock wave and a forward movement of the lower shock; on the contrary, with aileron moving upwards, the shock wave on the upper surface moved fore and the lower shock

wave moved aft. The cycle obtained in the investigation of buzz for a symmetrical airfoil is presented in Fig. 1.3.

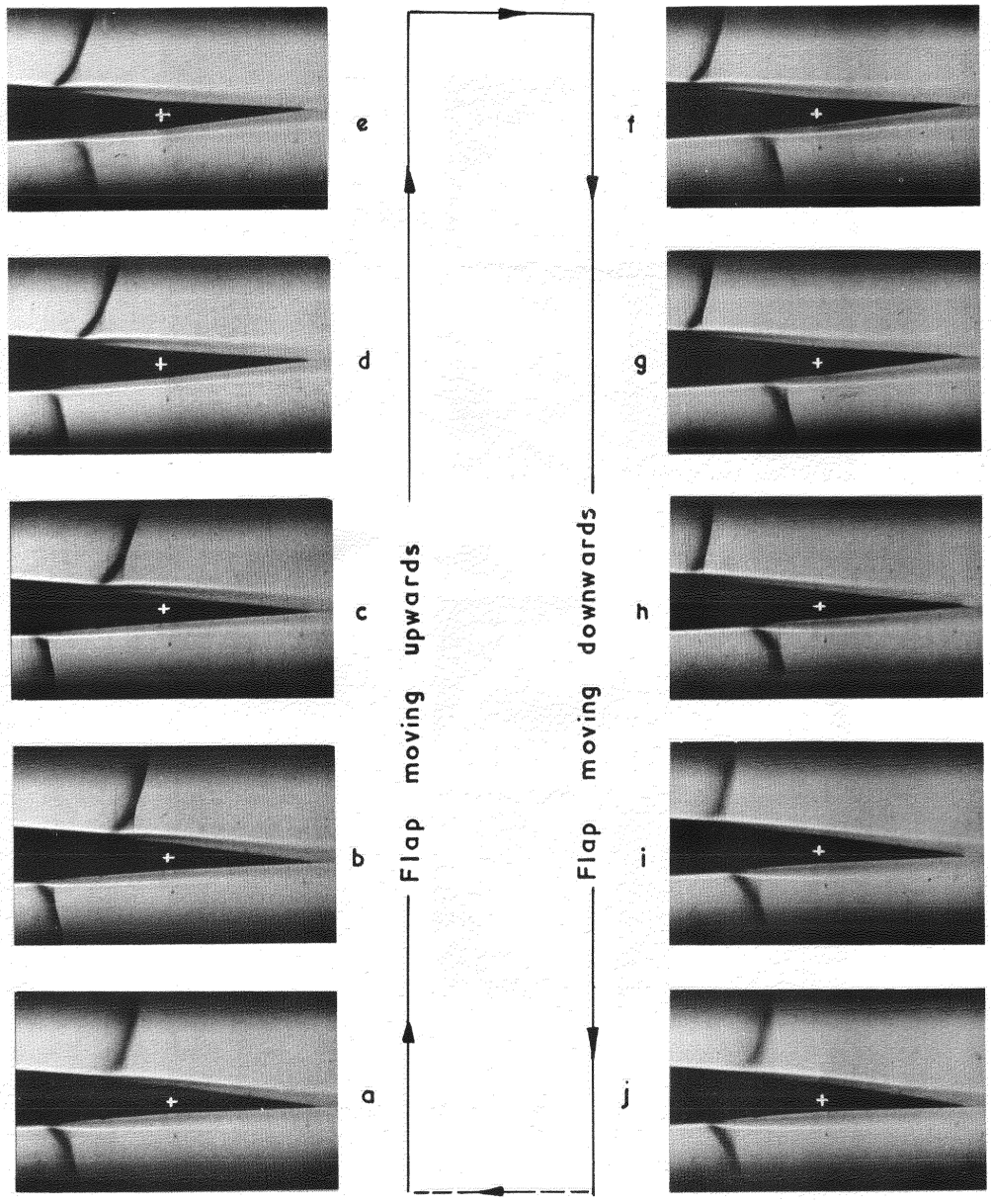

Figure 1.3: Buzz cycle for a symmetrical airfoil during wind-tunnel investigation by Lambourne [2].

This coupling between shock motion and aileron deflection is one of the most essential features of aileron buzz. Another important aspect that was evidenced by 1940s and 1950s wind-tunnel investigations, is the phase difference between

the motion of the shock wave and the deflection of the control-surface. The phase lag is identified with the time lag required for the pressure changes resulting from the flap motion to propagate and modify the aerodynamic load which drives the aileron.

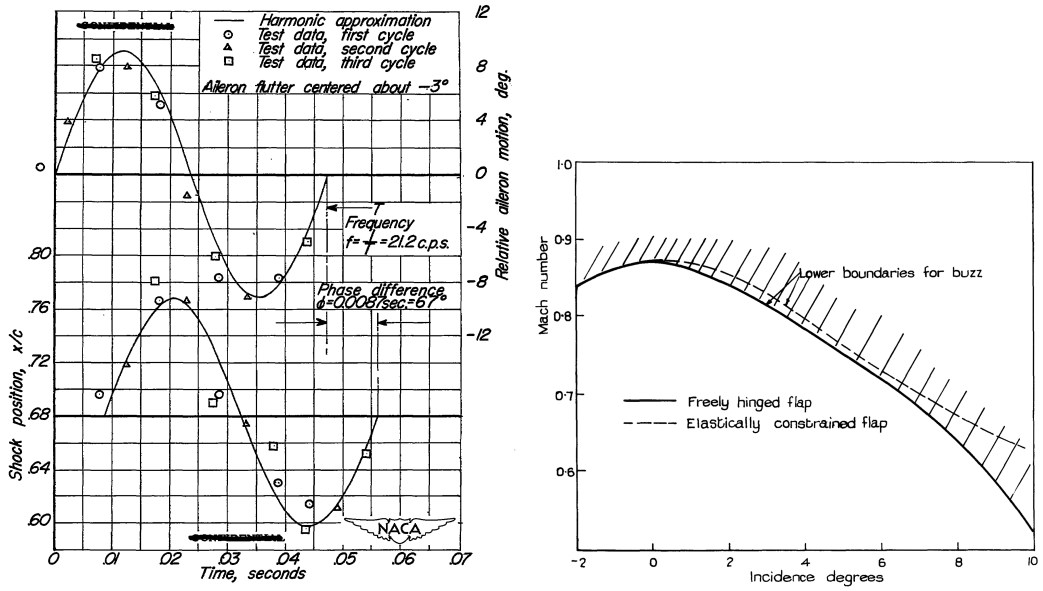

(a) Phase lag (from Ref. [2])

(b) Buzz boundary (from Ref. [5])

Figure 1.4: Typical features of aileron buzz.

Furthermore, wind-tunnel investigations also suggested that the phenomenon could be associated to different regimes of flow, depending on the Mach number, wing section and angle of attack. In particular, for a given wing the region in which buzz is likely to occurr is described in the plane identified by Mach number and angle of attack and it is such that with increasing incidence the Mach number for buzz onset decreases. In Ref. [3], Lambourne proposed a classification into three types, namely Type A, Type B and Type C, sketched in Fig. 1.5 from top to bottom.

(A) The first type comprises aileron oscillation phenomena encountered at Mach numbers slightly higher than the critical Mach number, in which shock waves stand ahead of the hinge line. In this case the flow on the entire control-surface is subsonic and buzz is driven by shock-boundary layer unsteady interaction and shock-induced separation ahead of the control surface.

(B) At higher Mach numbers the upper and lower shock waves move aft, as dicussed in Section 1.1. When one or both shock waves occur between the

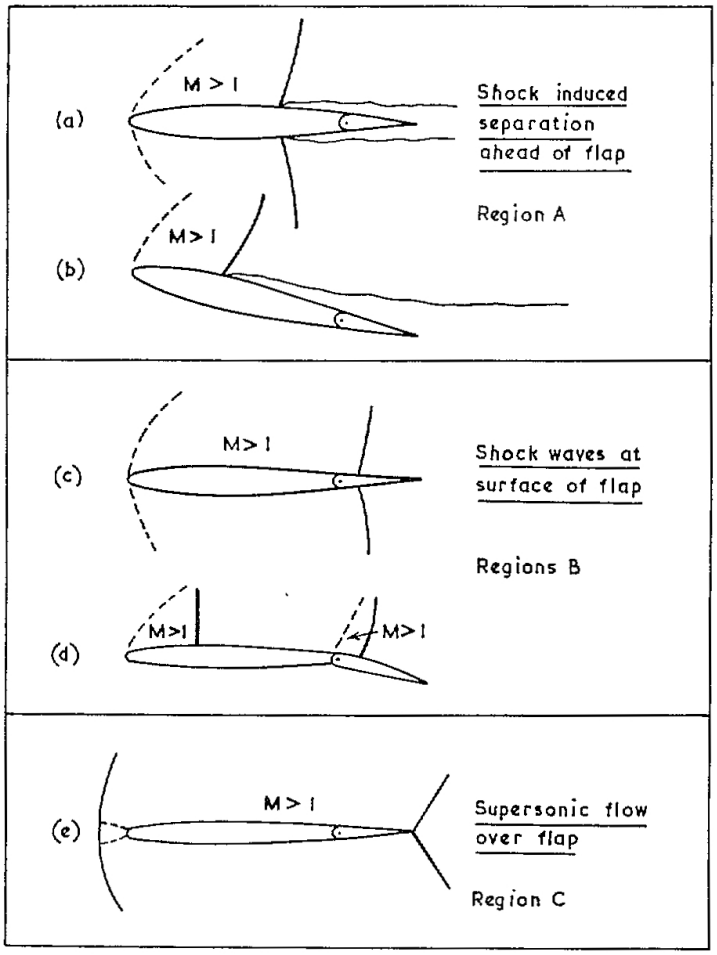

Figure 1.5: Classification of aileron buzz (figure from Ref. [3]).

hinge line and the aileron trailing edge and keep moving fore and aft, the instability is labelled as Type B buzz. In this condition the flow over the control-surface is mixed supersonic and subsonic.

(C) With further increase in Mach numbers the flow is supersonic over the entire control surface and the main shock waves occur at the aileron trailing edge. This kind of buzz is labeled as Type C and doesn't seem to involve shock-boundary layer interaction. In general, this particular type of buzz is associated to the negative damping predicted by potential-flow theories for an infinitely thin airfoil pitching about its leading edge for Mach numbers between 1 and 1.4. Although this theory might offer a possible explanation of Type C buzz, it should be noted that it has serious limitations, due to inability to treat shock dyamics, non-null angle of attack and aileron thick-

ness.

With respect to Type B, Lambourne explained that boundary layer separation was observed, but it didn't appear to be a driving mechanism. A later work by Bendiksen [6] supported the idea that the main drive of aileron buzz in such condition was the dynamics of shock waves moving on the aileron surfaces. After that, Type B buzz was labelled *nonclassical buzz*, in order to emphasize the minor role of boundary layer separation and shock-boundary layer interaction, which are instead pivotal in Type A mechanism. However, viscosity has an indirect effect in the non-classical aileron buzz. In particular, considering an airfoil operating at a small angle of attack at Mach number slightly higher than the critical Mach number M_{cr}, the fore and aft movement of the upper shock wave is considerably slowed down, due to shock-induced boundary layer separation. As a result, with increasing Mach number (i.e., increasing shock strength) the viscous effects and the mutual shock-boundary layer interference would inhibit the shock motion, whereas an inviscid model would predict growing amplitude in the shock wave motion.

Despite a number of wind tunnel studies already mentioned, a complete theory for control-surface buzz was never developed, especially for Type B buzz. The phenomenon usually receives minor discussion and it is generally grouped with "other aeroelastic phenomena", for which there are not theories able to successfully predict flutter boundaries. Because a theoretical treatment appears to be out of reach, it is necessary to resort on experimental studies or direct numerical simulations for analysis. With regard to the latter, few such numerical simulations have been attempted in the past, among which the work by Steger and Bailey [7], Bendiksen [6], Howlett [8] and the numerical investigation of rudder buzz by Fulgsang et al. [9]. The reason for the limited interest in aileron buzz is that the phenomenon causes limited practical problems in modern aircraft that use hydraulically operated (i.e. very stiff and irreversible) controls. However, fatigue issues in the components of the flight control system might arise and are critical. Also, smaller aircraft such as business jet aicraft proved to suffer from this problem. Furthermore, from a theoretical standpoint, the problem is not without interest. There are very few single-degree-of-freedom instabilities in the field of aeroelasticity, which require deviations from potential flow models. Examples are stall flutter phenomena associated with helicopter rotors and jet engine compressors blades. Because these are essentially single-degree-of-freedom instabilities, they tend to be soft and not as dangerous and destructive as, for example, coupled bending-torsion flutter on aircraft wings. Aileron buzz is an exception and often results in explosive instabilities, yielding very large amplitudes within a few cycles and permanent damages.

Chapter 2

Aerodynamic Model

In the analysis of an aeroelastic system, the aerodynamics plays a key role, because it provides the load acting on the structure. This is particularly true for a one-degree-of-freedom flutter in transonic regime, such as aileron buzz, because in order to develop an appropriate model of the phenomenon a linear and simple structural model is sufficient, whereas a nonlinear aerodynamic model is strictly required. As a result it is necessary to resort to more sophisticated mathematical models and numerical methods within the research field of Computational Fluid Dynamics (CFD), which is nowadays replacing the standard industrial tools based on potential flow models. A sustained drive in this way over the last 30 years progressed from transonic small disturbance and full potential through Euler flow simulations and is now reaching a point where complex configurations of real vehicles can be modeled and studied using a variety of Navier-Stokes solvers [10]. Of course, this progress was made possible by the increasing computational capability of modern computers and the improving efficiency of CFD numerical schemes. Nevertheless, the counterpart of high-accuracy solvers, such as CFD codes, is the higher computational costs in terms of work and memory with respect to the linearized tools. For instance, the Navier-Stokes equations, which provide the complete model of a flow, aren't usually integrated *tout court* for large-scale or design problems in which multiple configurations ought to be examined. As a matter of fact, the solution would require a severe computational effort and in some cases even the employment of the less expensive Reynolds-Averaged Navier-Stokes equations might be troublesome. Therefore, it is necessary to identify the mathematical model and numerical method capable of providing the best compromise between accuracy of the results and computational efficiency, depending on the objective of the numerical study.

The current chapter is aimed at defining and presenting the aerodynamic CFD model, which is the backbone of the aeroelastic model that is presented in the next chapter. In addition the numerical implementation is discussed in terms of space and time discretization, aerodynamic mesh and solver.

2.1 Governing Equations

In the study of aileron buzz, nonlinear flow models are strictly required due to the presence of unsteady shock waves and possible shock-boundary layer interaction. As a matter of fact, the presence of shock waves clashes with the assumption of small perturbation on which the potential models are based. In addition, because the intention of the work is the study of non-classical aileron buzz, in which shock dynamics is the main drive (as discussed in Chapter 1), the mathematical model of the Euler equations is chosen, which is also widely exploited for aeroelastic instability problems [6, 11]. Viscosity would no doubt contribute to the phenomenon by affecting the shock position, but will be neglected in the present study.

2.1.1 Euler equations

In general, the model of the Euler equations is exploited, when the boundary layer theory is assumed and when compressibility effects are very important. The boundary layer assumption is adopted for high Reynolds number flows surrounding and passing over aerodynamic bodies; in this condition, it is reasonable to assume that viscous diffusion and thermal conduction are restricted to a very thin region close to the body, namely the *boundary layer*, whereas the flow outside such layer can be approximated as inviscid and non-conductive. Disregarding the very thin boundary layer, an inviscid non-conductive model can be employed inside the entire domain, leaving the *no-slip condition* at the wall, which states that the fluid will have zero velocity relative to the boundary, and considering the *no-penetration condition*, where the fluid velocity normal and relative to the wall is set to zero and the fluid velocity parallel to the wall is unrestricted. Flow models that have such features are the potential flow model and the *ideal gas* model, that is an inviscid, non-conductive gas, for which the Euler equations hold. In addition, the Euler equations are capable of modeling and capturing the compressibility effects, that have a key role in the transonic regime. As a matter of fact, shock waves occurrence and dynamics are crucial to the aeroelastic instabilities onset and need an accurate predicition, as already pointed out in Chapter 1. Furthermore, it is worth recalling that, beyond the *ideal gas* model assumption, the Euler equations hold when thermodynamic and chemical local equilibrium exists, the gas is conceived as a continuum and volume forces are neglected. These assumptions are reasonable and adopted in flows such as the one the present work is focusing on.

The system of the Euler equations in conservative form with Eulerian formulation is the following

$$\frac{\partial}{\partial t}\mathbf{u} + \nabla \cdot \mathbf{f}(\mathbf{u}) = 0 \qquad \forall\, (\boldsymbol{x}, t) \in \Omega \times [t_1, t_2], \tag{2.1}$$

where $\Omega \subseteq \mathbb{R}^d$ and $[t_0, t_f] \subseteq \mathbb{R}^+$ are respectively the d-dimensional spatial do-

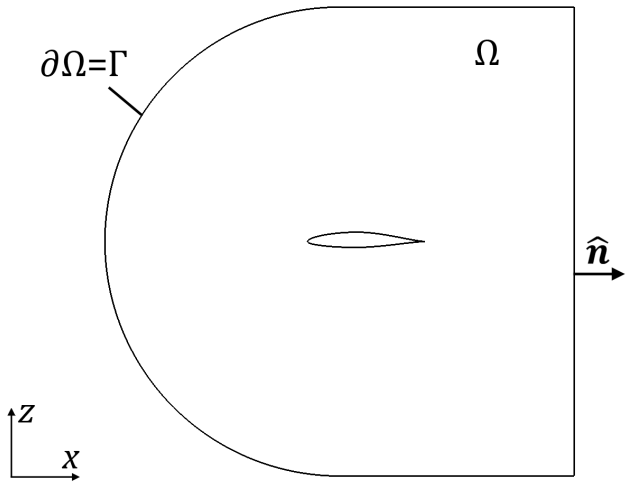

Figure 2.1: Spatial domain.

main and the time interval in which the equations are integrated (see Fig. 2.1). Vector $\mathbf{u}(\boldsymbol{x}, t) = \{\rho,\ \mathbf{m},\ E^t\}^T$ stores the conservative variables, i.e. density ρ, momentum $\mathbf{m}$ and total energy per unit volume E^t, which represent the solution of Eqn. (2.1) and depend on position $\boldsymbol{x}$ and time t; vector $\mathbf{f}(\mathbf{u})$ includes the inviscid flux functions, defined as follows:

$$\mathbf{f} = \left\{ \mathbf{m},\ \frac{\mathbf{m} \otimes \mathbf{m}}{\rho} + p(\mathbf{u})\ I,\ \frac{\mathbf{m}}{\rho}\left(E^t + p(\mathbf{u})\right) \right\}^T, \tag{2.2}$$

where p is pressure and I is the identity matrix of size $d \times d$. The governing equations also have an integral form, that is

$$\frac{\mathrm{d}}{\mathrm{d}t} \int_\Omega \mathbf{u}\ d\Omega + \oint_\Gamma \mathbf{f}(\mathbf{u}) \cdot \hat{\boldsymbol{n}}\ d\Gamma = 0, \tag{2.3}$$

where $\Gamma = \partial\Omega \subseteq \mathbb{R}^{d-1}$ represents the boundary having normal unit vector $\hat{\boldsymbol{n}}(\boldsymbol{x})$, outwards pointed. The problem isn't complete though, because not only initial and boundary conditions must be set, but also Eqn. (2.2) requires the definition of the equation of state for pressure, that is the relationship between pressure p and the solution variables $\mathbf{u}$. To set initial and boundary conditions, it is necessary to determine the initial distribution $\mathbf{u_0}(\boldsymbol{x})$ and the boundary function $\mathbf{g}(s, t)$ depending on the coordinate s describing the boundary and time. These known functions are then assigned respectively in the domain and in the inflow boundary Γ_{in} as follows:

$$\begin{cases} \mathbf{u}(\boldsymbol{x}, 0) = \mathbf{u_0}(\boldsymbol{x}) \\ \mathbf{u}|_{\Gamma_{in}}(t) = \mathbf{g}(s, t) \qquad s \in \Gamma_{in}. \end{cases}$$

The inflow or inlet boundary Γ_{in} is defined as the subset of the boundary for which the inner product between the local unit normal and the advection velocity $\mathbf{a}(\mathbf{u}) = \mathrm{d}\mathbf{f}/\mathrm{d}\mathbf{u}$ is negative:

$$\Gamma_{in} = \{\boldsymbol{x} \in \Gamma : \boldsymbol{n}(\boldsymbol{x}, t) \cdot \mathbf{a}(\mathbf{u}(\boldsymbol{x}, t)) < 0\}\,. \tag{2.4}$$

The remaining part of the boundary will be referred to as the outflow or outlet boundary. It is worth noting that the definition of the inlet boundary depends on the solution $\mathbf{u}$ at a given time, thus the inflow boundary varies in general with time. Then, assuming that the flow is approximated by means of the *polytropic ideal gas* thermodynamic model (i.e. a gas with constant pressure and volume specific heats c_p and c_v), the resulting equation of state is the following

$$p = (\gamma - 1)E, \tag{2.5}$$

where

$$\gamma = \frac{c_p}{c_v} \qquad E = E^t - \frac{1}{2\rho}|\mathbf{m}|^2.$$

For air, the specific heats ratio γ is equal to 1.4. With Eqn. (2.5), the definition of the aerodynamic problem is complete.

However, the simulation of aileron buzz requires to perform unsteady simulations of the flowfield while the computational domain is continuously changing its shape to account for the control-surface motion. This is a typical feature of aeroelastic computations: the flow equations are to be solved in a domain whose shape continuously varies with time due to the motion of the boundaries of the domain, namely the deformation of the structure itself. Therefore, it is necessary that the model is capable of coping with the boundary motion, both in the definition of the appropriate mathematical model and in the numerical implementation. As far as the former is concerned, the appropriate model should resort on the Arbitrary Lagrangian Eulerian (ALE) formulation, which is aimed at combining the advantages of the classical kinematical descriptions (i.e. Lagrangian and Eulerian formulations), while minimizing respective drawbacks as far as possible. The ALE formulation of the Euler equations turns out to be similar to the Eulerian formulation Eqn. (2.3), except for an additional flux term that depends on the local velocity $\boldsymbol{v}$ of all the moving boundaries. In integral form, the Euler equations become

$$\frac{\mathrm{d}}{\mathrm{d}t}\int_{\Omega(t)} \mathbf{u}\, d\Omega + \oint_{\Gamma(t)} [\mathbf{f}(\mathbf{u}) - \mathbf{u}\boldsymbol{v}] \cdot \hat{\boldsymbol{n}}\, d\Gamma = 0, \tag{2.6}$$

where it is worth noting the time dependency of the moving domain $\Omega(t)$, boundary $\Gamma(t)$, normal vector $\hat{\boldsymbol{n}}(\boldsymbol{x}, t)$ and local velocities vector $\boldsymbol{v}(\boldsymbol{x}, t)$ [12]. Regarding the numerical techniques capable of dealing with moving boundaries, time integration scheme compliant with the Geometric Conservation Law (GCL) and mesh

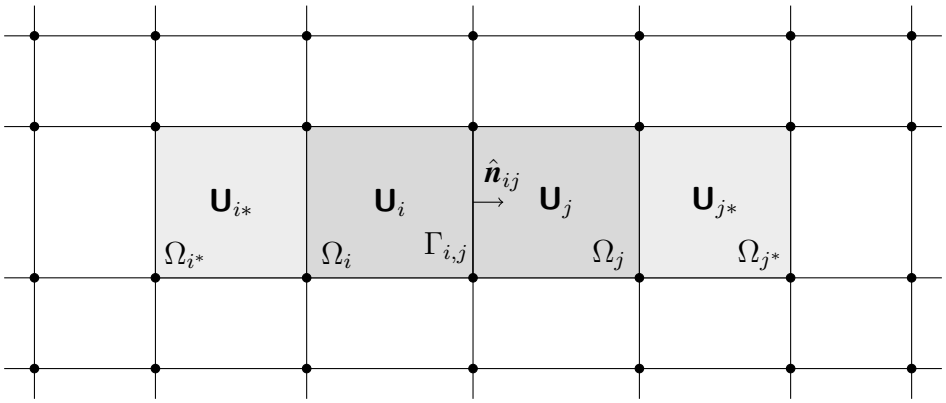

Figure 2.2: Spatial grid and volumes involved in flux function definition.

movement and adaptation strategies are employed. The former is discussed in the following section, that presents space and time discrtization of the equations, while the latter is presented in Section 2.2.

2.1.2 Space discretization

Once the set of governing equations are assembled, space discretization is carried out by subdiving the domain into a number of volumes or cells, as sketched in Fig. 2.2. Each cell Ω_i is associated with vector $\mathbf{U}_i$ which stores the conservative variables averaged on the volume and is defined at the cell-center node $\boldsymbol{x}_i$. In this way, the volume and surface integrals in Eqn. (2.3) are evaluated respectively on each cell volume and volume boundary. In particular, the volume integrals involves only the i-th cell, whereas the surface integral become a summation over the interfaces between the i-th cell and all the adjacent cells, thereby yielding a coupling between neighbouring volumes. Therefore, a connectivity with the neighbouring cells is defined which comprises the interface Γ_{ij} representing the contact surface between the i-th and j-th volumes and the normal vector $\hat{\boldsymbol{n}}_{ij}$ associated to the interface [13]. The resulting set of ordinary differential equations in time is the following:

$$\frac{\mathrm{d}\left(\mathbf{U}_i\Omega_i\right)}{\mathrm{d}t} + \sum_{i=1}^{N_f} |\Gamma_{ij}|\mathbf{F}_{ij} = 0 \quad \forall i, \tag{2.7}$$

where $\mathbf{F}_{ij}$ is the numerical evaluation of the flux function or *numerical flux* between i-th and j-th cells and N_f is the set of interfaces that bounds the i-th cells: $\Gamma_i = \left\{\Gamma_{i1}, \Gamma_{i2}, ..., \Gamma_{iN_f}\right\}$.

With regard to the numerical flux, the numerical scheme is defined with the purpose of obtaining a monotone but sharp solution near discontinuities, such as

shock waves, and at the same time to achieve high-order accuracy in space at least in smooth regions. A good and widely employed strategy [14] relies on a high resolution combination of a monotone first-order-accurate numerical flux vector, namely $\mathbf{F}^{\mathbf{I}}_{ij}(\mathbf{U}_i, \mathbf{U}_j)$, and a second-order-accurate flux vector $\mathbf{F}^{\mathbf{II}}_{ij}(\mathbf{U}_{i^*}, \mathbf{U}_i, \mathbf{U}_j, \mathbf{U}_{j^*})$. The former depends on the solution in the cells adjacent to the interface, where the flux is computed, whereas the latter also involves neighbouring volumes, as sketched in Fig. 2.2. In this sense, the algorithm uses the first-order-accurate method as a rule, but close to a discontinuity switches to the second-order-accurate flux. The swapping between the two flux vectors is obtained by means of a suitable flux-limiter operator $\Phi(\mathbf{U}_{i^*}, \mathbf{U}_i, \mathbf{U}_j, \mathbf{U}_{j^*})$, that is:

$$\mathbf{F}^{\mathbf{II}}_{ij} = \mathbf{F}^{\mathbf{I}}_{ij} + \Phi \left(\mathbf{F}^{\mathbf{II}}_{ij} - \mathbf{F}^{\mathbf{I}}_{ij} \right). \tag{2.8}$$

2.1.3 Time discretization

The solution of Eqn. (2.7) requires time discretization, which is carried out with the numerical schemes typical for the solution of a Cauchy problem. In fact, Equation. (2.7) can be rewritten as a Cauchy problem as follows

$$\begin{aligned} \frac{\mathrm{d}\left(\mathbf{U}_i \Omega_i\right)}{\mathrm{d}t} &= f(\Gamma_{ij}, \mathbf{U}_{i^*}, \mathbf{U}_i, \mathbf{U}_j, \mathbf{U}_{j^*}) \quad \forall i \\ &= f(t, \mathbf{U}_i, \Omega_i) \quad \forall i, \end{aligned} \tag{2.9}$$

together with suitable initial conditions. In the right-hand-side of the previous equation function f appears, that is a proper function in which all the space discretization is condensed. Depending on when such function is evaluated, different time-marching scheme are defined. Among time integration methods are *explicit* methods, which evaluate the right-hand-side of Eqn. (2.9) using information at previous time intervals. For instance, an explicit Runge-Kutta method, such as the one employed in the numerical implementation (discussed in the next section), looks like the following

$$\left(\mathbf{U}_i \Omega_i\right)^{n+1} = \sum_{k=0}^{p} a_k \left(\mathbf{U}_i \Omega_i\right)^{n-k} + \Delta t \sum_{k=0}^{p} b_k f_i^{n-k} \quad \forall i, \tag{2.10}$$

where apex $n+1$ stands for the time to be solved, apexes $n-k$ denote the evaluation at previous time intervals and Δt is the constant time step. Coefficients a_k, b_k and upper bounds of summations p, k depends on the particular Runge-Kutta method considered. Opposite to explicit methods, *implicit* schemes exist, which in addition to information at previous time instants involve information at the time instant to be solved, namely $\left(\mathbf{U}_i \Omega_i\right)^{n+1}$, f^{n+1}, etc. As a result, the methods belonging to the latter class imply higher computational cost, due to the

manipulation of high-order sparse matrices and possibly nonlinear systems [15]. Furthermore, it is necessary to garantee the stability of the numerical scheme. For a hyperbolic one-dimensional problem it is possible to prove that an implicit method is always unconditionally stable, whereas explicit methods require the time step Δt to satisfy the Courant Friedrich Lewy condition (CFL) for stability [16]. The CFL condition for the d-dimensional Euler equations states the following

$$\max_i \left(\Delta t \frac{|\Gamma_i|}{|\Omega_i|} \max_q \lambda_{iq} \right) \leq Co_{max} \tag{2.11}$$

that is the time step Δt should be bounded, depending on the size $|\Gamma_i|/|\Omega_i|$ of the smallest cell in the grid, the greatest advection velocity (computed as the maximum eigenvalue of the advection matrix $\mathbf{A} = \mathrm{d}\mathbf{F}/\mathrm{d}\mathbf{U}$, which is numerically evaluated on volume Ω_i). The bound is set by the maximum Courant number Co_{max}, depending on the numerical scheme [14].

In addition, the integration between time instants t^n and t^{n+1} in the case of moving boundary (thereby, moving grid) raises the question of when to evaluate the metric quantities (e.g. cell volumes Ω_i, interfaces Γ_{ij}) and the numerical fluxes. A useful guideline for evaluating these quantities as well as time-integrating fluxes on moving grids is provided by the enforcement of the Geometric Conservation Law (GCL) or its Discrete counterpart (DCGL). The GCL law states that the computation of the metric quantities depending on the grid points positions and velocities must be performed in such a way that, independently of the mesh motion, the resulting numerical scheme preserves the state of a constant and uniform flow. Thus the CGL can be interpreted as a relationship between the rate of change of the volume Ω and the velocity $\boldsymbol{v}$ of its moving boundary, that is

$$\frac{\mathrm{d}}{\mathrm{d}t} \int_{\Omega(t)} d\Omega = \oint_{\Gamma(t)} \boldsymbol{v} \cdot \hat{\boldsymbol{n}} \, d\Gamma, \tag{2.12}$$

which, after space and time discretization, results in a condition on the numerical form of the mesh velocity $\mathbf{v}_{ij}^n$ associated to the interface Γ_{ij}^n. For instance, in the case of the explicit Euler scheme, the following set of equations is obtained

$$\frac{\mathrm{d}}{\mathrm{d}t} \int_{\Omega(t)} d\Omega = \sum_{i=1}^{N_f} |\Gamma_{ij}| \mathbf{v}_{ij}^n \qquad \forall i, \tag{2.13}$$

that yield the definition of the GCL-compliant interface velocity

$$\mathbf{v}_{ij}^n = \frac{\Omega_i^{n+1} - \Omega_i^n}{\Delta t |\Gamma_{ij}|} \qquad \forall i, j. \tag{2.14}$$

The previous result is valid for the explicit Euler scheme, but a similar procedure is possible for arbitrary time integration schemes.

2.2 Numerical Implementation

First of all, for the numerical CFD and CFD-based aeroelastic computations the solver AeroFoam is used, whose development started back in 2008 and continues today with the challenging target of filling the empty space left in OpenFOAM for a density-based RANS solver, almost mandatory when dealing with highly compressible flows [17]. In this sense it provides all the space and time discretization operators typical of explicit density-based algorithms, as well as offering a variety of speed-up techniques, several flow models and interfaces for aeroelastic applications.

In the following, some of the most important numerical ingredients employed in the calculations are discussed and presented from the pre-processing to the post-processing stage.

Mesh. To start with, the domain is set, using a coordinate system such that the plane to which the wing section belongs is the xz-plane and that positive deflection and hinge moment, corresponding to rotation and moment about the y-axis, are oriented downwards (see Fig. 2.1 at the beginning of the chapter). Then, the

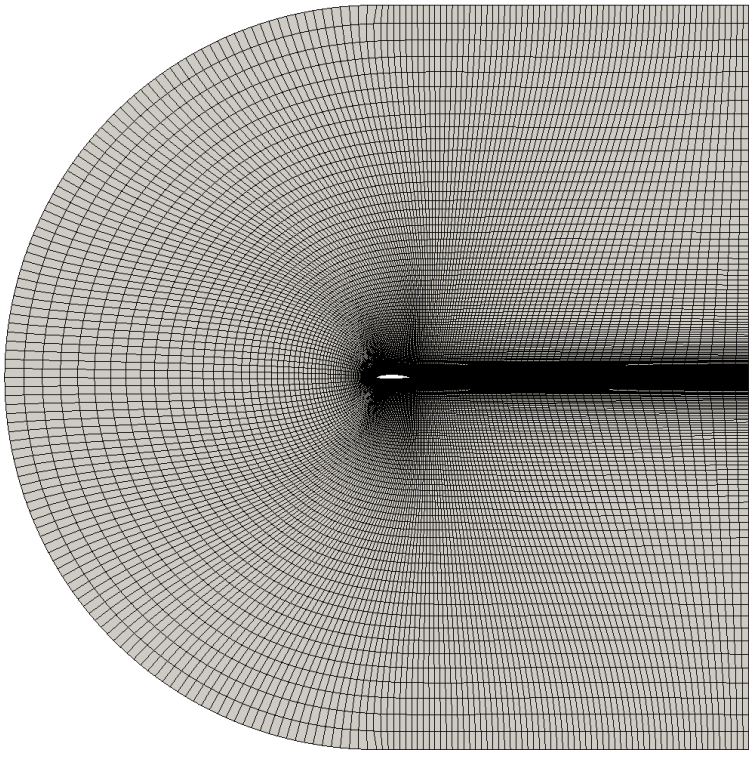

Figure 2.3: Aerodynamic C-mesh.

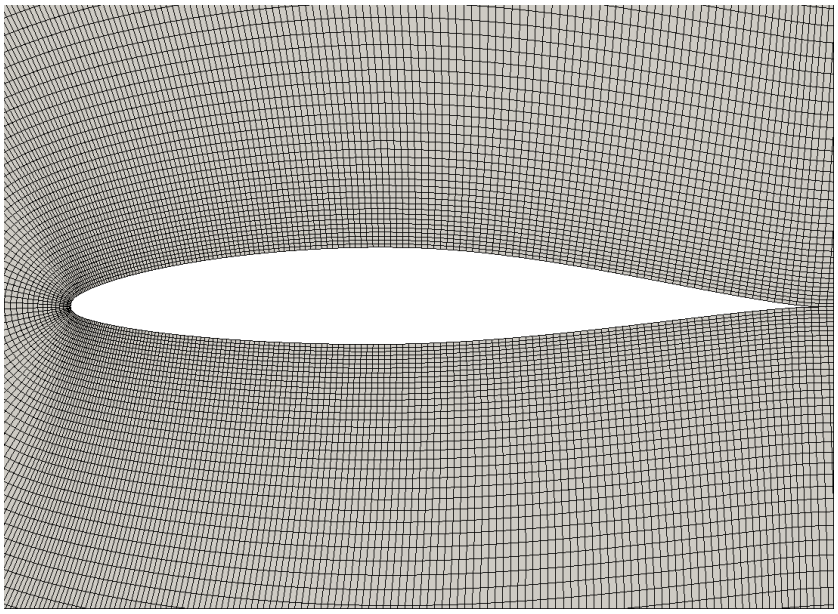

(a) Uniform grid

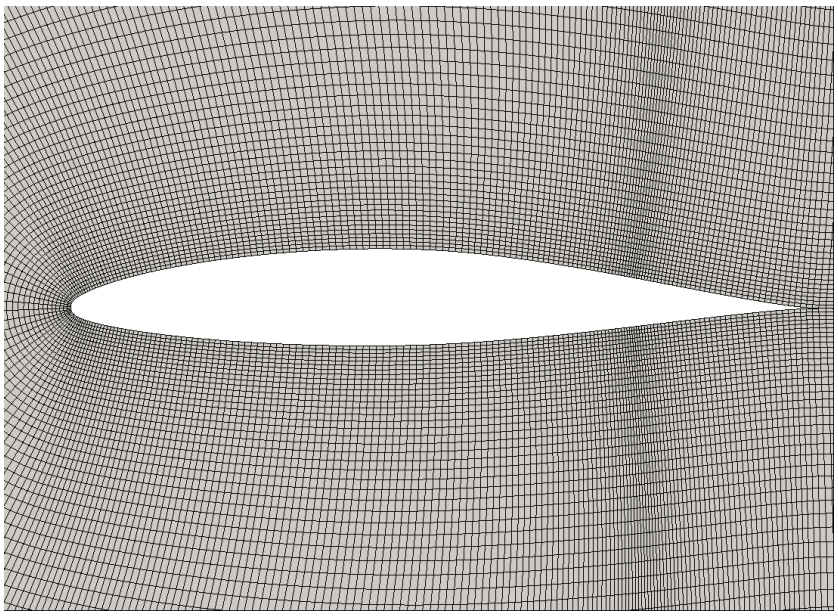

(b) Refined grid

Figure 2.4: Uniform and hinge-refined grids.

aerodynamic grid is built with a routine written in Matlab environment. It is a C-mesh built around the wing section with hexaedral elements, which extends ± 10 chords both chordwise and in the airfoil thickness direction Fig. 2.3. The extension of the mesh has been selected after a brief convergence analysis, which is

presented in Section 4.2. Because the problem is two-dimensional, the discretization is carried out only in the wing section plane, whereas spanwise the elements are not partitioned. In addition, the mesh is smoothly refined not only in radial sense from the far-field boundary to the body, but also from the trailing edge to the leading edge, in order to describe in detail the nose geometry. This type of mesh will be referred to as Uniform, so that it is distinct from a further refined grid (called Refined), that is smoothly refined at the aileron hinge line in addition to the radial and leading-edge refinements (see Fig. 2.4). This second type of mesh has been generated to accurately capture the shock waves moving about the hinge line and it provides better convergence property as discussed later in Section 4.2. Actually, other grids are employed in the analysis, however, because they arise from the choice of the aeroelastic interface, i.e. the integration between the aerodynamic and structural sub-systems, they are discussed in the next chapter (see Section 3.3).

Boundary conditions and initial conditions. After the generation of the grid, a routine converts the mesh into OpenFOAM native format; this operation is necessary, because the CFD solver chosen for the analysis is developed in OpenFOAM environment. The conversion also produces the partition of all the boundary into patches, namely parts of the boundary with different characteristics. On each patch a boundary condition must be set by the user; the boundary condition is a *no-penetration* condition for the patch to whom the wing belong, an *empty* condition for the patches perpendicular to the y-axis, and the *automatic* condition for the inlet and outlet boundary. The *automatic* condition ensures that at each time the inlet boundary is computed according to the condition expressed in Eqn. (2.4) and that the inflow boundary condition is applied only on the cells belonging to the inlet patch. In addition, the wing patch is automatically detected by the solver as a moving boundary and this information is crucial to the solver that considers and applies displacement only to moving boundaries. Regarding initial conditions, those are assigned by the user inside an appropriate folder contained in the *case folder*, i.e. the folder where all the data about the calculation are stored. The initial conditions are set in terms of field of pressure, temperature, velocity and possibly density, momentum and total energy, if the Euler equations are solved starting from a previous computation.

Space discretization. In order to apply the space discretization presented in Section 2.1.2, the first order accurate Approximate Riemann Solver by Roe $\mathbf{F}^{\mathbf{ROE}}$ and the second order accurate Lax-Wendroff $\mathbf{F}^{\mathbf{LW}}$ numerical fluxes are implemented in the solver, thus: $\mathbf{F}^{\mathbf{I}} = \mathbf{F}^{\mathbf{ROE}}$ and $\mathbf{F}^{\mathbf{II}} = \mathbf{F}^{\mathbf{LW}}$. The switch between them is automatically controlled exploiting the flux limiting strategy by van Leer [14], which, based on Eqn. (2.8), requires the numerical solution on the extended neigh-

bouring cells $\mathbf{U}_{i^*}$ and $\mathbf{U}_{j^*}$ to be readily available (for details about the notation of the cells, please refer to Fig. 2.2). This operation is performed efficiently with a suitable connectivity data structure built in the pre-processing stage. In addition, a GCL compliant ALE contribution to the numerical fluxes is automatically added in order to cope with moving boundaries.

Time discretization. With regard to time discretization schemes, the multi-stage explicit Runge-Kutta methods are implemented as the best compromise between computational requirements, stability condition and accuracy. Moreover, several acceleration options are available. In particular, for the present analysis a five-stage explicit Runge-Kutta time integration strategy was chosen together with a Multi-Grid method to accelerate convergence. In addition, a Local Time-Stepping technique was employed to speed-up convergence to the initial steady conditions, from which accurate unsteady solutions are obtained using an implicit Dual Time Stepping technique with explicit sub-iterations [18].

Mesh deformation tools. In addition, when dealing with problems in which the boundary and the grid vary with time, it is necessary to resort on mesh movement and adaptation techniques. A dedicated mesh deformation tool available in AeroFoam, which is based on a modified version of the Inverse Distance Weighting interpolation kernel[19] and it is particularly suited for aeroelastic static and dynamic simulation of free flying aircraft.

Post-process. The post-processing stage is carried out with the software Paraview and also with post-processing routines written on purpose in Octave and Python languages.

Finally, parallel computations have also been performed, because the solver has proved a satisfactory parallel efficiency with a linear speedup factor, benchmarked up to 128 processors [20].

Chapter 3

Aeroelastic Model

The preceding chapter was concerned with the aerodynamic CFD model, whose numerical solution provides the pressure field around the wing section and thereby the time-varying aerodynamic moment acting on the aileron. In this chapter, the attention is drawn on the entire dynamic aeroelastic system, which comprises, in addition to the aerodynamic model, the structural model. In general, aeroelastic problems are subdivided into problems where the interaction with the aerodynamics involves both inertial and elastic forces and phenomena where the interaction between the aerodynamics and the structure involves only the airplane flexibility. The former problem are usually referred to as *static* aeroelastic phenomena, while the latter are labelled as *dynamic* aeroelastic problems [21]. In this sense aileron buzz is numbered among the dynamic phenomena, because the inertial term has a significant contribution to the equations of motion. Elastic and dissipative contribution of the structure may be disregarded for control-surface buzz, because their effect would not be essential; as a matter of fact, the dynamic model of the aerodynamics already provides damping and stiffness to the overall aeroelastic system and, indeed, it is the value of such aerodynamic elastic and dissipative contributions that tunes the energy exchange between the aerodynamic and structural sub-systems, yielding stability or instability.

In the first section of this chapter the complete aeroelastic model for aileron buzz is presented and outlined with a comparison based on control theory. The subsequent sections are devoted to the definition of the structural part of the dynamic model and the discussion of the coupling between aerodynamics and structural dynamics. Finally, the numerical technique for the direct simulation of aileron buzz is presented.

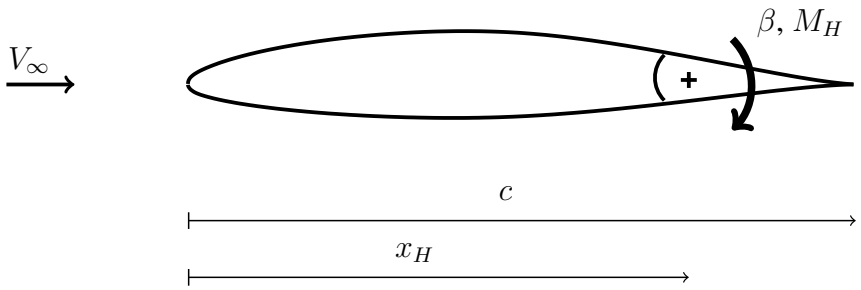

Figure 3.1: Dynamic model.

3.1 Aeroelastic system

As already mentioned in the previous chapter, for the analysis of aileron buzz a two-dimensional wing section is used. This choice is supported by the extensive use of two-dimensional models both in numerical simulations and in wind-tunnel tests [2, 22] and by the argument that two-dimensional models are reasonable for conservative estimates [6]. Another reason driving this choice is the evidence that the phenomenon is dominated by one degree of freedom, which belongs to the two-dimensional plane of the wing section. The last reasoning also results in the penchant for structural models of the aileron that are rigid, rather than flexible ones. Accordingly, in the current work the dynamic model is represented by a fixed wing section with unit span and non-symmetrical airfoil, in which the aileron is integrated into the wing. The aileron is hinged at three-quarter-chord location and its degree-of-freedom, namely rotation about the hinge β, is modeled as rigid. The layout of the problem is sketched in Fig 3.1.

Besides, the main feature of the aeroelastic problem is highlighted by the analogy with control teory presented in the block diagram sketched in Fig. 3.2. The system comprises the structural block I, which stands for the dynamic motion of the freely hinged rigid control-surface, and the aerodynamic block A. Letter I is chosen to denote the structural sub-system, because the dynamics of the aileron involves only the structural inertial term, while elastic and dissipative contributions are disregarded. The inertial force depending on the aileron deflection β needs to balance the aerodynamic moment M_H acting on the control-surface; the balance is provided by the motion of the aileron itself. In turn, the aileron rotation influences the aerodynamics involved in the problem to the extent that the boundary conditions of the aerodynamic equations are changed. As a result, a different pressure field is obtained, thereby modifying the aerodynamic moment acting on the aileron itself, which changes the deflection and so on. Therefore, the aeroelastic problem resembles a closed-loop system, in which the structural sub-system acts like the main system and the aerodynamic sub-system provides the feedback.

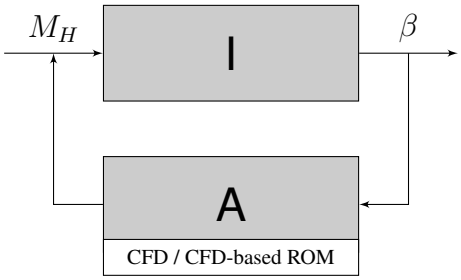

Figure 3.2: Block diagram of the aeroelastic system for buzz analysis.

Hence the CFD computation is conceptually comparable to a dynamic system that translates the structural displacement into the aerodynamic load. However, its solution is time- and work-consuming and the faster structural solver is basically left waiting for the CFD solution at each time step. As a result, the direct aeroelastic simulation with the CFD aerodynamic model is very expensive, especially when the solution for different configurations is demanded. A very attractive possibility is to resort on a Reduced-Order Model (ROM), namely a surrogate model of the aerodynamic sub-system, which is based on fewer degrees of freedom and necessitates less computational effort in order to be solved. In addition, the ROM should be capable of accurately representing the actual dynamic system, mapping the structural displacement into the aerodynamic loads as the CFD solver would do. A methodology for the construction of a suitable ROM is *system identification*, which in this case is carried out starting from the CFD solutions, thereby yielding the so-called *CFD-based ROM*.

In conclusion, the modelling of the aerodynamics is carried out in two ways: by means of a CFD solution and with a surrogate low-order model. A more complete discussion on the CFD-based ROM is given in Chapter 5, where the methods for system identification and the definition of the ROM for buzz is presented. Instead, the following sections focus on the definition of the structural sub-system and the discussion of the CFD-based aeroelastic model for the aeroelastic direct simulation.

3.2 Structural model

The structural model is represented by a rigid aileron integrated into the two-dimensional airfoil. The aileron motion is described with a single degree of freedom, namely the aileron deflection angle about its hinge $\beta(t)$, whose dynamics is governed by the following equation

$$I_H \ddot{\beta}(t) = M_H(t), \tag{3.1}$$

where I_H is the aileron moment of inertia and $M_H(t)$ is the aerodynamic moment acting on the aileron, both evaluated with respect to the hinge line. Equation (3.1) states the balance between inertial and aerodynamic forces, whereas structural elastic and dissipative contributions are not modeled in the present work.

Because a non-symmetrical airfoil is chosen for the analysis, the initial condition for Eqn. (3.1) is a perturbation provided by the initial steady unbalanced aerodynamic moment acting on the aileron.

3.3 Numerical models and aeroelastic interface

The structural model can be easily defined in the solver, which is also responsible of performing the feedback connection between the structural and aerodynamic problems. In particular, two structural models have been employed and thereby two ways to interface aerodynamics and structure dynamics.

The first model exploits the fact that the problem is governed by one rigid degree of freedom: at each time interval, after the calculation of the updated control-surface deflection β^{n+1}, the boundary cells belonging to the aileron are displaced according to a rigid linearized rotation $\mathcal{R}$, that is

$$\boldsymbol{u}_a^{\,n+1} = \mathcal{R}\boldsymbol{u}_a^{\,n}$$

where vectors $\boldsymbol{u}_a^{\,n+1}$ and $\boldsymbol{u}_a^{\,n}$ represent the boundary volumes displacements respectively at the updated and current time. The rotation operator $\mathcal{R}_i$, which depends on the value of the control-surface deflection β^{n+1} and the position of the i-th aerodynamic cell $\boldsymbol{x}_{a_i}^{\,n} = \left\{x_{a_i}^{\,n}, y_{a_i}^{\,n}, z_{a_i}^{\,n}\right\}^T$, acts on each aerodynamic cell as follows

$$\mathcal{R}_i(\beta^{n+1}, \boldsymbol{x}_{a_i}^{\,n}) = \begin{bmatrix} 0 & 0 & 0 \\ 0 & 0 & 0 \\ \beta^{n+1} & 0 & 0 \end{bmatrix} \left(\begin{Bmatrix} x_{a_i}^{\,n} \\ y_{a_i}^{\,n} \\ z_{a_i}^{\,n} \end{Bmatrix} - \begin{Bmatrix} x_H \\ y_H \\ z_H \end{Bmatrix} \right)$$

and in a compact form the operator $\mathcal{R}$ reads

$$\mathcal{R}(\beta^{n+1}, \boldsymbol{x}_a^{\,n}) = \left[\, \hat{\boldsymbol{y}} \times \left(\boldsymbol{x}_{a_i}^{\,n} - \boldsymbol{x}_H\right) \,\right]^T \beta^{n+1},$$

where $\boldsymbol{x}_H = \{x_H, y_H, z_H\}^T$ is the position of the hinge (i.e. the center of rotation) and $\hat{\boldsymbol{y}}$ is the unit vector denoting the y-axis. The linearized rotation needs to be applied only to the cells belonging to the aileron boundary. In order to do so, a slight modification in AeroFoam is introduced: in the pre-processing stage a box $\mathcal{B}$ is defined in such a way that all the nodes of a moving boundary falling inside the box are actually moved during the computations, whereas the remaining nodes are held still:

$$\boldsymbol{x}_a^{\,n+1} = \begin{cases} \boldsymbol{x}_a^{\,n} + \boldsymbol{u}_a^{\,n+1} & \text{if } \boldsymbol{x}_a^{\,n} \in \mathcal{B} \\ \boldsymbol{x}_a^{\,n} & \text{if } \boldsymbol{x}_a^{\,n} \notin \mathcal{B} \end{cases}$$

For the current work the box is the set: $\mathcal{B} = (x_H, c) \times (0, 1) \times (-1, 1)$. A consequence of this approach is that an edge is produced between the airfoil and the aileron when the control-surface is deflected, because the rigid rotation is applied only to the cells of the boundary behind the hinge line.

The second approach requires the definition of a modal basis $\mathcal{N}$, depending on the structural nodes position $\boldsymbol{x}_s$, that associates the generalized displacement $q(t)$, i.e. the aileron deflection angle, to the linearized displacement of the structural nodes $\boldsymbol{u}_s$. After the computation of the updated generalized displacement q^{n+1}, the modal basis updates the structural nodes $\boldsymbol{u}_s^{\,n+1}$ as follows

$$\boldsymbol{u}_s^{\,n+1} = \mathcal{N} q^{n+1}.$$

The structural nodes are located on the airfoil chord line and are connected by rigid elements, while the modal basis is defined in such a way that it provides displacements consistent with those of the rigid model. In particular, the basis depends on the location of the nodes $\boldsymbol{x}_s$ and it has null value for the nodes placed ahead of the hinge line, while for the N_{sA} nodes belonging to the aileron it is linearly dependent on the difference between the x-coordinate of the structural node $\boldsymbol{x}_{s_i}$ and that of the hinge line x_H:

$$\mathcal{N}(\boldsymbol{x}_s^n) = \begin{bmatrix} 0 & 0 & 0 \\ \vdots & \vdots & \vdots \\ 0 & 0 & 0 \\ x_{s_1}^{\,n} - x_H & 0 & 0 \\ & \vdots & \\ x_{s_i}^{\,n} - x_H & & \\ \vdots & \vdots & \vdots \\ x_{s_{N_{sA}}}^{\,n} - x_H & & \end{bmatrix}$$

or in a compact format

$$\mathcal{N}(\boldsymbol{x}_s^n) = \left[\left[\boldsymbol{0} \dots \boldsymbol{0} \right], \left[\hat{\boldsymbol{y}} \times (\boldsymbol{x}_s^{\,n} - \boldsymbol{x}_H) \right] \right]^T.$$

The modal basis has three columns and as many rows as the structural nodes. Once the structural nodes have been displaced, it is necessary to translate the structural displacement and velocity fields into a variation of the boundary displacements (i.e., boundary conditions) of the aerodynamic sub-system. The employment of the aeroelastic interface operator $\mathcal{I}$ provides the conversion. In general, it is necessary to

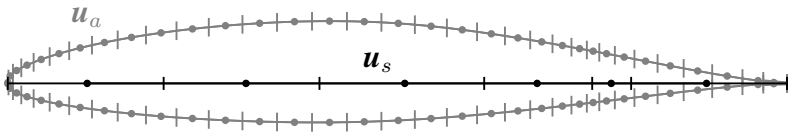

Figure 3.3: Structural nodes $\boldsymbol{u}_s$ and aerodynamic nodes $\boldsymbol{u}_a$.

1. translate the structural displacement and velocity fields into a variation of the boundary conditions on the aerodynamic sub-system

$$\boldsymbol{u}_a = \mathcal{I}(\boldsymbol{x})\, \boldsymbol{u}_s; \tag{3.2}$$

2. convert the pressure field providing the aerodynamic forces into a load condition acting on the structural sub-system

$$\boldsymbol{F}_s = \hat{\mathcal{I}}(\boldsymbol{x})\, \boldsymbol{u}_s. \tag{3.3}$$

The interface operator must meet several requirements. It should be capable of linking models with non-matching spatial domain and numerical grids, as well as preserve the momentum and energy exchanged between the two sub-systems. With regard to the latter feature, the conservation of momentum and energy is necessary to mantain the overall stability properties of the aeroelastic system, namely to garantee the equivalence of the virtual work $\delta\mathcal{L}$ made by the aerodynamic forces $\boldsymbol{F}_a$ on the structural displacements interpolated on the aerodynamic degrees of freedom $\boldsymbol{u}_a$ with the virtual work made by the aerodynamic forces interpolated on the structural degrees of freedom for the structural displacements:

$$\delta\mathcal{L} = \delta \left\{\boldsymbol{u}_a\right\}^T \left\{\boldsymbol{F}_a\right\} = \delta \left\{\boldsymbol{u}_s\right\}^T \left\{\boldsymbol{F}_s\right\}. \tag{3.4}$$

The previous equation also provides a condition to define the interface operator between structural and aerodynamic forces, i.e. $\hat{\mathcal{I}}$; in fact, substituting Eqn. (3.2) into Eqn. (3.4) and comparing the result with Eqn. (3.3) yields

$$\hat{\mathcal{I}} = \mathcal{I}^T. \tag{3.5}$$

The strategy adopted in the solver AeroFoam to build the aeroelastic interface operator consists of an interpolation scheme based on a Moving Least Squares technique [23]. This method ensures the conservation of momentum and energy transfer between the two sub-systems and it is sufficiently flexible to treat complex configurations. However, in this case the interface operator is employed only

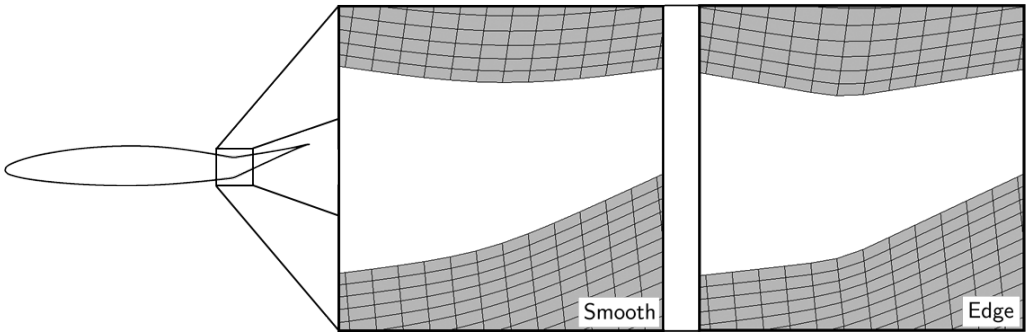

Figure 3.4: Example of Smooth and Edge grids with aileron deflection $\beta = 20$ deg.

in the conversion of the structural displacements into the aerodynamic displacements. The reason for this is that during the analysis it has become evident that, although the operator $\mathcal{I}$ is globally conservative, the interface isn't partially conservative. In other words, the total aerodynamic forces acting on the airfoil computed on the structural nodes matches with the load computed on the aerodynamic nodes, however the partial load on the aileron is different when it is computed in the structural set with respect to the one of the aerodynamic set. As a matter of fact, the coupling between the aerodynamic and structural nodes is carried out on every moving boundary, which in this case is simply the wing boundary. Because the wing boundary is a single non-partitioned patch, this implies that the aerodynamic forces belonging to the aileron aerodynamic nodes partially transfer also to the structural nodes ahead of the hinge line. As a result, the load acting on the aileron is different for the structural set and the aerodynamic set. Because the study of aileron buzz with a rigid degree of freedom doesn't strictly require the presence of a modal aeroelastic interface, the interface does not need to be redefined and the problem is bypassed employing the aeroelastic interface operator only to translate the structural displacements to the aerodynamic nodes and it is not involved in the conversion of the aerodynamic forces. For the latter purpose, the aerodynamic load acting on the aileron is computed by summing up all the contributions of the forces associated to the aerodynamic nodes which lay inside a box $\mathcal{B}$, which defines the region in which the aileron is present. As already mentioned for the rigid interface previously discussed, the box is the set: $\mathcal{B} = (x_H, c) \times (0, 1) \times (-1, 1)$. In addition, the employment of the interface operator for the conversion of the displacement fields has an evident consequence: the translation softens the difference between the null displacements of the structural nodes ahead of the hinge line and the displacements of the nodes belonging to the aileron, yielding a smoothed geometry.

As a result, two different grids have been created: the non-smoothed grid obtained with the rigid approach is labeled as Edge and the smoothed grid resulting

from the modal approach is referred to as Smooth (Fig. 3.4). The emerging difference between the two approaches is discussed in the next chapter. Once the boundary displacement is updated, either with the rigid or modal interface, the inner cells are moved with the dedicated hierarchical mesh deformation tool available in AeroFoam, based on a modified version of the Inverse Distance Weighting interpolation kernel, already mentioned in Section 2.2.

Finally, although the resulting grids are different, it is worth noting that both structural models are associated to the same numerical solver of the aeroelastic problem, which is the concern of the next section.

3.3.1 Numerical direct simulation

The numerical direct simulation is based on a pseudo-explicit scheme exploiting the dual time step technique. Aeroelasticity and fluid-structure coupling computations are usually performed using a very small global time step value. This is especially true when studying high frequency phenomena. Therefore a very large number of iterations is required, and this leads to very expensive computations. Moreover, moving meshes computations are required, which increases CPU costs. This is the reason why the use of dual time stepping for aeroelastic computations becomes very interesting. The physical time step used to describe the unsteady phenomenon is no longer constrained by stability time step values in the smallest cells. As a matter of fact, in dual time stepping the fluid equation of motion is integrated by regular time-marching, with the instantaneous flowfield at each physical time step being computed via an inner iteration loop. The inner-loop "pseudo-time" process is similar to a steady-state flow computation, including the use of multigrid for convergence acceleration. In such a procedure, the inner loop also provides the weak coupling point for the structural solver. The structural equation of motion are based on a Crank-Nicolson scheme in which the aerodynamic loads are computed leveraging on the dual time stepping solution. A finer solution would involve the employment of a predictor-corrector approach, however when dealing with time steps much lower than the reciprocal of the maximum frequency of interest, an explicit solution is sufficiently accurate and does not induce instability problems.

Chapter 4

Numerical tests and results

The discussion in Chapter 1 highlights the role of shock dynamics in non-classical aileron buzz, which yields the employment of high-fidelity CFD codes that are capable of giving accurate prediction of the aerodynamic nonlinearities. However, further care must be taken on the definition of all minimal details that might influence the solution in terms of shock position and dynamics. In this sense, the current chapter is aimed at discussing some preliminary numerical results, pointing out the effects of grid details on buzz analysis. The reliability of the methods and techniques involved in the solver is not assessed in the current work, because an extensive analysis regarding the topic has already been accomplished in [24, 20] and proved the capability of the solver to deal with a wide range of aerodynamic and aeroelastic problems.

In the first section, the data of the dynamic model are summarized and a convergence analysis with respect to grid refinement and size is presented. The analysis stresses the importance of mesh convergence for reliable buzz computations. Then, in Section 4.3 the choice of the geometric aerodynamic model is discussed, which is devoted to the quantification of the uncertainty on buzz responses associated to a particular geometric detail, namely the hinge of the aileron.

4.1 Preliminary results

Calculations are performed on the non-symmetrical Naca 65_1-213 ($a = 0.5$) airfoil (Fig. 4.1), with the aileron pitching about three-quarter-chord location. The choice of this Naca airfoil is motivated by the availability of the data necessary for buzz simulation, as well as by historical reasoning. As a matter of fact, the Naca 65_1-213 was the airfoil shaping the wing mounted on the P-80, the first aircraft to encountered control-surface buzz according to Lambourne [3]. Exploiting data from Ref. [8] (airfoil chord $c = 1.472$ m, aileron moment of inertia $I_H = 0.5536$ kg·m^2), the Reynolds number is set to $1{\cdot}10^7$ and the angle of attack is set to zero

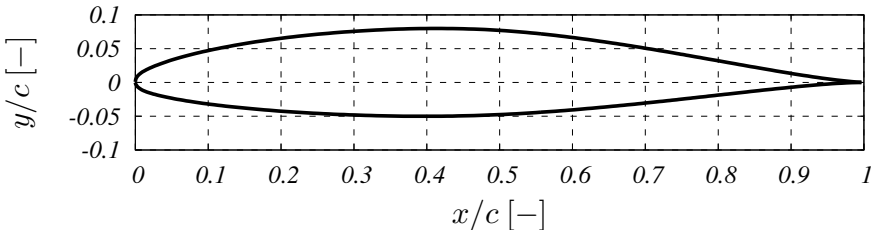

Figure 4.1: Naca 65_1-213 ($a = 0.5$) airfoil.

for the entire analysis. A time step of 0.001 is chosen in order to provide time accuracy in the frequency range of interest.

The C-mesh extends ± 10 chords both chordwise and in the airfoil thickness direction: this value is chosen after a comparison between two grids extending respectively ± 10 and ± 20 chords. The resulting behaviours of the pressure coefficient at Mach number $M = 0.8$ are presented in Fig. 4.2. The curves pratically overlap and there is not a sensitive distinction. The comparison drives the decision of employing the smaller grid, which demands less computational effort with equal characteristic size of the cells.

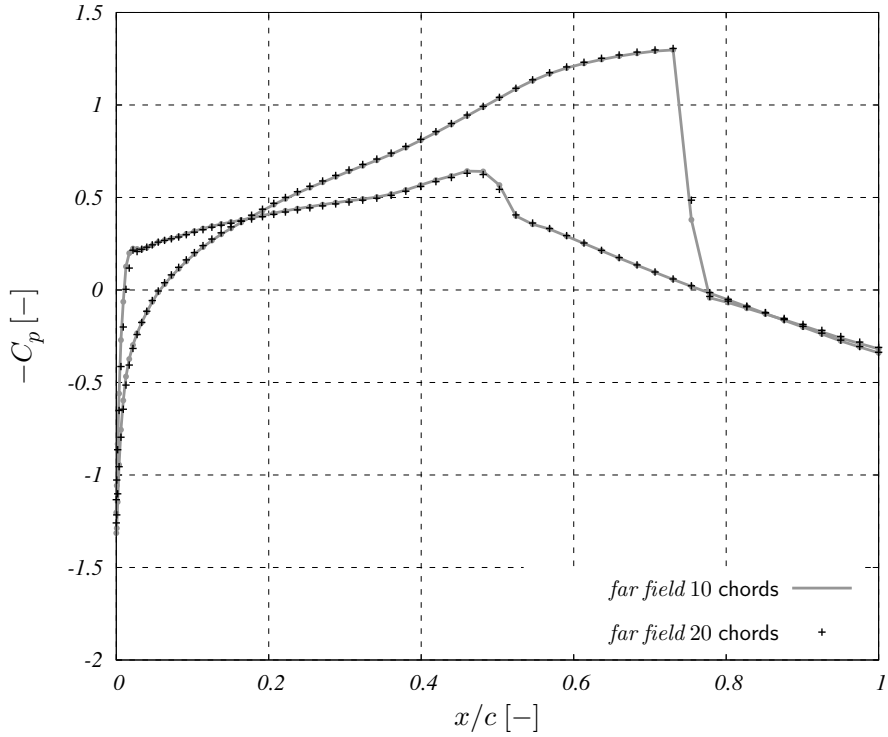

Figure 4.2: Pressure coefficient comparison between two grids extending respectively ± 10 chords and ± 20 chords.

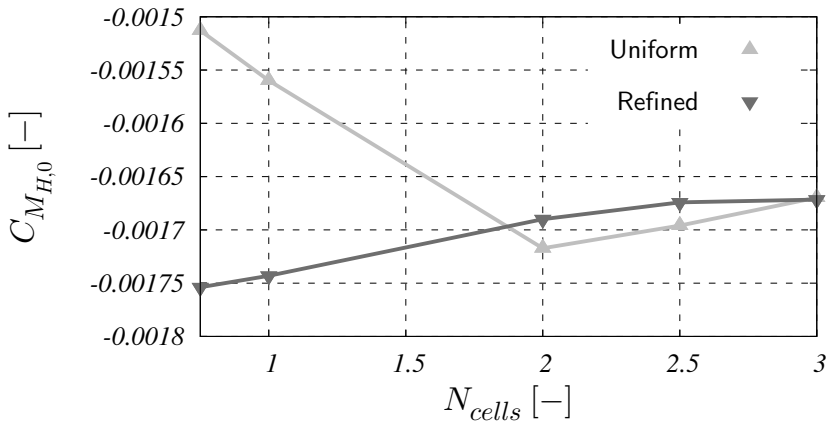

Figure 4.3: Mesh convergence with regard to initial hinge moment coefficient at $M = 0.8$.

4.2 Convergence analysis

To start with a convergence analysis regarding mesh refinement and size is performed at Mach number $M = 0.8$. A comparison is carried out among the initial aerodynamic hinge moment coefficients obtained progressively increasing the number of cells on the airfoil surfaces. The outcome of such analysis is presented in Fig. 4.3, where the hinge moment coefficients are plotted against the ratio N_{cells} between the number of cells belonging to the wing section and a reference value, corresponding to 128 cells. The Refined grid presents good convergence property with increasing number of cells on the aileron surfaces, whereas the Uniform grid yields a non-monotonic behaviour. With further increase in number of cells, it would probably oscillate around the value at which the Refined grid has converged and it would eventually converge, yet at a higher computational cost. The poor convergence property of the Uniform grid is likely to be the consequence of the lower resolution provided across the dominant shock wave, which is the shock wave occurring on the upper surface right behind the hinge line. Thus, from this preliminary analysis the Refined grid is selected for the aeroelastic computations.

Secondly, the system response is computed for different mesh sizes using both Edge grid and Smooth grid. The results are presented in Fig. 4.4, where on the left side the aileron deflection angle is plotted against time t and on the opposite side the behaviour of the aerodynamic hinge moment coefficient M_H in time is shown. The features of the behaviours at different mesh size are summarized in Fig. 4.5, where the resulting motion frequency f_{at} and amplitude A_{at} after transient interval are shown against the ratio N_{cells}. It is clear that the mesh size greatly influences the system response: a coarse mesh predicts buzz at Mach number $M = 0.8$,

whereas finer meshes yield stable responses. Furthermore, the Edge grid appears to be more sensitive to change in mesh size and it requires a finer mesh to converge to the stable behaviour. On the other hand, although it looks like the Smooth grid converges earlier to the stable behaviour, from a quantitative standpoint it converges only for the grid characterised by $N_{cells} = 3$, because for coarser grids the equilibrium deflection angle is still changing noticeably with mesh size. As a result, in both cases it is necessary to resort on the hinge-refined mesh with greater number of cells, containing 49152 hexaedra.

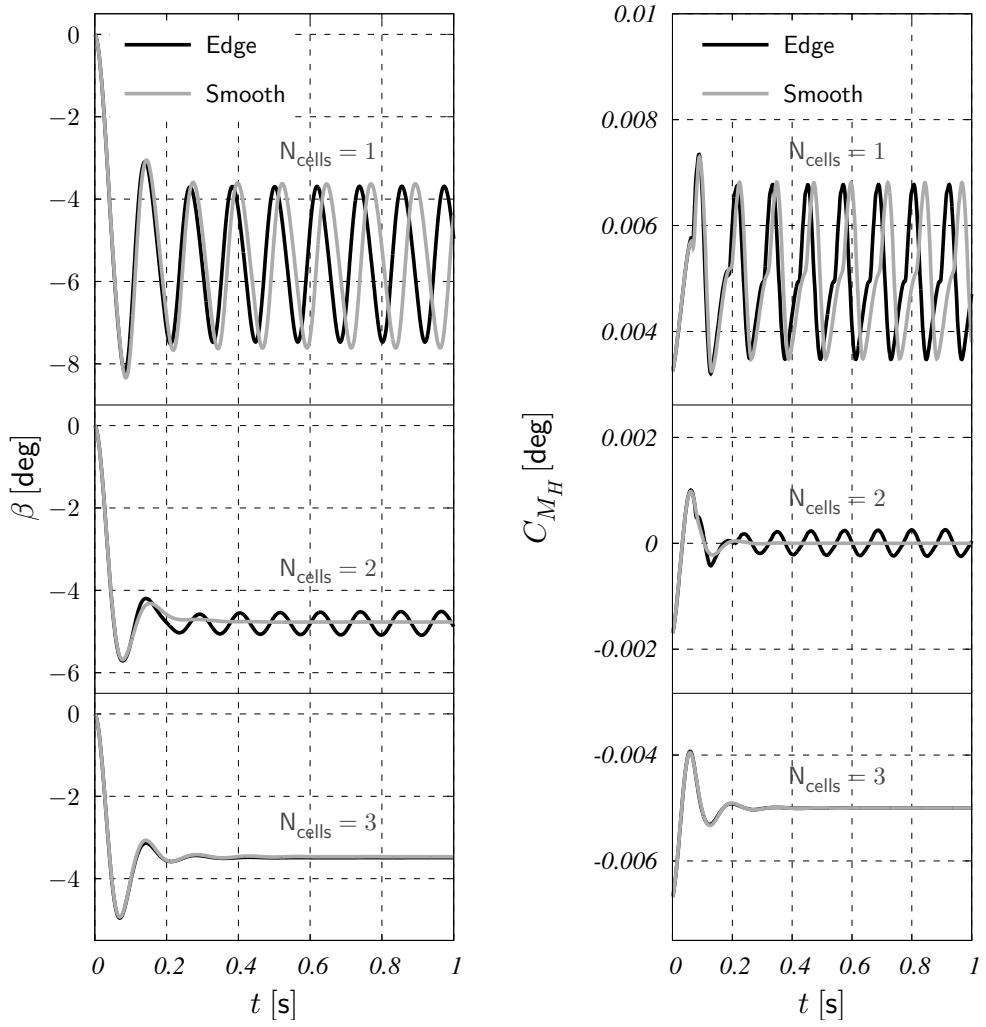

(a) Rotation (b) Moment

Figure 4.4: Comparison of system responses obtained with different mesh size at $M = 0.8$.

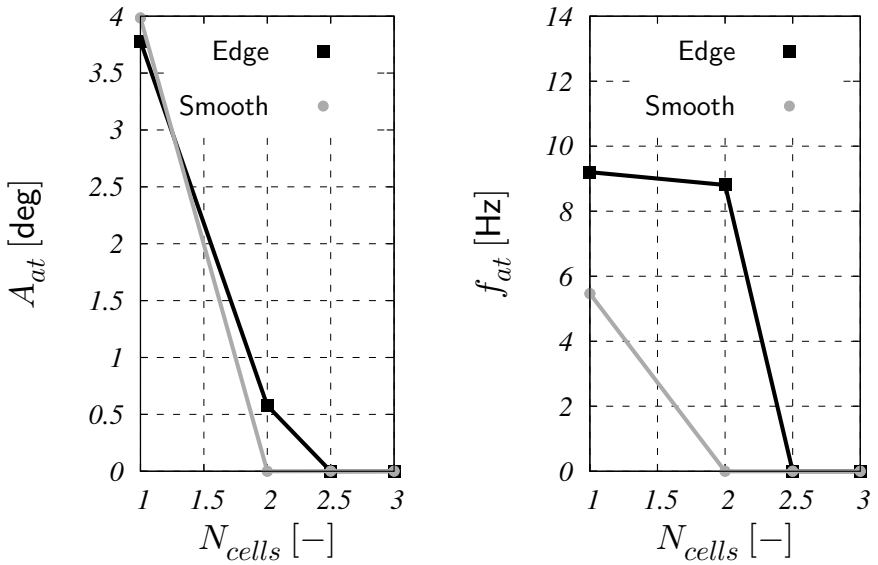

(a) Amplitude

(b) Frequency

Figure 4.5: Mesh convergence of aileron motion at $M = 0.8$.

4.3 Geometry Analysis

Given the role of shock dynamics in non-classical aileron buzz (cf. Chapter 1), a proper numerical study requires an accurate prediction of the aerodynamic non-linearities, which is obtained through the employment of CFD codes. However, other minimal details might influence singificantly the solution in terms of shock position and dynamics. Among them are mesh refinement and size, as discussed in the previous section. In the current section, the attention is turned to the integration of the control-surface in the main wing, which is usually carried out in two different ways when the gap is not modeled: one can either smooth the edge between the main body and the deflected control-surface or leave the shape discontinuity as it is. Both solutions have been employed in the past computations of aileron buzz and flutter with oscillating control-surfaces [25, 7, 26] and it is interesting to quantify the relevance of the geometric description of the hinge detail on the phenomenon.

Once the mesh size and refinement has been chosen based on the mesh convergence analysis, the aeroelastic responses at several Mach numbers are computed. The resulting variation in time of the aileron deflection angle is presented in Fig. 4.6, whereas Fig. 4.7 shows the shock waves position, which is computed as an average of the x-coordinate of the cells falling inside the shock front. It is evident that the Edge and Smooth grids yield dynamic responses that differ from

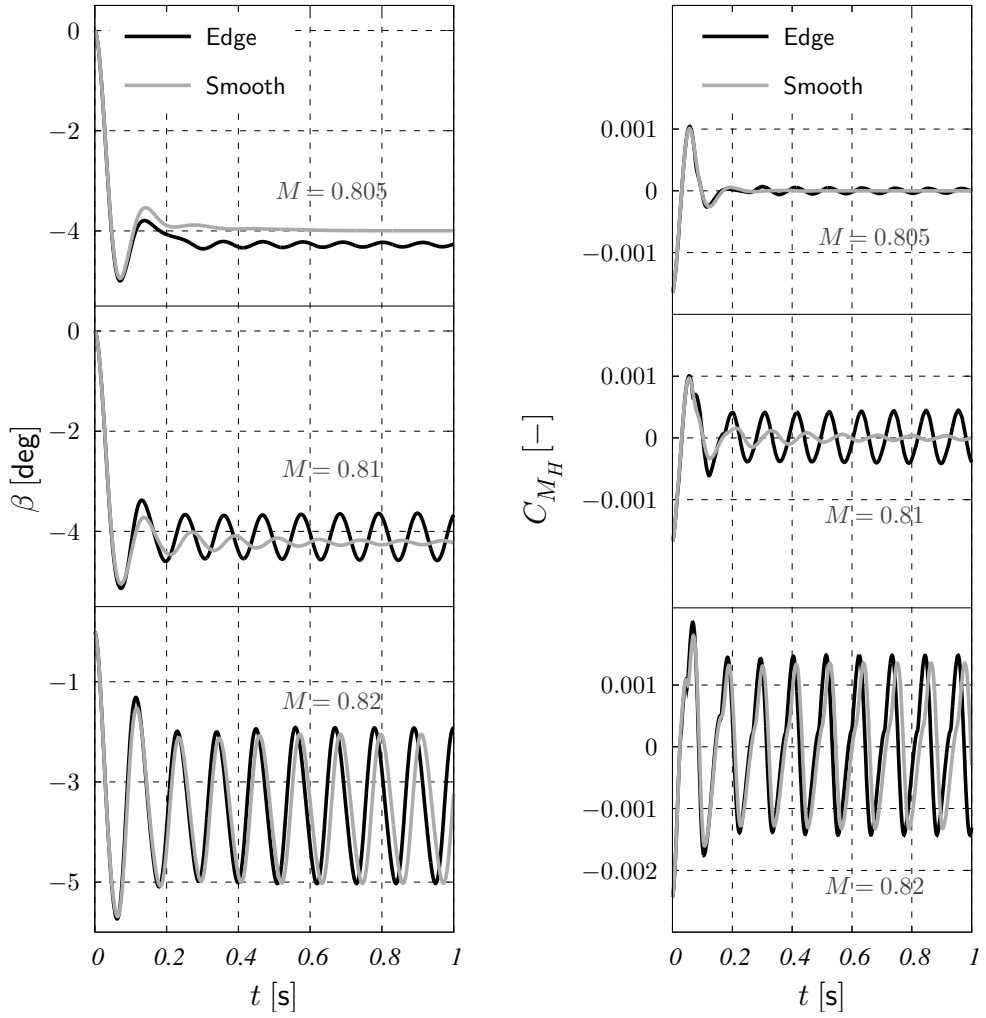

(a) Rotation (b) Moment

Figure 4.6: Comparison of system responses obtained with different Mach number, from top: $M = 0.805$, $M = 0.81$ and $M = 0.82$.

one another both from a quantitative and qualitative standpoint. As a matter of fact, at Mach number $M = 0.805$, the system responses are both stable, however the equilibrium deflection angle is different, due to the position after transient of the lower shock wave, that occurs ahead of the hinge line with the Smooth grid and that slightly moves behind the hinge line in the Edge case (Fig. 4.7). In addition, at Mach number $M = 0.81$ the difference is even more striking: the system response computed with the Smooth grid is stable, whereas the Edge grid yields aileron buzz. With further increase in Mach number, the responses are qualitatively the same, but they still differ in amplitude and frequency content. It is also

worth noting that the abrupt peak occuring during the transient response of the Edge solutions (Fig. 4.7) is caused by a steep and quickly-disappearing shock wave occurring just behind the hinge line because of the sudden deflection of the aileron.

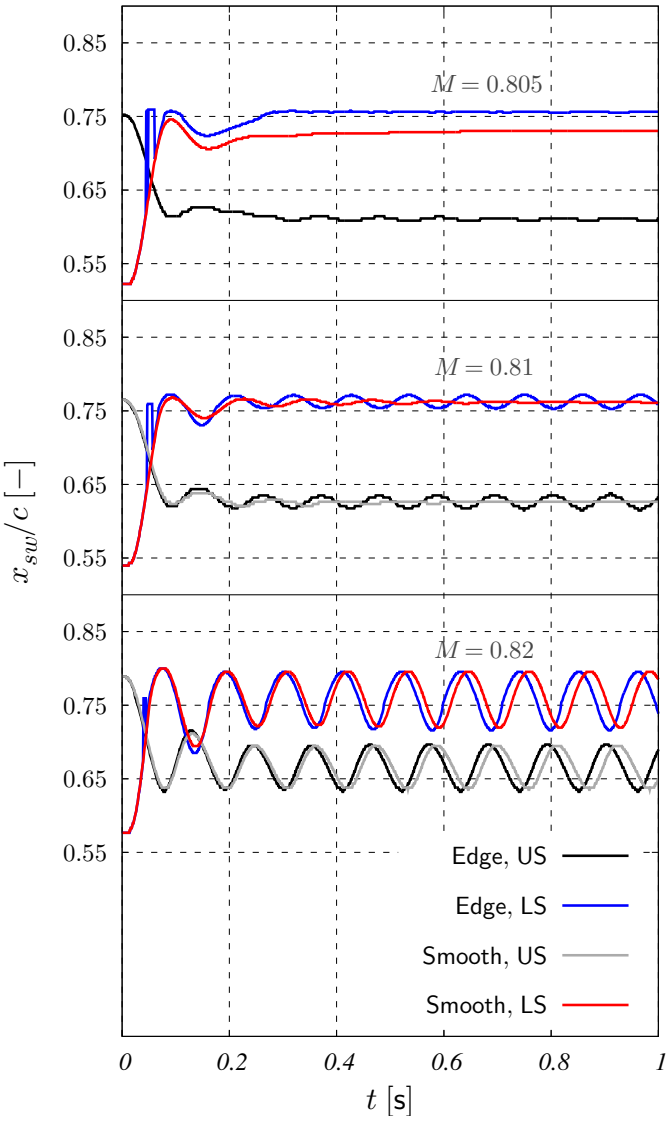

Figure 4.7: Shock wave dynamics at $M = 0.805$, $M = 0.81$ and $M = 0.82$ (US and LS stand for upper and lower surfaces).

In order to provide an understanding of the difference between the grids, it is convenient to consider separately the effects of a prescribed oscillation of the control-surface on the flowfield. Such analysis is the focus of the next section.

4.3.1 Response to a prescribed rotation

Exploiting the buzz amplitude and frequency observed at Mach number $M = 0.82$, a sinusoidal aileron rotation is prescribed with amplitude 1.6 deg around -3.5 deg and frequency 10 Hz. Figure 4.8 shows the resulting pressure field at four different time in the prescribed cycle, while the cycles of the deflection angle, moment and shock position are presented in Fig. 4.9 and Fig. 4.10. First of all, it is interesting to notice a typical feature of aileron buzz, namely the time lag between the peak of the deflection angle and the peak of the shock position (cf. Section 1.2), due to the time needed by the flow to adapt to the aileron displacement. In general, the time lag is longer because viscosity undoubtedly affects the

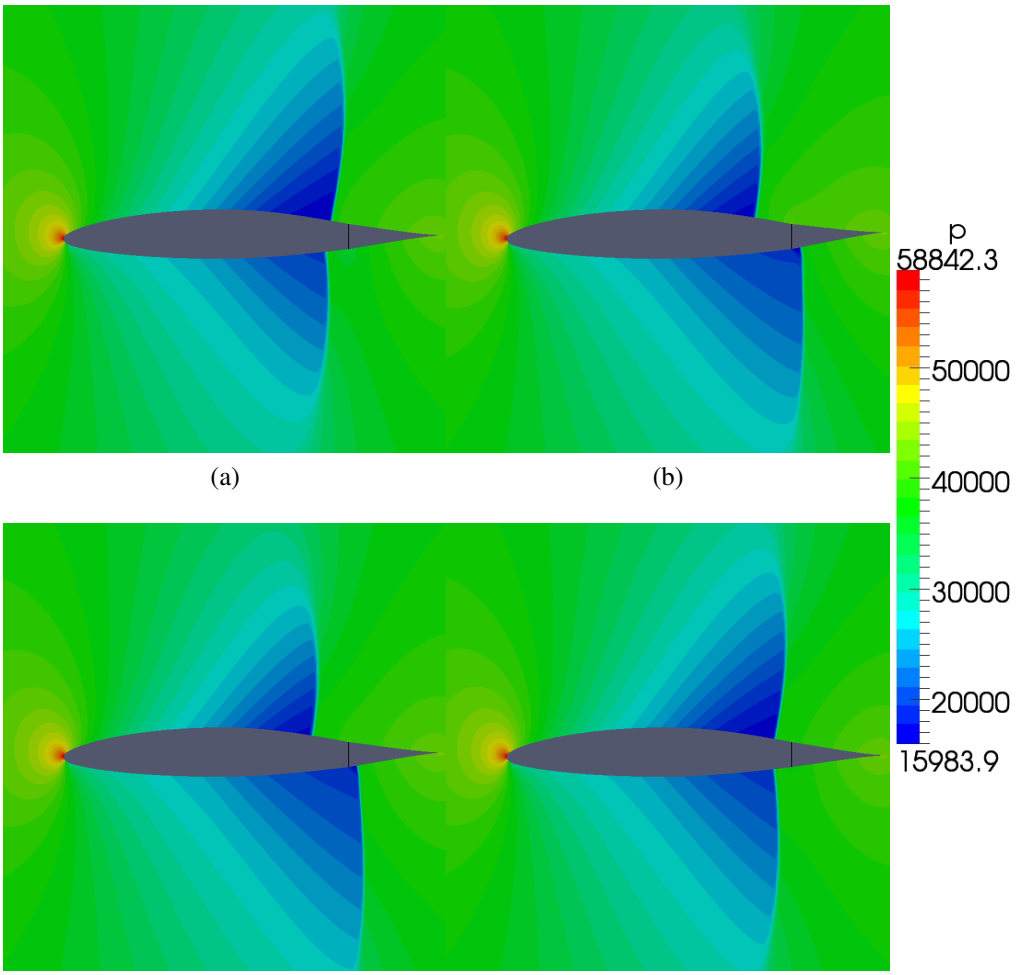

Figure 4.8: Snapshots of pressure field during a prescribed cycle: (a) initial, (b) maximum upward deflection, (c) half-period, (d) minimum negative deflection.

phenomenon and delays the effect on the shock wave dynamics of a sudden displacement of the aileron. However, because in the current work an inviscid model is employed, the effect is reduced yet still present, due to the flow nonlinearities. In addition, at maximum negative rotation amplitude for the Edge grid the load is still increasing, whereas the Smooth grid yields a decreasing load. In particular, the greater quantitative difference between the Edge and Smooth grids occurs at the point marked in Fig. 4.9, that is $t/T = 0.28$, where the Edge grid yields a stronger downward moment.

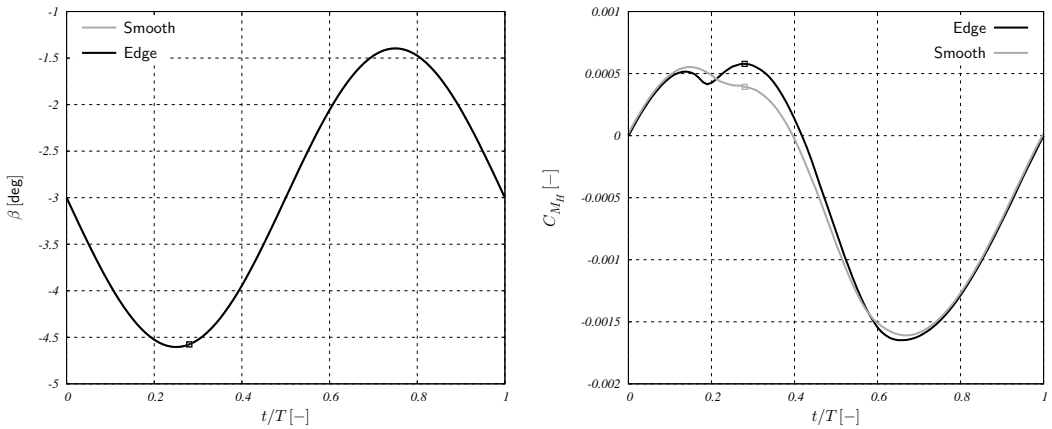

Figure 4.9: Cycle for prescribed rotation at $M = 0.82$: deflection angle (left) and hinge moment coefficient (right).

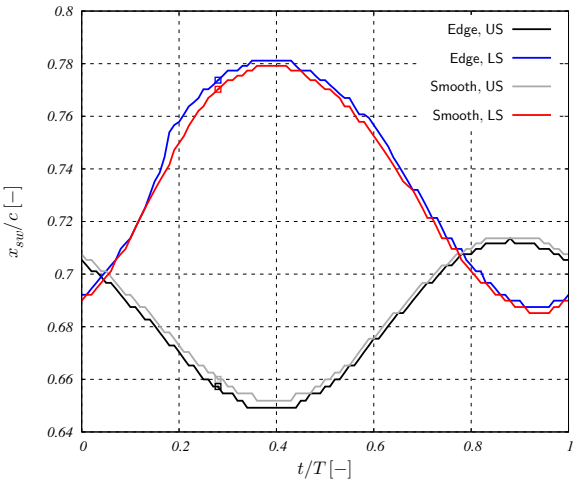

Figure 4.10: Cycle of shock wave position for prescribed rotation at $M = 0.82$.

Focusing on the pressure coefficient at that time, presented in Fig. 4.11, in concurrence with that upward deflection angle a strong shock wave occurs at the lower

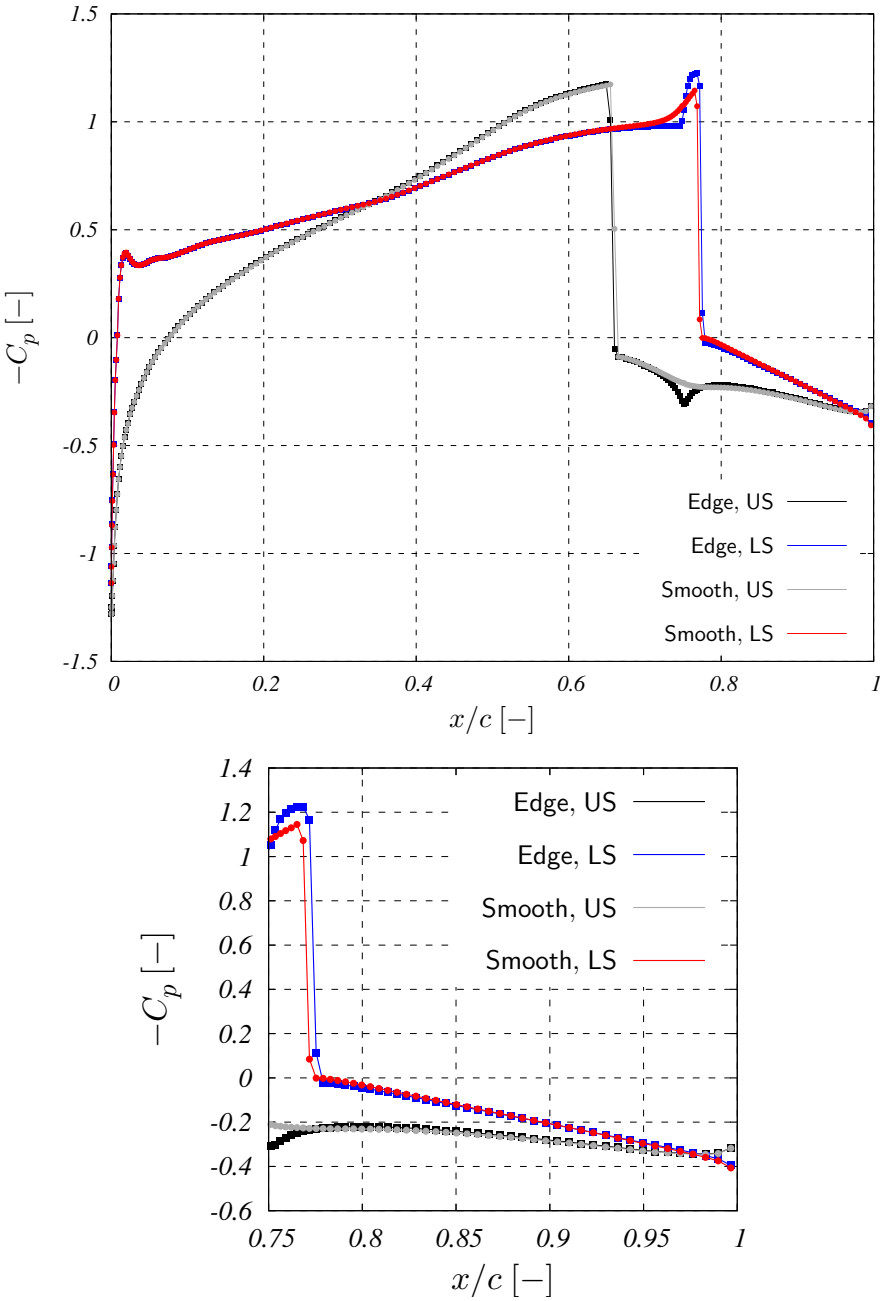

Figure 4.11: Pressure coefficient at $M = 0.82$ and $t/T = 0.28$.

surface of the aileron and its strength and position is different for the two grids. In particular, the position is more rearward and the shock wave has stronger intensity in the Edge case. The reason for this is that the edge between the main wing section and the deflected aileron causes an expansion wave, which in turn

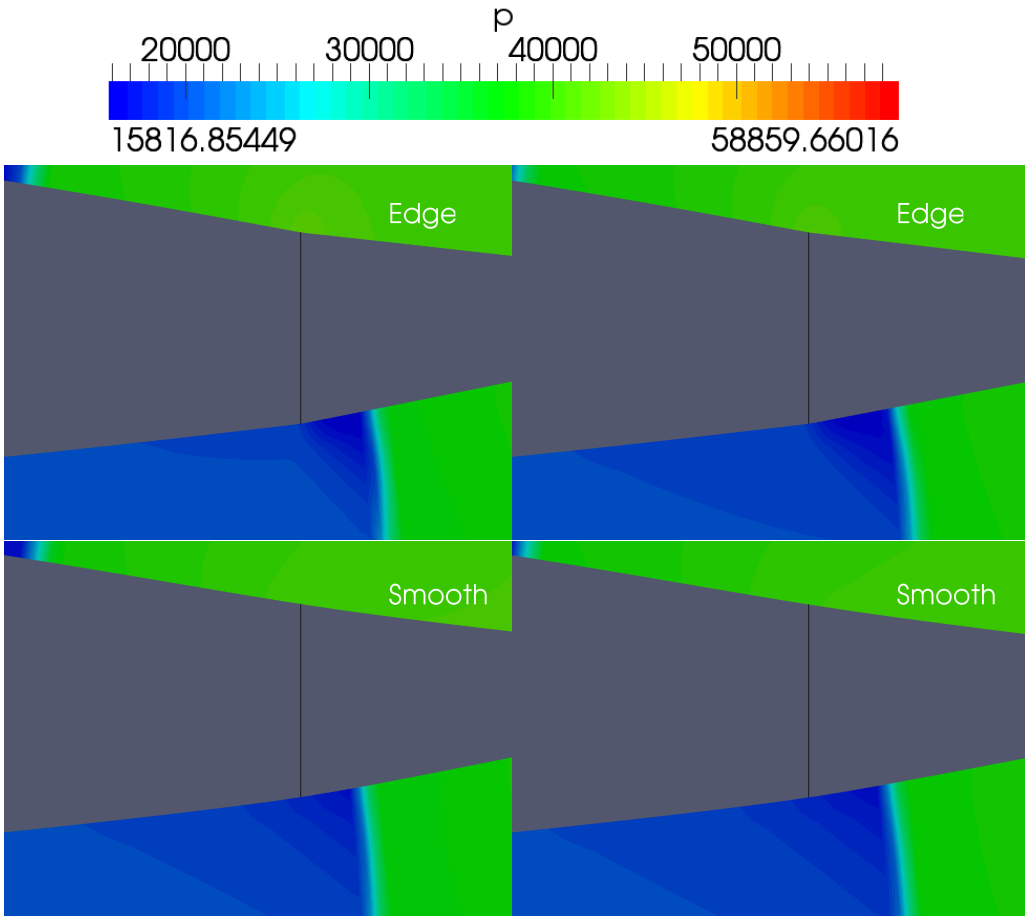

(a) (b)

Figure 4.12: Zoomed snapshots of pressure field: (a) maximum upward deflection, (b) maximum backward shock wave position.

produces a rapid change to a lower value of pressure and therefore a more intense shock wave is required for pressure recover. The contribution to the hinge moment of the discontinuity in the upper surface pressure coefficient for the Edge grid is not determining when compared to the effect of the expansion, mainly due to the closeness to the hinge line. The peculiar behavior of the pressure coefficient close to the trailing edge is related to a limited and imperceptible discontinuity in the normal vector of the last volumes of the wing boundary. However, the effects do not influence the current analysis due to its small contribution. Furthermore, the expansion is also detectable in the isobars shown in Fig. 4.12, which presents the pressure field at two instants of time, namely the time in which the aileron deflection is maximum upward and the subsequent time in which the shock position is most backward. In the figure, it is also interesting to notice that the difference be-

Peak frequency [Hz]	0	10	20	30
Error [%]	0.16	2.75	61.2	21.25

Table 4.1: Percentual error in peak values of load spectra.

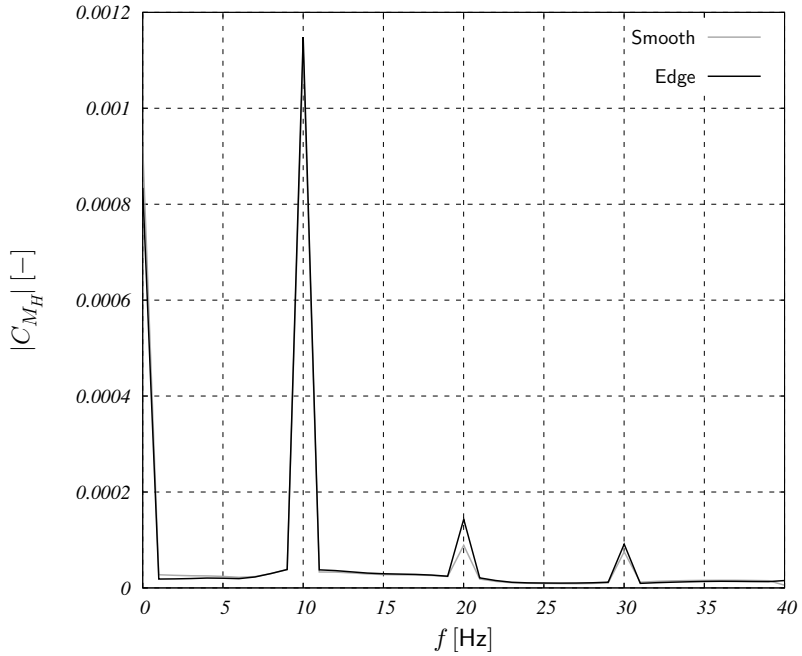

Figure 4.13: Frequency spectrum of the hinge moment coefficient.

tween the two grids is very difficult to perceive, thereby stressing that the details whose effect is considered are actually minimal, but still they have an appreciable influence on the system response. In addition, the analysis of the load spectra shows peaks in concurrence of multiple values of the basic frequency, namely the frequency of the prescribed rotation (Fig. 4.13). In particular, as expected from the variation in time presented in Fig. 4.9, the greater differences correspond to the higher frequency contributions (Tab.4.1).

Another test with prescribed rotation is performed at Mach number $M = 0.805$ (Fig. 4.14 and Fig. 4.15). The prescribed sinusoidal rotation is the same of the same value of the previous case in terms of amplitude and frequency, however the average value is set to the equilibrium rotation angle observed in the direct simulation (Fig. 4.6). Because the equilibrium angle is different for the two grids, it is not possible to eliminate from both grids the contribution of the unbalanced moment corresponding to the average rotation angle. Also, the multiple peaks evidenced in the load spectra for a prescribed rotation suggests that the nonlinear dynamics of buzz could be represented to a first approximation by a linear model,

whose input is a sequence of even polynomials of the system input. In this condition a similar trend to the one obtained at Mach number $M = 0.82$ is dected, that is the greater difference occurs when the aileron is deflected in the most upward position.

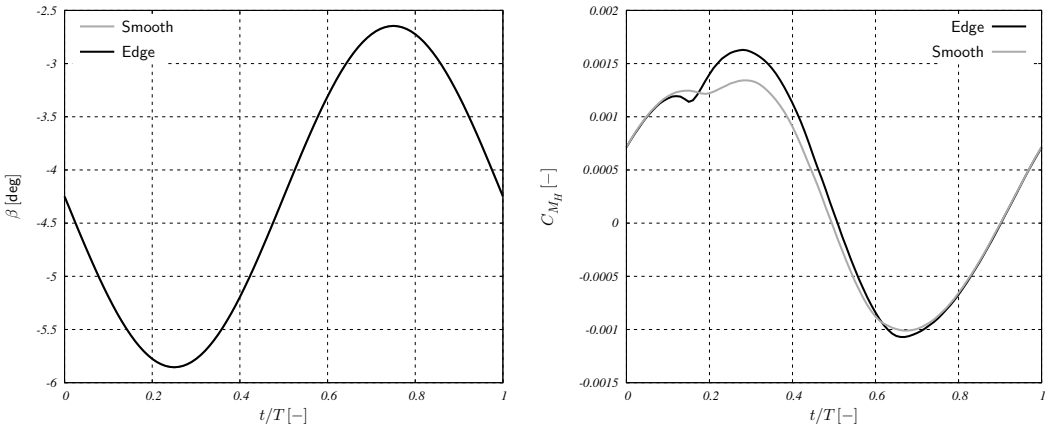

Figure 4.14: Cycle for prescribed rotation at $M = 0.805$: deflection angle (left), hinge moment coefficient (right).

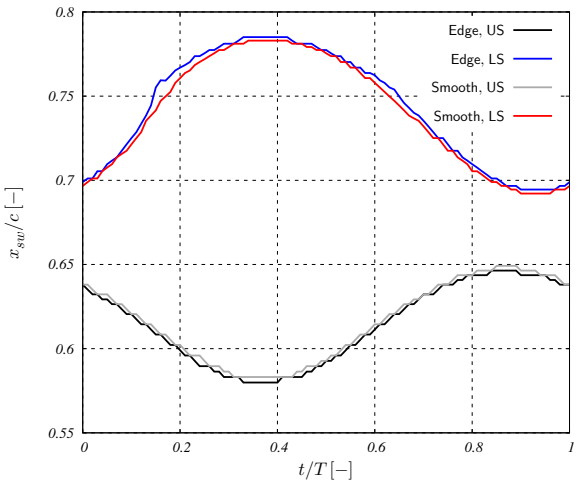

Figure 4.15: Cycle of shock wave position for prescribed rotation at $M = 0.805$.

4.3.2 Uncertainty estimate

Finally, an estimate of the range in which the two grids yield a qualitatively different response is computed by an extrapolation of the relationship between the Mach number and the logarithmic decrement. Because the latter is proportional

to the system damping ratio, the extrapolated Mach number at which the logarithmic decrement becomes zero would represent the Mach number for buzz onset. In particular, a linear extrapolation is chosen, exploiting the results at Mach numbers $M = 0.8$ and $M = 0.805$, that is where the response is overdamped. Figure 4.16 presents the curves resulting from the analysis and the range of discrepancy between the grids. The result points out that the Edge grid yields buzz at lower Mach number, as already observed in Fig. 4.6, and that the range in which the solutions are qualitatively different is [0.808, 0.8146], thereby producing an uncertainty of about 1%.

In conclusion, the convergence and geometry analysis points out that mesh refinement is crucial to obtain reliable results and that the choice between a smoothed and non-smoothed grid has an influence on the system response, both quantitatively and qualitatively. The study provides further insight into the numerical simulation of control-surface buzz, as well as flutter phenomena dominated by shock dynamics.

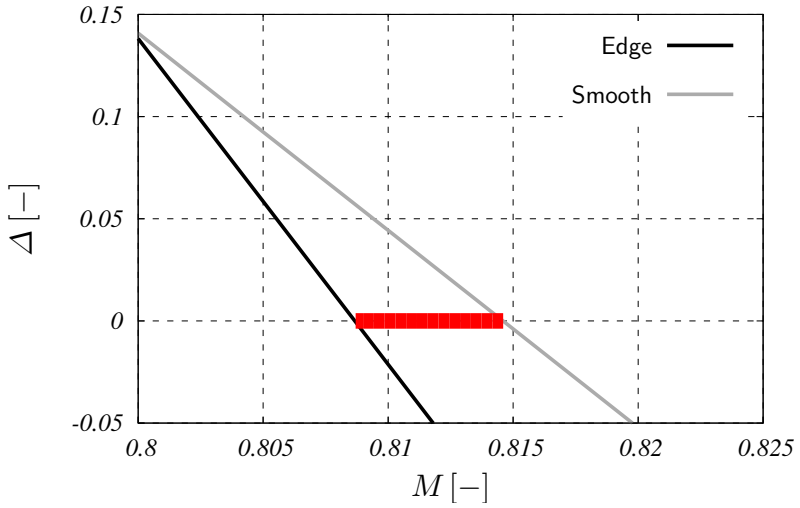

Figure 4.16: Extrapolation of logarithmic decrement plotted against Mach number.

Chapter 5

Aerodynamic reduced-order model

The previous chapters describe the analysis of aileron buzz employing a numerical model based on the CFD computation of the flowfield. A very attractive alternative to the CFD-based aerodynamic model is a surrogate aerodynamic model, i.e. a Reduced-Order Model (ROM), that is a low-order characterization of a physical process such that the essential behaviours of the process are captured with a relatively small number of degrees of freedom. According to Beran and Silva [27] the objective in defining a ROM is on the one hand to provide accurate descriptions of the dynamic system at a computational cost much lower than the original numerical model and on the other to build a means for a readily interpretation of the system dynamics. As a matter of fact, despite the growing efficiency of CFD calculations, the computational cost of numerical simulations is too high for CFD to be used in various multi-disciplinary settings, such as multi-objective optimization and stability prediction. In addition, the enormous size of computed datasets might impede the understanding of the essential features of the phenomenon of interest. As a result, ROMs might be a convenient analysis tool and it is also expected that they will experience an increase in industrial applications, thanks to the possibility of treating a wide range of load cases and flight conditions in the design stage [10].

The development of reduced-order models for the aerodynamics is a considerable activity in the field of aeroelasticity, where the employment of low-order models of the aerodynamic sub-system lessens the cost of stability predictions. The most common and well-established approach for the description of the aeroelastic problem is the *classical approach*, which is based on the representation of the model in the frequency space. Besides, the *modern approach* has gained momentum, which is based on the description of the governing equations in time. The typical governing equations of the aeroelastic system read

$$\boldsymbol{M}\ddot{\boldsymbol{q}} + \boldsymbol{C}\dot{\boldsymbol{q}} + \boldsymbol{K}\boldsymbol{q} = \boldsymbol{Q}_a\left(q_\infty, M_\infty\right),$$

where $\boldsymbol{M}$, $\boldsymbol{C}$ and $\boldsymbol{K}$ are respectively the structural mass, damping and stiffness

matrices, $\boldsymbol{q}$ is the generalized structural displacement and $\boldsymbol{Q}_a$ is the aerodynamic load, depending on the freestream Mach number M_∞ and dynamic pressure q_∞ (the dependence on the Reynolds number is minor and usually disregared). The load also depends on the structural displacement field because of the boundary conditions of the aerodynamic problem. It is therefore possible to define a relationship between the structural displacement and the aerodynamic load, that in the case of a linear(ized) model yields

$$\boldsymbol{M}\ddot{\boldsymbol{q}} + \boldsymbol{C}\dot{\boldsymbol{q}} + \boldsymbol{K}\boldsymbol{q} - q_\infty \int_0^t \boldsymbol{h}(t-\tau)\boldsymbol{q}(\tau)\mathrm{d}\tau = 0,$$

where in the previous equation the linear dependence of the load on the dynamic pressure q_∞ is made explicit and $\boldsymbol{h}(t-\tau)$ is the kernel function of the aerodynamic model, that is the relationship mapping the displacement $\boldsymbol{q}(\tau)$ into the load $\boldsymbol{Q}_a(t)$. Viable options in the construction of a mapping for the aerodynamic sub-system are: Volterra series theory and Volterra kernels identification using impulse or step inputs to the fluid system, Kahrunen-Loeve modes (proper orthogonal realization [28]) extracted from the dynamic response of the full-order fluid system when excited by proper inputs, (balanced) realizations of state-space theory, for instance, by means of Roger's method [29] and other identification methods based on input-output relations for the system based on systems theory [30]. In particular, the last methods ascribe to the process of defining a suitable mapping between the input and output of a dynamical system, which is usually called *system identification* in systems theory.

The objective of the current chapter is to develop a suitable reduced-order model of the aerodynamic sub-system for buzz analysis. The model should be capable of accurately and expediently estimating the unsteady CFD solution around the wing section of the aeroelastic model and predicting the time-varying load on the aileron. The definition of the ROM is carried out in the time domain, employing numerical techniques that belong to system identification. Section 5.1 is concerned with the general procedure and ingredients of system identification necessary to identify a low-order model of a dynamical system, whereas Section 5.2 presents the definition and development of the CFD-based ROM for the analysis of aileron buzz, as well as the comparison with CFD results.

5.1 System identification

System identification is a process for obtaining a mathematical model of a dynamic system based on a set of measured data from the system, namely input and output data [31, 32]. This methodology is used to fit the parameters of a given model structure to a set of recorded data from the dynamic system. The result is a reduced-order model, that is a mathematical map between the input and the output

of the system having reduced complexity with respect to the original system. The order and level of accuracy in the definition of the model structure depends on the application of such model and it is usually the result of a compromise among several requirements. System identification is widely employed in many areas, such as economics, geophysics and engineering, for analysis purposes, prediction of the behaviour of certain system variables with different inputs or conditions, implementation and verification of a possible control system. In general, the procedure of system identification is the following:

1. The first step is the analysis of the real dynamic system; as a matter of fact, the prior knowledge of the real system provides valuable information and guides the choice of the model structure that best suits the real system. At this stage it is also necessary to determine the objective of the model, so that the model structure possesses the proper level of accuracy with respect to its application. The knowledge of the real system not only yields the design of the experiment, the definition of the model structure and the identification strategy, but it is also involved in the calculation of the model to the extent that it indicates the reliability and fidelity of the computed model with respect to the real system.

2. The next stage is the design of the experiment from which the input and output sets are recorded. It is necessary to define which data are to be recorded, which excitation is to be used, as well as when to sample. In particular, the excitation is provided by a *training signal*, that is the input signal that excites the system and causes the system to produce an output, which is recorded for the identification. The characteristics of the training signal (e.g. amplitude, frequency) are set, having in mind both the model structure and the identification strategy. In some cases, the filtering of the recorded data is needed, in order to avoid potential aliasing or the effect of noises.

3. Parallel to the design of the experiment is the definition of the model structure that goes along with the choice of identification strategy or method. The model is defined by a structure based on a set of parameters or variables which are computed in the identification process in such a way that the resulting model fits best the real system. Thus, the identification relies on an optimization procedure that seeks the optimal variables of the given model structure in order to minimize a suited error. The possible choices and optimal criteria for the structures and methods are described in detail in Sections 5.1.1 and 5.1.2.

4. The calculation of the optimal parameters of the model structure is performed using algorithms and techniques suited for the chosen identification

method and training signal. At this stage many problems might be encountered arising mainly from numerical difficulties.

5. The validation of the model is required; in order to perform it, it is necessary to set *a priori* the indicators of a well-behaving model, based on the real system knowledge and recorded data. It is quite likely, though, that the model first obtained will not pass the validation test, because of a number of reasons mainly related to the fact that the success of the identification is dependent on the initial choice of the model structure and the amount and quality of the data used to train the model. In the case of missed validation, it is necessary to understand the reason of the failure and adjust training signals, model or method, accordingly.

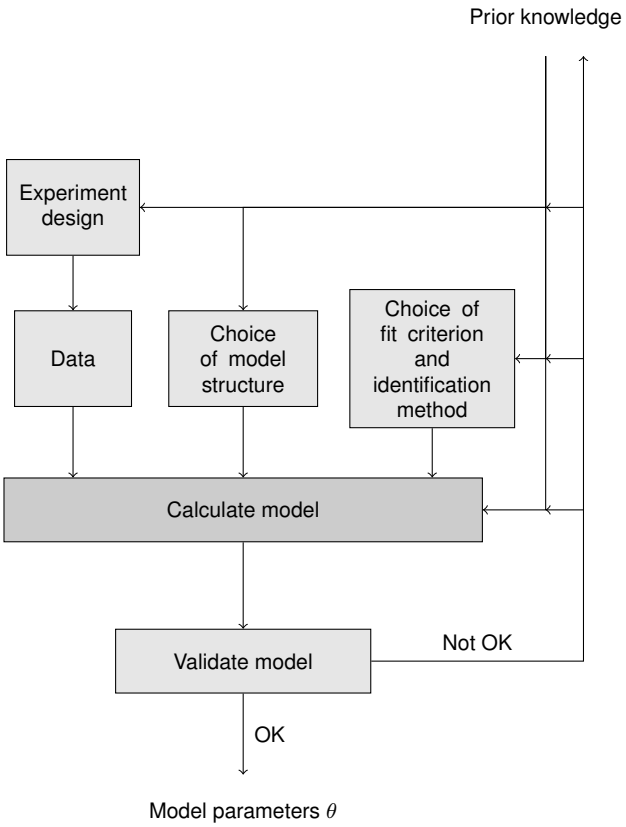

Figure 5.1: Flow chart of the identification procedure (from Ref. [31]).

5.1.1 Model structures

The model structure is the mathematical tool that maps the input of the system into the output of the system in the same way the real system would do. At the beginning of the identification process, it is necessary to define the model structure or model family $\mathcal{M}(\theta)$ and the corresponding model parameters θ that will be later computed. In general, the model structure should fulfill the following requirements:

(a) the model should be capable of representing the real dynamic system, even in an off-design condition;

(b) the model should be computationally efficient and easy to implement;

(c) in the case of coupling with other systems, the model should be compatible and ready for the numerical integration.

The model structures are manifold: depending on the application, one can choose from a wide variety of potential models that are distinguished, for instance, by the presence and absence of certain input signals, the accuracy order and level of detail, the type of representation. Here, a brief classification is proposed, which is comprehensive of the model types interesting for the system idenfication performed in the current work.

To begin with, a basic distinction is made between models whose behaviour is influenced by an *exogenous variable*, i.e. an input, and models that evolve on their own. To the former category belongs the typical linear time-indipendent systems of systems theory, while the latter models are represented by *time-series*, such as the logistic map. Another possible classification is based on the presence or absence of state variables; state variables are auxiliary variables describing the dynamic behaviour of a system. Even if the real system is dynamic and a complete state-space description would require the presence of state variables, it is also possibile in the identification process to disregard the state dynamics and reconstruct the relationship between the input and the output based only on the input and its derivatives. When the state variables are involved in the model structure the model is identified with a *state-space representation*, whereas in the absence of state variables the model is said to have an *external representation*. The description of the dynamic model is possible both using continuous time and discrete time. In the former case, that is in the *continuous-time representation*, the model variables apply to the time-varying vectors of input, output and possible state variables as a whole, whereas in the latter, namely in the discrete-time representation, the system variables apply to each discrete values of input and output sets. A bridge between the two representation is possible, employing the state-space representiation and a proper transformation from the discrete-time space to the continuous-time space.

A considerable issue encountered during the choice of the structure is related to the amount of realism and transparency of the model. As a matter of fact, it is possible to choose a *black box* model, that is a model structure that completely disregards and hides the physics of the real dynamic systems and emulates the input-output relationship using substitute variables unrelated to the real system. The black box model is usually employed when it is not possible to obtain a physical description of the real system or the complete description is too cumbersome and it is desirable to define a reduced-order yet sufficiently accurate model. Another possibility is that of employing a *transparent* model, namely a model based on the actual laws that determine the relationship between the variables involved in the dynamic system. In this case the objective of the identification is the determination of the system parameters. A great advantage of a transparent structure is that the model should behave exactly as the actual system and an incongruous outcome in the identification procedure is immediately recognizable. A halfway solution is the so-called *grey box* structure, which is basically a black box model, with some additional physical information on the real system.

Finally, some applications, such as adaptive prediction or control, require a model of the system that is available online while the system is operating, whereas in others the complete set of training data are available. The accessibility of the signals in time naturally influences the choice of the model structure, as well as of the identification method.

5.1.2 Methods

In order to calculate the model parameters θ, a suitable identification method is adopted, which is based on an optimization approach. As a matter of fact, the set of parameters is sought by means of the minimization of a given cost function. The cost function is a measure of the error between the identified output data and the recorded output data; a typical cost function is the mean quadratic error J defined as follows

$$J = \frac{1}{N_t} \sum_{k=1}^{N_t} \left[\varepsilon(t_k)\right]^2 , \tag{5.1}$$

where N_t is the number of samples of the error ε, which is given by the difference between the ouput y produced by the training signal and the identified output y_i evaluated at time sample t_k:

$$\varepsilon(t_k) = y(t_k) - y_i(t_k).$$

Once the cost function is defined, a suitable optimization strategy is chosen. In the foregoing, the methods whose implementation have been attempted in the current work are briefly discussed (cf. Ref. [32, 31] for further information).

The most classical choice for system identification is the least squares method. The cost function in Eqn. (5.1) depends on the input/output recorded data and the model parameters θ. Taking the derivative of the cost function with respect to the parameters and setting it to zero (i.e., the necessary condition for a minimum point) yields a system of equations, whose solution provides the model variables θ. Such a technique is widely employed in linear identification, but it presents difficulties with non-persistent excitations and might give rise to conditioning problems with increasing model order.

With the spread of (recurrent) neural networks (i.e. less transparent model structures having an internal dynamics) genetic algorithms have been employed, along with a more common approach based on the gradient method, which is also known as *back-propagation method*. The former is a global optimization strategy, which would promise to overcome the difficulty of restraining on a local minimum. It is based on the evolution concept, which states that only the genes belonging to the stronger individuals pass from one generation to the next one. In this case, the genes are the model parameters and the individuals are realizations of the model based on a set of genes. The optimal individuals are defined through the *fitness function*, which is the reciprocal of the cost function: the lower the cost function, the higher the fitness function and the ranking of the corresponding individual. In order to test different genes, random individuals are generated and interchanged on every advancing step of the algorithm until an optimal set of individuals is reached.

On the other hand, the back-propagation strategy is based on a gradient method, that produces a descent on the quadratic cost function $J(\theta)$ along the direction opposite to the gradient $dJ/d\theta$. Such methodology might incur into local minima and shows very poor convergence speed. Furthermore, both the gradient techniques and the genetic algorithms have a substantial computational cost, that might limit their applicability.

5.1.3 Training signals

The training signal is the input signal used in the experimental stage of the system identification procedure: a chosen input is prescribed to the real dynamic system in order to excite it and record the resulting output data. Naturally, the prescribed excitation should meet several multidisciplinary requirements among which are the following:

(a) The signal should be capable of exciting the frequency interval of interest with an amplitude that is sufficiently high to induce a measurable response, yet not overdriving the system. If the hypothesis of small perturbations is assumed, the signal should not exceed the linearity boundary; within such

a framework it is important to precisely define what is “high” or “small”, performing suitable linearity tests.

(b) The signal should be capable of dealing with the chosen identification method: as a matter of fact, coupling particular training signals and methods might give rise to numerical difficulties in the calculation of the model parameters;

(c) The signal should be realizable, that is compatible with the experimental layout: if an experiment is conducted, the excitation feasibility, intrusivity should be analysed, whereas in the case of a numerical experiment, the compatibility with the numerical methods and computational overhead should be taken into account.

In the foregoing a discussion is presented of the training signals that are most employed in the numerical identification of the aerodynamic sub-system for aeroelastic problems.

Harmonic input. A classical choice consists in persistently exciting the system with a simple harmonic input signal with prescribed frequency $\bar{\omega}$ and maximum amplitude A. Assuming that the system is Linear Time Invariant (LTI) and asymptotically stable, the frequency response theorem states that the output signal is also harmonic with equal frequency. As a consequence it is possible to compute the ratio between the output and input signal and extract the aerodynamic transfer function at frequency $\bar{\omega}$. Clearly such a strategy implies a high computational overhead, since it is necessary to repeat the numerical simulation for each reduced frequency inside the range of interest.

Frequency sweep input. Frequency sweeps are generated by smoothly varying frequency inside the bandwith of interest for a sinusoidal function; linear sweeps are also called *chirps*. By design, all frequencies within a specified bandwidth are excited. Frequency sweeps are common in the flight-test community. One dangerous disadvantage of the frequency sweep is the over-excitation of the structure, which often causes critical flight attitude.

Pulse input. Choosing an ideal impulse of infinite amplitude and zero width as input signal for exciting the aerodynamic subsystem, the aerodynamic impulse responses matrix at every time would be readily available. However, it is not possible to numerically implement an ideal impulse, but only a so-called *real impulse* of finite amplitude and width suitably chosen in order to excite the frequency interval of interest. Because a very small time step should be used in order to approximate the real impulse, a significant computational effort is required. Moreover,

unless a very wide time window is chosen, it is difficult to accurately identify the static gain and the low frequency dynamics of the aerodynamic sub-system.

Step input. In order to accurately identify also the static gain and the low frequency dynamics, it is convenient to choose as training signal an ideal step of prescribed maximum amplitude $\hat{A}$. Such a strategy is promising if only the geometric contribution (i.e. the contribution proportional to the structural displacement) is considered. Instead, when considering also the kinematic contribution (which involves the velocity field), the same problems stated above for the pulse input would arise. Moreover the Fourier transform of the output signal quite often presents spurious Gibbs oscillations, spoiling the accurate identification of the high frequency dynamics of the aerodynamic sub-system.

Blended step input. Finally, it is possible to choose a blended step input signal $I(t)$, which is given by:

$$u(t) = \begin{cases} 0 & \text{if} \quad t < 0 \\ \frac{A}{2}\left[1 - \cos\left(\bar{\Omega}t\right)\right] & \text{if} \quad 0 < t < t_{max} \\ A & \text{if} \quad t > t_{max} \end{cases} \tag{5.2}$$

where $\bar{\Omega}$ is the angular frequency, t_{max} is the half-period time of the cosine and A is the step amplitude. With non-dimensional variables the previous equation reads

$$u(\eta) = \begin{cases} 0 & \text{if} \quad \eta < 0 \\ \frac{A}{2}\left[1 - \cos\left(k_\Omega \eta\right)\right] & \text{if} \quad 0 < \eta < \eta_{max} \\ A & \text{if} \quad \eta > \eta_{max} \end{cases}$$

where $\eta = tV_\infty/L_\infty$ is the adimensional time, $k_\Omega = \bar{\Omega}L_\infty/V_\infty$ is the angular reduced frequency, $\eta_{max} = t_{max}V_\infty/L_\infty$ is the half-period non-dimensional time of the cosine and L_∞, V_∞ are respectively the reference length (i.e. the airfoil chord) and the freestream speed. The value of the angular velocity is set depending on the maximum frequency of interest f_{max} or its reduced counterpart $k_{max} = 2\pi f_{max}L_\infty/V_\infty$ and also dictates the half-period time:

$$\begin{aligned} k_\Omega &= \frac{k_{max}}{2} \quad \text{or} \quad \bar{\Omega} = \pi f_{max} \\ \eta_{max} &= \frac{\pi}{k_\Omega} \quad \text{or} \quad t_{max} = \frac{\pi}{\bar{\Omega}}. \end{aligned} \tag{5.3}$$

As a rule, the amplitude of the signal is chosen depending on the particular application and with regard to the possible limitations due to the signal feasibility or the linearity assumption.

5.2 Linear model for aileron buzz

With reference to Fig. 3.2, the ROM for the aerodynamic sub-system needs to map the input of the system, namely the aileron deflection angle β into the aerodynamic load acting on the aileron, that is the hinge moment M_H. The experiment for the identification is represented by a CFD computation of the aerodynamics with a suitable prescribed time history of the deflection angle, from which the hinge moment coefficient is recorded. From these sets of data, the calculation of the parameters is carried out, finally providing a substitute to the aerodynamic sub-system which can be easily integrated with the structural system, yielding a low-order aeroelastic model.

In the current section the reduced-order model for aileron buzz is presented, starting from the discussion of the model structure and the identification method and concluding with validation results.

5.2.1 Model and method

To begin with, the main charateristics of the model structure need to be set. With reference to the basic classification presented in Section 5.1.1, the definition of the main features of the ROM developed in the current work are discussed.

Model structure. The model is comprehensive of an exogenous variable, i.e. the input variable u_a, which in this case is the aileron deflection β. In addition, the model structure is described by means of a state-space representation: this choice is widely employed when dealing with CFD-based ROM, because it is capable of dealing with both high and low frequencies dynamics, as well as enabling an easy integration with the structural sub-system. A continuous-time representation of the model is also chosen, so that the integration with the structural sub-system and the solution of the aeroelastic system are more manageable thanks to the compact realization of the system. Such choices lead to the definition of the following system for the description of the mapping between the input u_a and the output y_a, (i.e. the hinge moment coefficient C_{M_H}):

$$\begin{cases} \dot{\mathbf{x}}_a = \mathbf{A}\mathbf{x}_a + \mathbf{B}\mathsf{u}_a \\ \mathsf{y}_a = \mathbf{C}\mathbf{x}_a + \mathsf{D}\mathsf{u}_a, \end{cases} \tag{5.4}$$

where $\mathbf{x}_a$ are the state-variables and matrices $\mathbf{A}$, $\mathbf{B}$, $\mathbf{C}$ and D are time-invariant matrices that determine the equation of state (the first one in Eqn. (5.4)) and the ouput equation (the second equation in Eqn. (5.4)). In addition, the system is assumed to be linear with respect to the input variable. This assumption would limit the capability of the identified model to represent the actual dynamic system, because the aerodynamics in the transonic regime presents strong nonlinearities

that would cause nonlinear dependence of the load with respect to the structural displacement (cf. Chapter 1). However, it is a convenient strategy in building a ROM to start from a model with lower complexity and then increasing the level of complication and transparency of the model until the desired fidelity is reached. This idea is also supported by the suggestion based on the frequency analysis of the response to a sinusoidal prescribed motion (cf. Chapter 4) that the dependence on the structural displacement in the problem of aileron buzz can be approximated by a linear dependence on an even polynomial of the input u_a. In this case a linear model would be sufficient, but it would be necessary to add other inputs (namely even powers of the input u_a) in order to take into account the system nonlinearities. As a result, the preliminary step is the construction of a linear model, which actually maps the variation of the input with respect to the initial value into the variation of the output with respect to the initial hinge moment coefficient. The choice of taking a variation with respect to the steady-state calculation leads to the interpretation of the model as a dynamic linearization performed around a nonlinear steady-state solution.

Furthermore, in order to define the structure of matrices $\mathbf{A}$, $\mathbf{B}$, $\mathbf{C}$ and D the idea of a grey-box model is pursued. As a matter of fact, the state variables $\mathbf{x}_a$ do not have a physical meaning and they are simply employed to resemble the dynamics of the system, thereby yielding a model structure with very low transparency level. However, it is possible to add information about the actual dynamic system in order to improve the low-order model and ease the identification process. The analysis in Chapter 1 and the numerical study presented in Chapter 4 surely provide a good prior knowledge of the phenomenon which drives the following observations.

Considering the aerodynamics as a dynamic system, it is reasonable, at least in the case of interest, to assign to the model the property of asymptotic stability with respect to perturbations related to a structural displacement. In addition, because the focus of the work is on a phenomenon dominated by oscillations and harmonic behaviours, an appropriate choice for the eigenstructure of the system is based on complex eigenvalues that, containing both a real and an imaginary part, will contribute to the oscillating behaviour of the system. As a result, the model should possess complex conjugate eigenvalues with negative real part: the easiest way to assign the eigenstructure to matrix $\mathbf{A}$ is that of building a diagonal matrix with two-by-two blocks, each of which has the desired couple of complex eigenvalues.

A further assumption is introduced into the model structure: a diagonal matrix with two-by-two blocks is, for instance, the state-space representation of a dynamical system based on a parallel of second-order systems. Leveraging on this idea, the aerodynamic model structure is built as a parallel of internal second-order sub-systems, which are modelled as mass-spring-damper systems. A partial jus-

tification of this choice might be supported by the following physical abstraction: treating the flow as a solid continuum, the flowfield is regarded as if it were the displacement and velocity field of a solid continuum. The effect of the compressibility of the flow translates somehow in hypothetical damping and flexibility. In particular, the basic structure of the i-th internal sub-system is the following

$$\begin{cases} \dot{\tilde{\mathbf{x}}}_i = \begin{bmatrix} 0 & 1 \\ -\mathsf{k}_i/\mathsf{m}_i & -\mathsf{d}_i/\mathsf{m}_i \end{bmatrix} \tilde{\mathbf{x}}_i + \begin{bmatrix} 0 \\ 1/\mathsf{m}_i \end{bmatrix} \mathsf{u}_a \\ \tilde{\mathsf{y}}_i = \begin{bmatrix} 1 & 0 \end{bmatrix} \tilde{\mathbf{x}}_i, \end{cases} \tag{5.5}$$

where m_i, d_i and k_i are respectively mass, damping and stiffness coefficients, while the output $\tilde{\mathsf{y}}_i$ of the internal system is the position of the state $\tilde{\mathbf{x}}_i$. Actually, because the state variables do not have a physical meaning and neither have the stiffness and damping coefficients, it is legitimate to redefine the state variables as $\mathbf{x}_i = \mathsf{m}_i \tilde{\mathbf{x}}_i$ and the coefficients as $\mathsf{a}_i = \mathsf{k}_i/\mathsf{m}_i$ and $\mathsf{b}_i = \mathsf{d}_i/\mathsf{m}_i$, thereby obtaining the following representation

$$\begin{cases} \dot{\mathbf{x}}_i = \begin{bmatrix} 0 & 1 \\ -\mathsf{a}_i & -\mathsf{b}_i \end{bmatrix} \mathbf{x}_i + \begin{bmatrix} 0 \\ 1 \end{bmatrix} \mathsf{u}_a \\ \mathsf{y}_i = \begin{bmatrix} 0 & 1 \end{bmatrix} \mathbf{x}_i, \end{cases} \tag{5.6}$$

This condensed representation is used to reduce the number of the model parameters, alleviating the cost of the identification method procedure. To this end, in the parameters calculation it is also assumed that coefficients a_i an b_i are multiple of the basic coefficients a_1 and b_1; the assumption is driven by the need of further reducing the number of the optimization parameters and it is considered a good strategy to span the frequency range of interest without aggravating the computational cost of the minimization procedure. Finally, the amplitude of the internal system outputs is then tuned by the output layer of the model structure which operates a linear combination of the internal outputs by the emplyment of the amplification factors c_i:

$$\mathsf{y}_a = \mathsf{c}_1 \mathsf{y}_1 + \ldots \mathsf{c}_N \mathsf{y}_N.$$

The output equations is completed by adding a contribution proportional to the input and its first and second derivatives, that is

$$\mathsf{D}_0 \mathsf{u}_a + \mathsf{D}_1 \dot{\mathsf{u}}_a + \mathsf{D}_2 \ddot{\mathsf{u}}_a,$$

where the coefficients D_0, D_1 and D_2 are to be determined in the identification process. Such terms not only represent the contribution at low frequency of the higher frequency dynamics, but also provide an additional mass, damping and stiffness for the complete aeroelastic system.

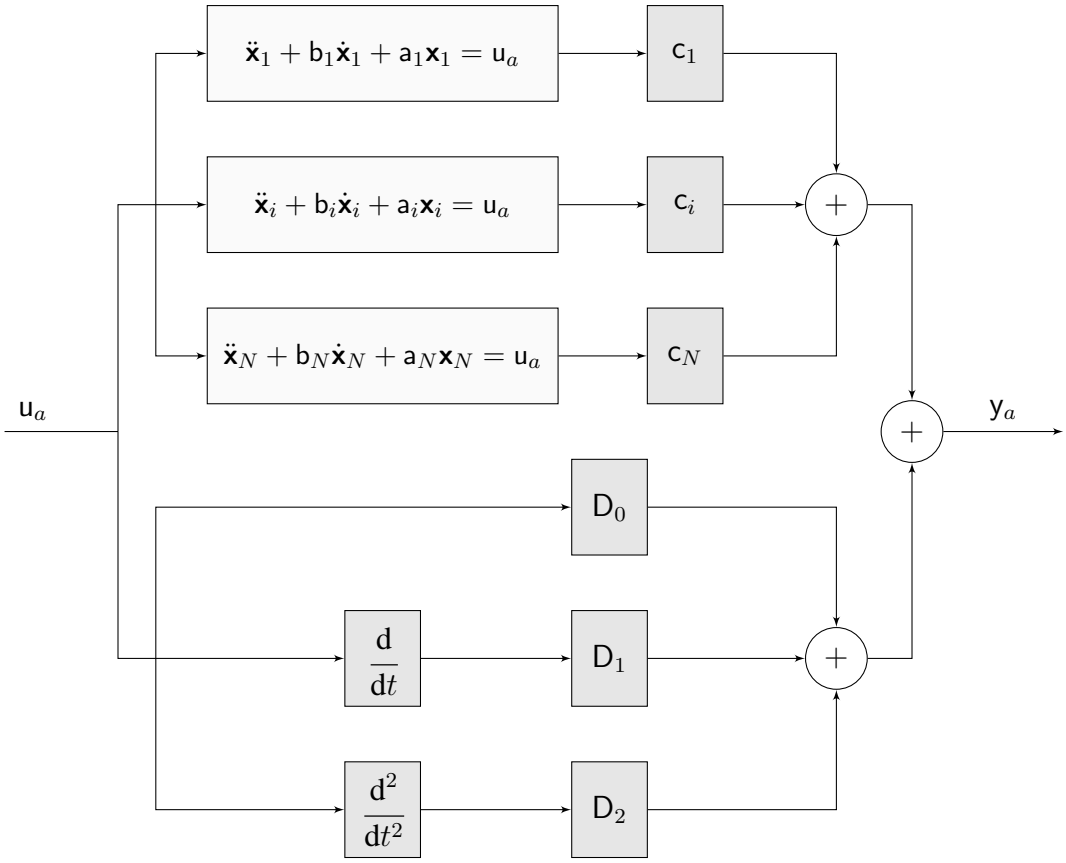

Figure 5.2: Block diagram of the aerodynamic model structure.

Thus, the system needs to be enlarged as follows

$$\begin{cases} \dot{\mathbf{x}}_a = \mathbf{A}_a\mathbf{x}_a + \mathbf{B}_a\mathbf{u}_a \\ \mathsf{y}_a = \mathbf{C}_a\mathbf{x}_a + \mathbf{D}_a\mathbf{u}_a, \end{cases} \tag{5.7}$$

and the resulting states, inputs $\mathbf{u}_a$ and matrices $\mathbf{A}_a$, $\mathbf{B}_a$, $\mathbf{C}_a$ and $\mathbf{D}_a$ are given by

$$\mathbf{x}_a = \begin{Bmatrix} \vdots \\ \mathbf{x}_i \\ \vdots \end{Bmatrix} \qquad \mathbf{u}_a = \begin{Bmatrix} \mathsf{u}_a \\ \dot{\mathsf{u}}_a \\ \ddot{\mathsf{u}}_a \end{Bmatrix}$$

$$\mathbf{A}_a = \begin{bmatrix} \ddots & & \\ & \begin{bmatrix} 0 & 1 \\ -\mathsf{a}_i & -\mathsf{b} \end{bmatrix} & \\ & & \ddots \end{bmatrix} \qquad \mathbf{B}_a = \begin{bmatrix} \vdots & \vdots & \vdots \\ \begin{bmatrix} 0 \\ 1 \end{bmatrix} & 0 & 0 \\ \vdots & \vdots & \vdots \end{bmatrix}$$

$$\mathbf{C}_a = \begin{bmatrix} \dots & \begin{bmatrix} \mathsf{c}_i & 0 \end{bmatrix} & \dots \end{bmatrix} \qquad \mathbf{D}_a = \begin{bmatrix} \mathsf{D}_0 & \mathsf{D}_1 & \mathsf{D}_2 \end{bmatrix}$$

The outline of the system is sketched in Fig. 5.2; the variables a_i, b_i, c_i and D_0, D_1, D_2 constitute the set of parameters θ that are calculated according to an optimization criterion to determine the best fit of the model structure with respect to the actual dynamic system.

Method. To begin with, a modified least squares method is employed. The approach is based on the separate minimization of two quadratic cost functions of the form

$$J = \frac{1}{N_t} \sum_{k=1}^{N_t} \varepsilon(t_k)^T \varepsilon(t_k),$$

which are respectively based on the error $\boldsymbol{\varepsilon}_x$ associated to the equation of state

$$\boldsymbol{\varepsilon}_x(t_k) = \dot{\mathbf{x}}_a(t_k) - \left(\mathbf{A}_a \mathbf{x}_a(t_k) + \mathbf{B}_a \mathbf{u}_a(t_k)\right),$$

and the error of the output equation $\boldsymbol{\varepsilon}_y$

$$\boldsymbol{\varepsilon}_y(t_k) = \mathsf{y}_a(t_k) - \left(\mathbf{C}_a \mathbf{x}_a(t_k) + \mathbf{D}_a \mathbf{u}_a(t_k)\right).$$

In order to minimize the quadratic form, the derivative of the cost function is taken with respect to the model parameters, that is the coefficients in matrices $\mathbf{A}_a$, $\mathbf{B}_a$, $\mathbf{C}_a$ and $\mathbf{D}_a$. The state variables should be provided, but these are unknown, because the experiment only yields input and output data set. Thus, it is assumed that to a first approximation the state variables are approximately the output variables: in particular, because the output is proportional to the state displacement, the state is reconstructed from the output and its first derivative. This approach yields two decoupled systems of equations, whose solutions are the parameters θ. Nevertheless, the approach proves to be effective in a wide range of cases only for a model structure containing one internal sub-system, but it is ineffective most of the times for high-order model, unless the frequency content of the output presents clearly separated peaks. The reason for the limited capability of this approach is likely to be related to the assumption that the state can be approximated with the system output. The assumption is acceptable in the case of a limited contribution of the input in the output equation when the coefficients c_i are nearly unit. As a matter of fact, it is crucial to provide each internal sub-system with the correct internal output y_i, which might differ to a large extent from the total output y_a.

Another possibility is the back-propagation strategy. In this case a gradient method is implemented, which seeks for a minimum along a descent direction in the quadratic function J, namely the direction opposite to the gradient $dJ/d\theta$. To this end, the model structure is subdivided into layers (an output layer, which is represented by the output equation, and an inner layers based on the inner subsystems) and the gradient is computed starting from the last, outer layer to the inner layer. Because the model structure has an inner dynamics, it is necessary

to write the differential equation governing each inner second-order sub-systems with an explicit technique and "unfold" each sub-system through time, yielding a series of feed-forward systems for each internal second-order sub-systems. Thus, the computational cost of the procedure is severe and the functional cost often flattens on a local minimum point far from the solution of the problem.

Therefore, a method based on the genetic algorithm is chosen. Such an approach permits to train the system from the input to the output and does not rely on further assumptions on the internal variables of the system. The genetic algorithm is based on an iterative scheme, which creates at each iteration a new set, or generation, of individuals distinguished by a set of genes that try to evolve to better solutions [33]. The genes are the model parameters, therefore each individual is associated to one realization of the model. The reciprocal of the cost function J (cf. Eqn. 5.1) is called fitness function and needs to be evaluated at each iteration for each individual. The evaluation of the fitness function implies integrating the associated system in time and the integration is performed by means of the energy-preserving Crank-Nicolson scheme. Once the fitness function is evaluated the ranking of the individuals of the current generation is carried out: the better individuals are the ones having the higher value of fitness function and the corresponding genes or parameters are the stronger. The next generation is then generated according to the following criteria: a small part is constitued by the stronger individuals of the previous generation, another small set is the result of the random crossover of strong individuals, a set comes from a perturbation mutation of randomly chosen previous individuals and a substantial part is produced by random selection of the genes. The loop is represented in Fig. 5.3. When the maximum number of iterations is reached or the error is lower than a given tolerance the method stops. The error is based on a quantity measuring the dispersion of the genes in the current generation, leveraging the assumption that the optimum point in the genetic evolution is reached when all the individuals in a generation possess (almost) the same genes.

The counterpart of the approach is the conspicuous computational cost that is needed to evaluate the functional cost for each individual at every iteration. In order to speed up convergence, several modifications are introduced. First of all, a least square method is employed only for the output equation of the system Eqn. (5.7); in this case, the trained internal signal y_i and the state variables $\mathbf{x}_a$ is readily available from the integration of the equation of state and there is no need for further assumption. The inclusion of the least square approach reduces the number of genes, because only coefficients a_i and b_i) constitute the set of genes for each individual. In addition, the ranges in which the parameters need to be sought are appropriately set. In particular, limits are defined for the parameters that exclude negative values of a_i and b_i and real values of the corresponding eigenvalues of matrix $\mathbf{A}$. Furthermore, during the loop the limits of each parame-

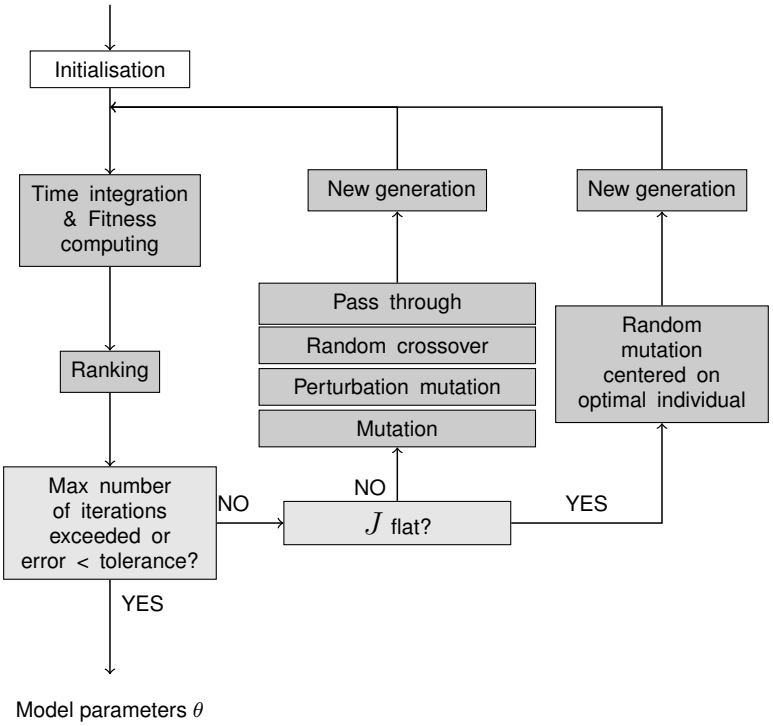

Figure 5.3: Outline of the genetic algorithm.

ter is progressively and slowly restricted around the current optimal genes, so that the convergence to the optimal state is accelerated yet avoiding excessive boundings to the algorithm. This also provides a certain "freedom" to the method with respect to the possible values of the model parameters: in fact, if the initial ranges are such that the optimal genes fall outside the prescribed range, the method is still capable of reaching the optimal values changing the limit correspondingly.

Furthermore, when cost function flattens with increasing number of iterations, settling on a value distant from the optimal point, the genes for the next generation are randomly chosen inside a range centered on the values of the genes of the optimal individual. In this way new evaluations are computed and a possible better individual is found. This operation usually produces high peaks in the behaviour of the cost with respect to the number of iterations, but is indeed very effective.

Finally, an incremental approach is employed to aid the identification process. In particular, the genetic algorithm is run more than one time and at each time a small number of internal sub-systems is considered. Such an approach permits a good convergence and accuracy of the genetic algorithm that attempts to catch first the most significant contributions to the system ouput and then the minor contributions. In addition, when the algorithm is run after the identification of the first small model, the fitness function is based on a modified cost function, which

contains a contribution that is proportional to the error between the identified and recorded outputs at the time instant $\bar{t}$ where they differ the most. Thus the cost function of the genetic algorithm J_{ga} is the following

$$J_{ga} = \rho_1 \frac{1}{N_t} \sum_{k=1}^{N_t} \left[\varepsilon(t_k)\right]^2 + (1-\rho_1)\left(y(\bar{t}) - y_i(\bar{t})\right)^2,$$

where the weighting coefficient ρ_1 is set equal to 1 in the first loop and then it is equal to 0.3, as a result of a brief analysis of the accuracy of the identified signal. This expedient is used to catch the greatest difference in the system responses yet maintaining the overall behaviour, thereby obtaining a more accurate identification.

Training signal. The chosen training signal is the blended step input: this signal allows to excite all the frequency falling inside a desired bandwith and overcome the numerical difficulties arising with the other input signals. The angular frequency Ω and the half-period time t_{max} are set in such a way that the frequency interval [0, 200] Hz is excited (cf. Eqn. (5.2) and Eqn.(5.3)), because the frequency analysis of the direct simulation shows non-null contributions up to that value. The amplitude of the step is selected within the bounds dictated by the linearity assumption and the capability of the numerical solver to cope with the almost sudden boundary and mesh movement. In particular, starting with a signal having amplitude $A = -1$ deg (which is considered not to exceed the linearity limit), the identification is carried out for signals with amplitude increasing up to $A = -3$ deg, which is either the average value or the steady-state value of most aeroelastic direct calculations. The resulting identification does not show any substantial difference in terms of identified solution, thus the higher amplitude is considered not to overstep the linearity bound.

Aeroelastic model. The low-order aeroelastic model is obtained by the integration of the aerodynamic state-space realization (cf. Eqn. (5.7)) with the structural sub-system, whose state-space realization reads

$$\begin{cases} \dot{\mathsf{x}}_s = \begin{bmatrix} 0 & 1 \\ 0 & 0 \end{bmatrix} \mathsf{x}_s + \begin{bmatrix} 0 \\ 1/I_H \end{bmatrix} \mathsf{u}_s \\ \mathsf{y}_s = \begin{bmatrix} 1 & 0 \end{bmatrix} \mathsf{x}_s, \end{cases}$$

where the input $\mathbf{u}_s$ is the aerodynamic load $M_H = q_\infty c^2 C_{M_H} = q_\infty c^2 \mathsf{y}_a$ and the output y_s is the aileron deflection angle β. The resulting aeroelastic model is the

following

$$\dot{\mathbf{x}}_{ae} = \begin{bmatrix} \begin{bmatrix} 0 & 1 \\ \dfrac{\mathsf{D}_0}{I_{ae}} q_\infty c^2 & \dfrac{\mathsf{D}_1}{I_{ae}} q_\infty c^2 \end{bmatrix} & \begin{bmatrix} \dots & 0 & \dots \end{bmatrix} \\ \begin{bmatrix} \vdots \\ \begin{bmatrix} 1 \\ 0 \end{bmatrix} \\ \vdots \end{bmatrix} & \begin{bmatrix} \vdots \\ 0 \\ 0 \\ \vdots \end{bmatrix} \end{bmatrix} \begin{bmatrix} \dfrac{q_\infty c^2}{I_{ae}} \mathbf{C}_a \\ \mathbf{A}_a \end{bmatrix} \mathbf{x}_{ae}$$

where $I_{ae} = I_H - \mathsf{D}_2 q_\infty c^2$. The integration in time is started from the initial unbalanced aerodynamic moment and is performed by means of the Crank-Nicolson scheme. The rotation angle and moment are then recovered as follows

$$\beta = \begin{bmatrix} 1 & 0 & \dots & 0 \end{bmatrix} \mathbf{x}_{ae}$$
$$M_H = q_\infty c^2 \left(\mathbf{C}_a \mathbf{x}_{ae} + \mathsf{D}_0 \beta + \mathsf{D}_1 \dot{\beta} + \mathsf{D}_2 \ddot{\beta} \right).$$

5.2.2 Results

The system identification is first employed to represent the stable aeroelastic response at Mach number $M = 0.8$. The recorded output data is presented with a blue line in Fig. 5.4, whereas the aerodynamic identified response is represented

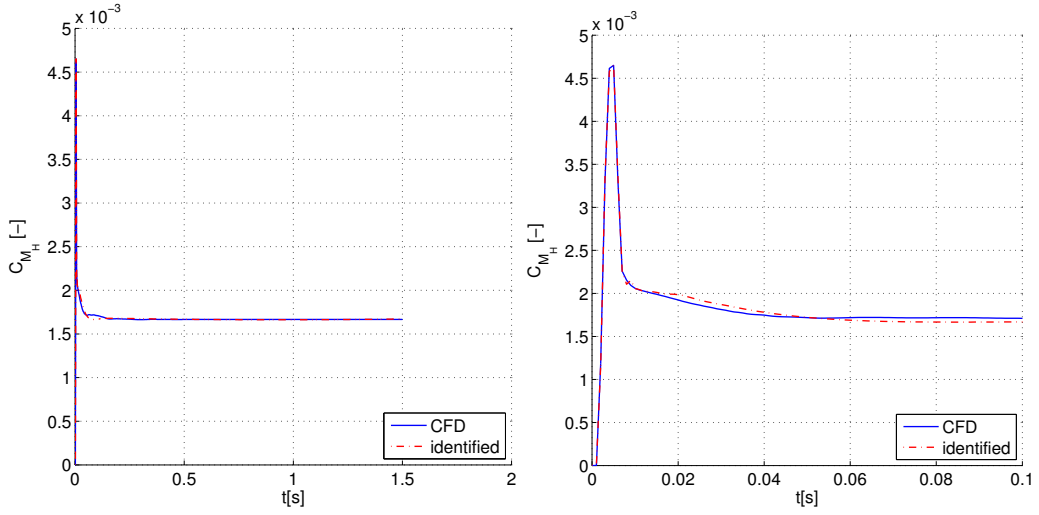

(a) Aerodynamic output (b) Zoom

Figure 5.4: Comparison of the recorded CFD-based response and the identified response subsequent to the prescribed input signal (Mach number $M = 0.8$).

by the red curve. The overall behaviour of the aerodynamic response is well represented by the identified model; slight differences are noticeable at the very high

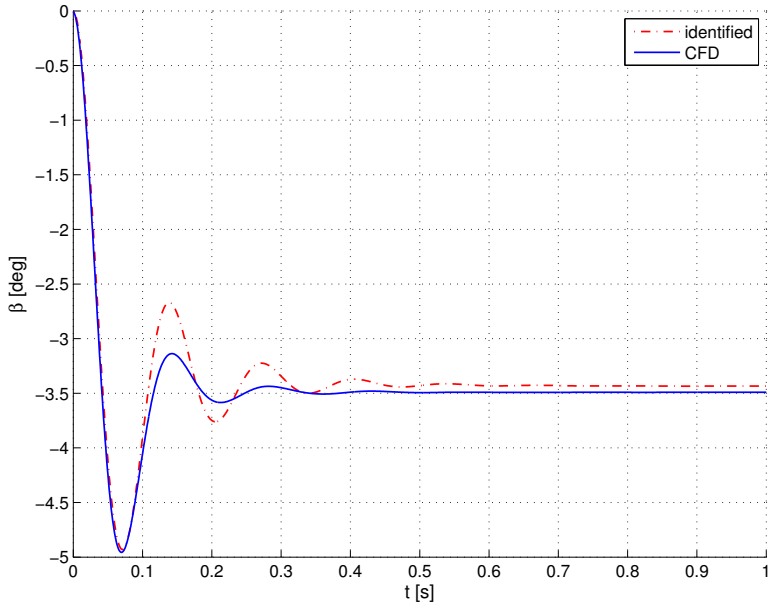

(a) Rotation

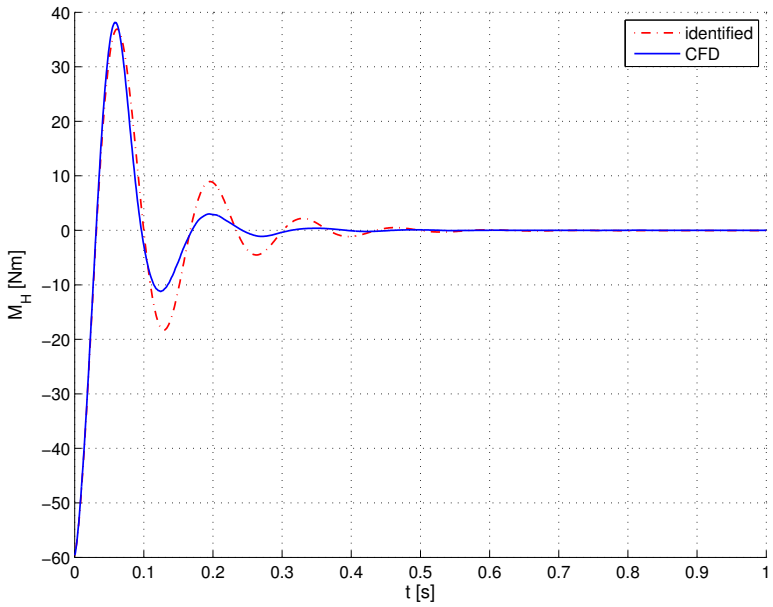

(b) Moment

Figure 5.5: Comparison of system responses between the aeroelastic CFD-based model and the aeroelastic ROM-based model (Mach number $M = 0.8$).

peak and in the subsequent instants when the response slowly oscillates until it reaches a steady state.

Then, the complete aeroelastic response in terms of aileron deflection and the hinge moment obtained with the reduced-order model is compared with the results of the direct numerical simulation in Fig. 5.5. The plot shows good agreement, especially in the first instants of time; however, after the first peak a discrepancy in the system damping ratio is evident, while the frequency of the signal is predicted with good accuracy. The reason for this is probabily twofold: on one side the linear model structure is not capable of representing a variable damping ratio, which in the actual system is not constant with time; on the other side the linear model strictly depends on the initial perturbation which would probably cause the model to effectively resemble the system response for the inital part of the response, but would lack in accuracy on the remaining instants of time. Furthermore, the accuracy of the identified model close to the first peak is taken as the indicator of a good identification. Thus it is possible to operate a brief convergence analysis, that shows an improvement on the system response up to 12 internal systems, whereas higher-order models produce highly oscillating yet damped responses, which usually suggest that the order of the system exceeds the necessary value (Fig. 5.6). Therefore, the identification has been carried out using 12 internal system, thereby employing 26 states.

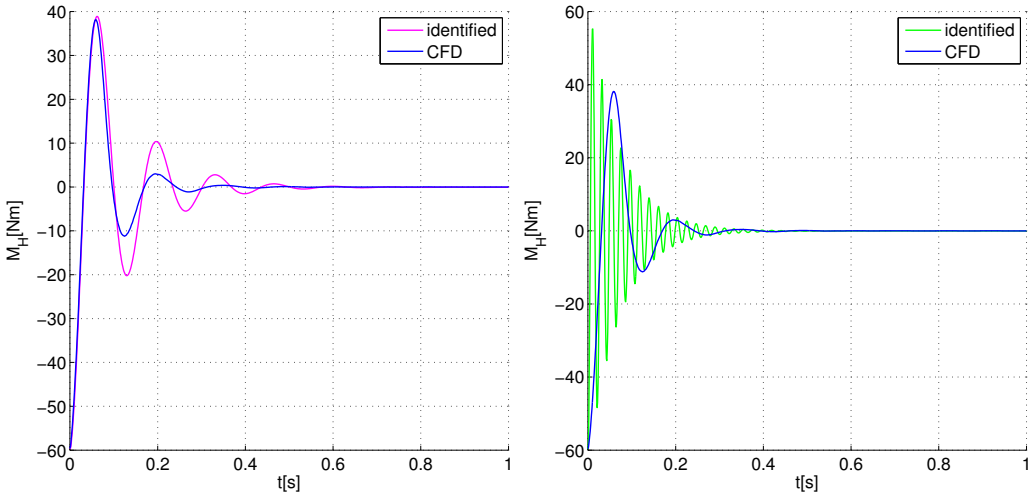

(a) $N = 10$ (b) $N = 42$

Figure 5.6: Comparison of system responses between the aeroelastic CFD-based model and the aeroelastic ROM-based model obtained varying the model order N (Mach number $M = 0.8$).

Once the low-order model is identified, the behavior of the eigenvalues of the aeroelastic system for different values of the freestream dynamic pressure q_∞ is obtained at constant Mach number. The reason for this analysis is that the low-order model is typically used to search for instabilities at the same Mach number by repeatedly changing the dynamic pressure without varying the Mach number. The buzz point is detected when the real part of an eigenvalue has null value. In Fig. 5.7 the real part of the eigenvalues of the resulting aeroelastic state matrix is plotted against dynamic pressure. The dependence of the model with respect to the dynamic pressure is linear in the model and this proportionality is also observed in the figure. A bifurcation of the real part of the eigenvalues is present in concurrence with the coalescence to null value of the corresponding imaginary parts, which is a typical feature of aeroelastic dynamic phenomena. For this particular Mach number, no instability points are detected.

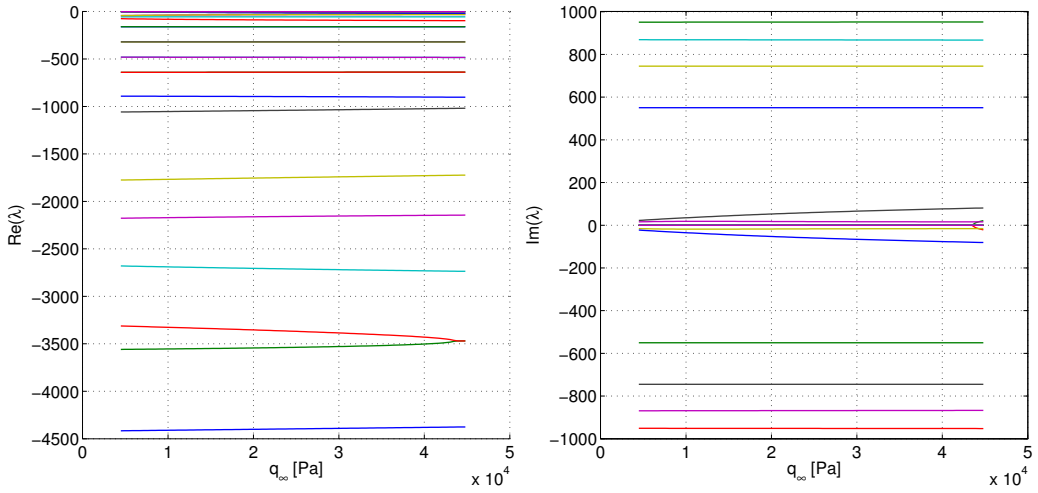

(a) Real part

(b) Imaginary part

Figure 5.7: Eigenvalues λ of the aeroelastic state matrix plotted against dynamic pressure (Mach number $M = 0.8$).

In addition, a comparison between the CFD-based aeroelastic response and the ROM-based response is provided at three dynamic pressures, namely q_∞. The different dynamic pressure is obtained in the CFD solver by varying the freestream pressure p_∞, because

$$q_\infty = \frac{1}{2}\gamma p_\infty M_\infty^2.$$

The comparison shows good agreement, still pointing out the difference in the system damping ratio. It is also noticeable that the response is less stable for lower dynamic pressure, which would resemble higher altitudes.

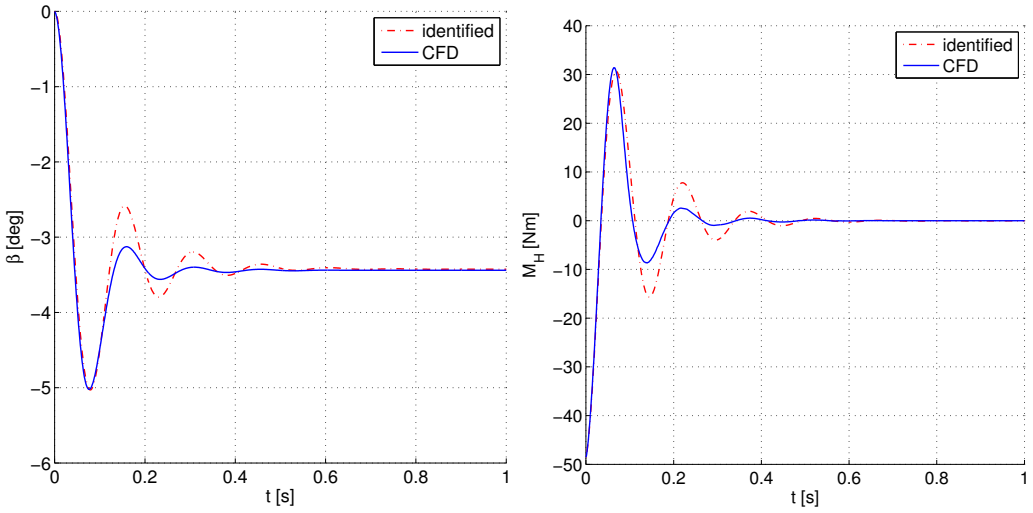

(a) Rotation (b) Moment

Figure 5.8: Comparison of system responses between the aeroelastic CFD-based model and the aeroelastic ROM-based model (Mach number $M = 0.8$, dynamic pressure $q_\infty = 13440$ Pa).

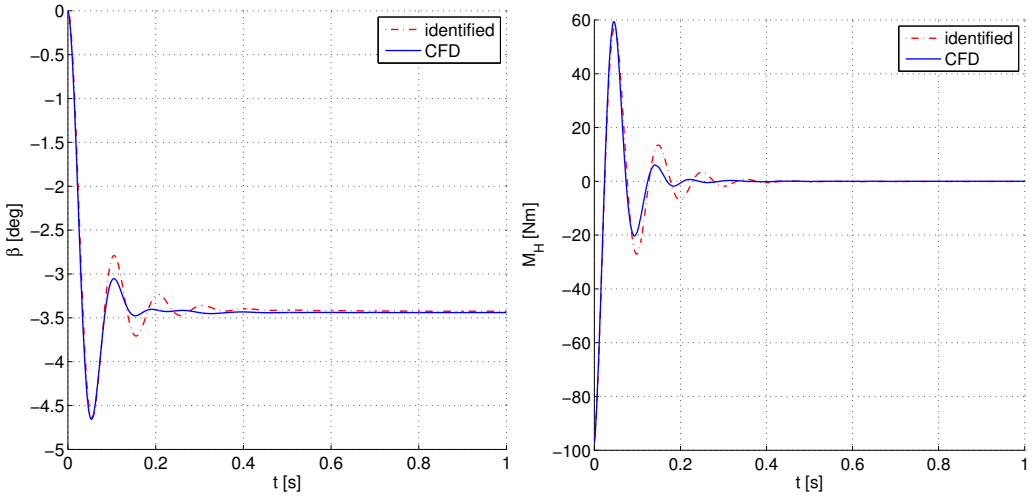

(a) Rotation (b) Moment

Figure 5.9: Comparison of system responses between the aeroelastic CFD-based model and the aeroelastic ROM-based model (Mach number $M = 0.8$, dynamic pressure $q_\infty = 26880$ Pa).

The search for an instability point leads to the identification of the reduced-order model at higher Mach numbers. The genetic algorithm is then run for each training

signal corresponding to a different Mach number. For Mach number $M = 0.835$ the reduced-order model finally predicts a point of aeroelastic instability. The identified aerodynamic response is presented in Fig. 5.10. It is worth notice that the output signal at Mach number $M = 0.835$ differs significantly from the output at Mach number $M = 0.8$, although the input signal is the same. This might be an evidence that the system attitude is changing. The instability point is marked in Fig. 5.11, whereas the real and imaginary parts of the eigenvalue are plotted in Fig. 5.12.

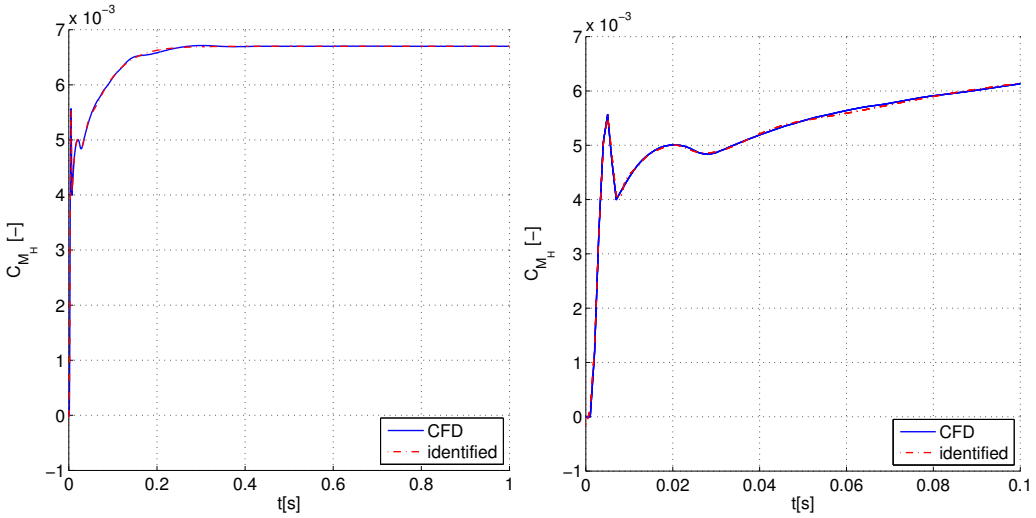

(a) Aerodynamic output (b) Zoom

Figure 5.10: Comparison of the recorded CFD-based response and the identified response subsequent to the prescribed input signal (Mach number $M = 0.835$).

Once the point of instability is found, the coupled Euler solution can then be

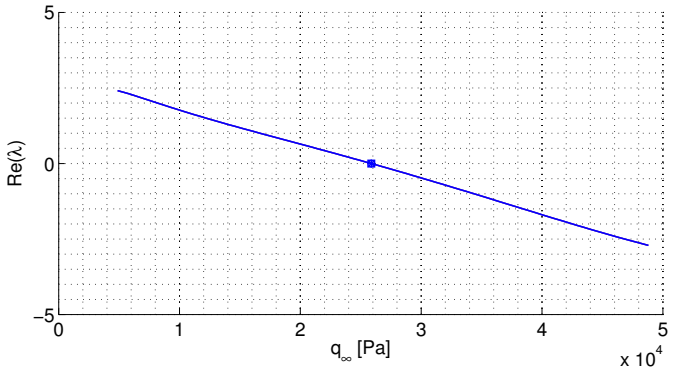

Figure 5.11: Instability point (Mach number $M = 0.835$).

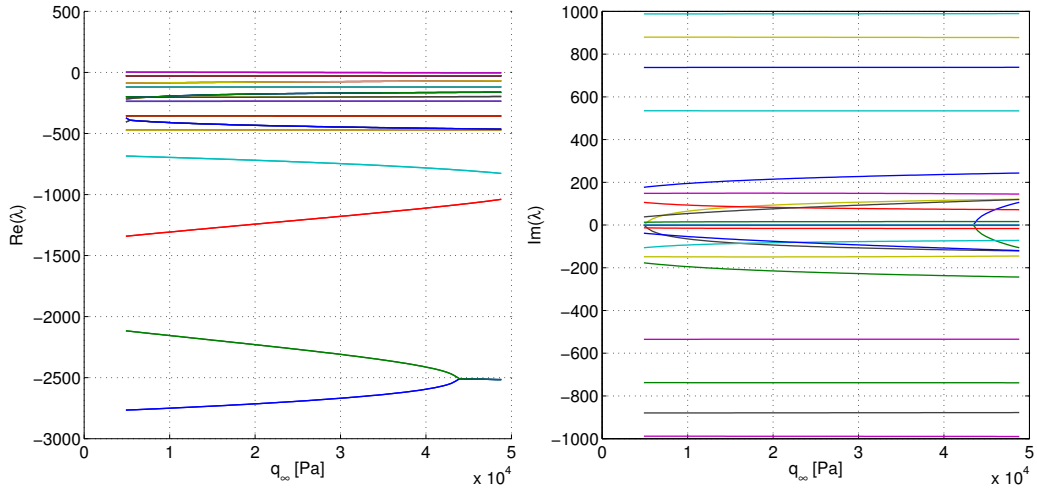

(a) Real part (b) Imaginary part

Figure 5.12: Eigenvalues λ of the aeroelastic state matrix plotted against dynamic pressure (Mach number $M = 0.835$).

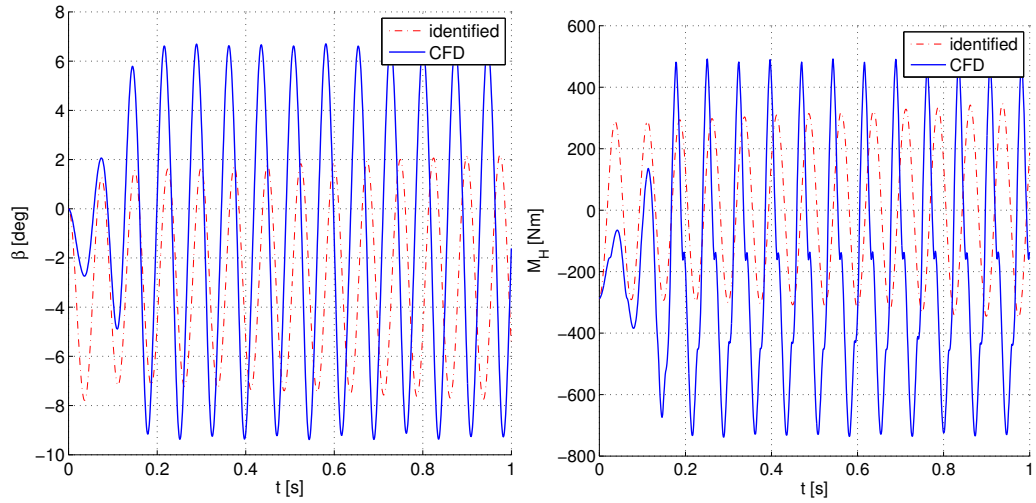

(a) Aerodynamic output (b) Zoom

Figure 5.13: Comparison of the recorded CFD-based response and the identified aeroelastic response (Mach number $M = 0.835$, dynamic pressure $q_\infty = 25870$ Pa).

run once to verify the accuracy of the coupled model solution. The comparison between the identified signal and the CFD aeroelastic computation is presented in Fig. 5.13. The plot shows that the high-order aeroelastic response is actually a buzz response, thereby proving that the identification effectively predicts an

instability onset. However, the amplitude is underestimated, a slight frequency shift progressively increases after the first two cycles and the highly nonlinear behaviour of the waves is not correctly represented. It is remarkable, though, that the frequency of the first cycles is well predicted.

Finally, it is worth noting that the CFD direct computations show buzz onset at various Mach number with different characteristic amplitude and frequency (for instance, the buzz results obtained in Chapter 4 at Mach number $M = 0.82$ differ from the response at Mach number $M = 0.835$ in Fig. 5.13). Instead, the reduced-order model is capable of predicting buzz onset only at Mach number $M = 0.835$ and for one precise value of dynamic pressure. This can be ascribed to the linearity assumption which is not capable of representing the mutual energy exchange between the aerodynamics and the structural dynamics that drives buzz. A possible explanation of the mechanism is that damping ratio and frequency have a dependence on the structural motion; because the linear analysis captures the frequencies better than damping, it is likely that the latter have a stronger dependence on the structural motion. In other words, the nonlinearity of the phenomenon seems to manifest itself with terms proportional to the structural velocity field rather than to the displacement field.

Conclusion

In the present work the numerical modelling of aileron buzz is discussed. The focus of the analysis is the aerodynamic model, which is obtained in two different ways: on one hand a CFD model is employed and on the other a low-order model is developed. The CFD-based aeroelastic model is founded on the numerical implementation of the two-dimensional Euler equations, which is an appropriate model for the simulation of non-classical aileron buzz, and a rigid model is chosen for the freely-hinged control-surface. The weak numerical aeroelastic coupling is obtained by means of two different approaches, which yield different descriptions of the geometric detail of the aileron hinge. The solver AeroFoam is used for the direct numerical simulation of the aeroelastic problem. In particular, the preliminary results show a noticeable sensitivity of the system response with respect to mesh refinement, size and with respect to the geometric detail of the integration of the control-surface into the wing. The reason for this is the dominant role of the shock dynamics in the aeroelastic phenomenon, which requires a finer representation in order to be accurately captured. In addition, the overall numerical layout proves to be a reliable means for the stability prediction of aileron-buzz. The numerical results also provide information for the development of the reduced-order model of the aerodynamic sub-system, which is a substitute of the CFD algorithm. The model structure is built on a linearity assumption and leveraging the idea of a grey box, that is a model containing some pieces of information about the actual system, such as the property of asymptotic stability and the oscillating behavior. The identification of the aerodynamic sub-system parameters is obtained by means of a suited genetic algorithm which exploits the data recorded in a preliminary CFD computation with a prescribed input signal properly exciting the dynamic system. The identification strategy proves to be effective and reaches accurate results, whereas the linear low-order model is capable of predicting instability and representing the results of the high-order CFD-based aeroelastic model yet with a limited range of applicability. In particular, the linear model is strongly dependent on the initial perturbation, thereby yielding a good agreement with the CFD results in the first istants of time. In addition, the response of the low-order model is similar to the CFD-based aeroelastic response more in terms of motion frequency rather than in damping ratio. This might be

an evidence that the nonlinearity manifests itself with terms proportional to the velocity field rather than the displacement field.

In this sense the natural development of the work is the implementation of a nonlinear low-order model: the basis of such model have already been developed in the presented analysis and it is believed, based on the response frequency analysis, that the employment of a polynomial substitute of the input would be sufficient to resemble the nonlinear behavior, thereby predicting with higher accuracy the buzz cycle and the buzz onset at each Mach number. In addition, the low-order model could be the basic constituent of a nonlinear model that could also take into account the variation of freestream Mach number and angle of attack. With such a tool a more comprehensive model of the aileron buzz would be provided, that could be applied also in the case of pitching arifoils. In addition, the state-space model would is possibly a profitable tool for the implementation of active control systems.

With regard to the CFD model, future works would focus on the viscous, three-dimensional analysis of buzz. As already pointed out, taking into account three-dimensional effects and viscosity will undoubtly affect the results to the extent that buzz onset would be shifted with Mach number, but it is likely that the main features highlighted in the current work would still occurr. Anyway, the inclusion of these effects in the analysis would provide more accurate CFD results, as well as enriching the CFD-based reduced-order model. In addition, Type A buzz could be studied in detail, focusing on the evaluation of the effectiveness of the presented model structure for this kind of buzz.

In conclusion, the work provides further insight in the numerical simulation of shock-dominated instability aeroelastic phenomena and blazes a trail for the development of a low-order model for the analysis of non-classical aileron buzz.

Bibliography

[1] http://aircrashed.com/cause/cCHI01MA163.shtml.

[2] Lambourne, N. C., 1960. Some Instabilities arising from the interactions between shock waves and boundary layers. Technical Report 473, Aeronautical Reasearch Council.

[3] Lambourne, N. C., 1962. Control-surface buzz. Reports and Memoranda 3364, Aeronautical Reasearch Council, London, UK, May.

[4] Brown, H. H., Rathert, G. A., and Clousing, L. A., 1947. Flight-test measurements of aileron control surface behaviour at supercritical Mach numbers. Naca Research Memorandum A7A15, April.

[5] Erickson, A. L., and Stephenson, J. D., 1947. A suggested method of analyzing for transonic flutter of control surfaces baed on available experimental evidence. Research Memorandum A7F30, NACA.

[6] Bendiksen, O. O., 1993. "Nonclassical aileron buzz in transonic flow". In 34th AIAA/ASME/ASCE/AHS/ASC Structures, Structural Dynamics and Materials Conference. AIAA Paper 93-1479.

[7] Steger, J. L., and Bailey, H. E., 1979. "Calculation of transonic aileron buzz". In 17th Aerospace Sciences Meeting. AIAA Paper 79-0134.

[8] Howlett, J. T., 1992. Calculation of unsteady transonic flows with mild separation by viscous-inviscid interaction. Nasa Technical Paper 3197, Langley Research Center, June.

[9] Fuglsang, D. F., Brase, L. O., and Agrawal, S., 1992. "Numerical study of control surface buzz using computational fluid dynamic methods". In AIAA 10th Applied Aerodynamics. AIAA 92-2654.

[10] Livne, E., 2003. "Future of airplane aeroelasticity". *Journal of Aircraft*.

[11] Bendiksen, O. O., 1992. "Role of shock dynamics in transonic flutter". In Prod. AIAA Dynamics Specialists Comf., pp. 401–414. AIAA Paper 92-2121.

[12] Muffo, D., Quaranta, G., Guardone, A., and Mantegazza, P., 2007. Interface Velocity Consistency in time-accurate flow simulations on dynamic meshes. Politecnico di Milano, Italy.

[13] Guardone, A., and Quartapelle, L. High-resolution unstructured finite-volume methods for conservation laws. Politecnico di Milano, Italy.

[14] LeVeque, R. J., 2002. *Finite Volume Methods for Hyperbolic Problems*. Cambride University Press.

[15] Quarteroni, A., Sacco, R., and Saleri, F., 2008. *Matematica Numerica*. Springer.

[16] Quarteroni, A., 2008. *Modellistica Numerica per Problemi Differenziali*. Springer.

[17] Romanelli, G., Serioli, E., and Mantegazza, P., 2010. "A 'free' approach to computational aeroelasticity". In 48th AIAA Aerospace Sciences Meeting. AIAA 2010-176.

[18] Blazek, J., 2001. *Computational Fluid Fynamics: Principles and Applications*. Elsevier.

[19] Witteveen, J., and Bijl, H., 2009. "Explicit mesh deformation using inverse distance weighting interpolation". In 19th AIAA Computational Fluid Dynamics. AIAA Paper 2009-3996.

[20] Romanelli, G., 2012. "Computational Aeroservoelasticity of Free-Flying Deformable Aircraft". PhD Thesis, Politecnico di Milano, March.

[21] Bisplinghoff, R. L., Ashley, H., and Halfman, R. L., 1996. *Aeroelasticity*. Dover Publications.

[22] Saito, H., 1959. On the Aileron Buzz in the Transonic Flow . Report 346, Aeronautical Reasearch Institute, University of Tokyo.

[23] Quaranta, G., Masarati, P., and Mantegazza, P., 2005. "A conservative mesh-free approach for fluid-structure interface problems". In COUPLED PROBLEMS.

[24] Romanelli, G., and Serioli, E., 2008. "Un approccio libero alla moderna Aeroelasticità Computazionale". MSc Thesis, Politecnico di Milano, July.

[25] Kwon, H., Kim, D., and Lee, I., 2004. "Frequency and time domain flutter computations of a wing with oscillating control surface including shock interference effects". *Aerospace Science and Technology*.

[26] Forestieri, G., Guardone, A., Isola, D., Marulli, F., and Quaranta, G., 2011. "Numerical simulation of aileron buzz using an adaptive-grid compressible flow solver for dynamic meshes". In COUPLED PROBLEMS.

[27] Beran, P. S., and Silva, W. A., 2001. "Reduced-order modeling: New approaches for computational physics". *American Institute of Aeronautics and Astronautics*.

[28] Dowell, E. H., Hall, K. C., Thomas, J. P., and Florea, R., 1999. "Reduced order models in unsteady aerodynamics". *American Institute of Aeronautics and Astronautics*. AIAA 99-1261.

[29] Roger, K. L., 1977. Airplane math modeling methods for active control design. Technical Report CP-228, AGARD, August.

[30] Cowan, T. J., Arena, A. S., and Gupta, K. K., 2001. "Accelerating computational fluid dynamics based aeroelastic predictions using system identification". *Journal of Aircraft*.

[31] Ljung, L., 1999. *System Identification Theory for the User*. Prentice Hall PTR.

[32] Bittanti, S., 2000. *Identificazione dei Modelli e Controllo Adattivo*. Pitagora Editrice.

[33] Weise, T., 2009. Global optimization algorithms - theory and application.